PE&RS
May 2023 Volume 89, Number 5

PHOTOGRAMMETRIC ENGINEERING & REMOTE SENSING — *The official journal for imaging and geospatial information science and technology*

The magnitude 7.8 and 7.5 earthquakes that struck southern Türkiye and western Syria on February 6, 2023, caused widespread destruction in both countries

2023 ASPRS International Technical Symposium

June 12-16, 2023
VIRTUAL

ASPRS is happy to announce the dates of its virtual conference. The 2023 ASPRS International Technical Symposium will take place.

The symposium will consist of:

- 15-minute oral presentations
- 5-minute Ignite-style presentations
- Poster Gallery
- Sustaining Member Vendor Spotlights
- ASPRS Society Highlights

Sessions will run each day from 10:00 AM to 6:00 PM Eastern Daylight Time (UTC - 4). All sessions will be recorded and made available on-demand to conference registrants. Presenters are eligible to submit full manuscripts for publication in the ISPRS Archives.

Interested in Presenting? For more information or to submit an abstract visit https://my.asprs.org/2023Symposium/2023-Symposium/Call-for-Abstracts.aspx

- Submission deadline is May 1, 2023
- Presenters will be notified of acceptance by May 8, 2023
- Presenters must be registered for the conference by May 22, 2023 to be included in the conference program

Registration Fees

ASPRS Member	$150 USD
ASPRS Student Member	$ 50 USD
ASPRS Emeritus Member	$ 25 USD
Non Member	$250 USD

Sponsorship Opportunities

- Vendor Spotlight/Product Demo
- Day Sponsor
- Session Sponsor
- Workshop Sponsor

"We are happy to offer this educational opportunity to the geospatial community. Virtual events are an excellent way to exchanammunity without the cost and time constraints of travel," said Karen Schuckman, ASPRS Executive Director

https://my.asprs.org/2023Symposium/

ANNOUNCEMENTS

Trimble's Applanix Transitions to the Trimble Brand Identity - Company embraces new aesthetic look and feel, while providing same trusted quality and expertise.

As you may have realized from our building, our website, and other promotional items, Applanix Corporation has fully adopted the Trimble global brand identity including the Trimble logo, colour scheme, and other standards and templates. The name Applanix does live on, however, as the brand name of the Positioning and Orientation Systems (POS) product line we first introduced to the mobile mapping world back in the 1990s, including the POS AV, POS MV, POS LV, and POSPac. These are now known as the Applanix POS systems, i.e. Applanix POS AV, Applanix POSPac MMS, etc.

While the Trimble look and feel may seem new to some of you, Applanix is celebrating its 20th anniversary of becoming "A Trimble Company" this year, and this change is a branding matter only. There are no changes to the people, products, or services we provide. Customers can expect the same trusted quality, expert knowledge, and unparalleled product support across our entire portfolio of products as they have always had.

Trimble Applanix will continue its ongoing commitment to innovation and new product development within the mobile mapping and surveying industry, and will continue to leverage Trimble's connected ecosystem of capabilities, networks, and partnerships to bring added value and benefit to our customers.

We encourage customers to connect with us through all the same channels as before—including our website, www.applanix.com, and by locating us at upcoming trade shows and conferences as part of the Trimble Booth.

As we celebrate this milestone 20th anniversary with Trimble, we wish to express our ongoing gratitude to all of our customers who continue to rely on our products and solutions for pinpoint accuracy, efficiency, and ease of use in all of their mobile mapping, survey, and autonomy applications. We look forward to many more decades assisting companies, developers, manufacturers, surveyors, and engineers reach their project goals by providing inertial navigation solutions that they can depend on with confidence.

Although our logo and branding look has changed, please note that we continue to operate with the legal name Applanix Corporation.

L3Harris Technologies announced a $765 million contract from NASA to design and build the next-generation, high-resolution imager for NOAA's Geostationary Extended Observations satellite system.

The GeoXO Imager will provide advanced visible and infrared imagery, more precise observations and improved water vapor measurements to significantly improve the accuracy and timeliness of weather forecasting in the Western Hemisphere. The addition of two new spectral bands and enhanced spatial resolution will improve space-based severe weather monitoring as well as short-term weather predictions and wildfire tracking.

"This award demonstrates L3Harris' proficiency to advance mission-critical geostationary imagers for NOAA," said Ed Zoiss, President, Space and Airborne Systems, L3Harris. "We're honored to continue our role with NASA and NOAA as a key provider of geostationary capabilities by adding relevant mission value to our nation's next-generation weather architecture."

Slated to begin launching in 2032, the GeoXO mission will provide the mainstay of NOAA's geostationary observation through 2055.

"We're proud to be a part of NOAA's GeoXO observing system, supporting short-term forecasts, severe weather, and disaster monitoring to provide advanced warning to decision makers," said Rob Mitrevski, Vice President and General Manager, Spectral Solutions, L3Harris. "This program continues our 60-year heritage in this mission area, serving to protect the lives and personal property of our citizens."

From space to ground, L3Harris provides the Advanced Baseline Imager for space-based data collection on NOAA's GOES-R mission, as well as the GOES-R enterprise ground system providing downlink, data processing and distribution, and command and control of the four-satellite GOES-R constellation.

Ten years after completing the company's first shoreline mapping project, **NV5 Geospatial** announced today that it has mapped more than 26 million acres of North America's shoreline and riverine environments for more than 200 projects. The projects have spanned across North America from the Nuyakuk River in Alaska, Lake Tahoe in California, the Rio Grande in Texas, the entire coasts of South Carolina and North Carolina, Achigan River in Quebec, Chesapeake Bay in Maryland, and the Florida Keys. In 2022 alone, the company mapped and acquired topobathymetric lidar data for 14 projects including the Yellowstone River, Wyoming; Hells Canyon, Indiana; Revillagigedo Island, Alaska, and Iles de la Madeleine in Quebec.

In 2023, NV5 is already slated for a number of additional shoreline and riverine projects including a two year contract with the National Oceanic and Atmospheric Administration's

(NOAA) National Geodetic Survey to provide topobathymetric lidar, 4-band imagery, and mapping of 3,115 sq miles of the coastal Maine shoreline.

10 Years of Technological Innovation—NV5 Geospatial first mapped the shorelines and riverine environments in 2012 with the acquisition of high-resolution bathymetric lidar and natural color imagery for 34,051 acres of shoreline along the Sandy River, located in northwestern Oregon, to study the ever changing basin geomorphology. Today, topobathymetric lidar has a wide range of use cases, including shoreline and coastal intelligence, habitat restoration, floodplain modeling, volumetric analysis, infrastructure planning and engineering, and coastal zone management.

Topobathymetric lidar simultaneously measures and records three distinct surfaces – land, water, and submerged land using airborne laser-based sensors. While this technology shares some characteristics of traditional airborne lidar mapping, it also has significant differences that increase the understanding of the nearshore environment for improved marine resource mapping, benthic habitat mapping, shoreline delineation, nautical charting, and marine debris mapping.

Helping to Solve North America's Most Challenging Coastal and Riverine Issues—The following five projects provide a sampling of the work NV5 Geospatial has participated in over the last 10 years; Hurricanes Michael, Florida and Florence, North Carolina, Okanagan Lakes, British Columbia, Elbow River, Alberta, Canada, Florida Keys, Florida, and Platte River, Nebraska.

For more information, visit https://www.nv5.com/news/coastal-riverine-26millionacres/.

ACCOMPLISHMENTS

Esri announced that Dr. Dawn Wright, the company's chief scientist, has been elected to the National Academy of Engineering (NAE). Dr. Wright is being honored by the Academy for her distinguished work applying geographic information system (GIS) technology to ocean science and developing GIS models for the oceans. In addition to her work as chief scientist of Esri, Dr. Wright has been a professor of geography and oceanography at Oregon State University since 1995 and was integral in building the first geospatial data models of the world's oceans. Having served on the Science Advisory Boards of both NOAA and the EPA, Wright joined Esri in 2011.

"It is truly an honor to be recognized by the National Academy of Engineering," said Wright. "Ocean exploration is impossible without the tools that enable scientific observation and understanding. It's been my privilege to help build some of the most innovative technologies allowing more insightful environmental data collection, and to be able to work with all the talented people at Esri."

On July 12, 2022, Wright served as mission specialist for a historic descent nearly 36,000 feet into the Pacific Ocean to capture images and data from the Challenger Deep, the deepest known point in the Earth's ocean. Wright was one of the few individuals—and the first Black person—to visit Challenger Deep, located within the Mariana Trench. The expedition produced an unprecedented series of detailed maps and data from the deepest place on Earth.

"Our technology has always been grounded in science, and Dawn Wright is one of the great scientists that has made our company so special," said Jack Dangermond, Esri founder and president. "She is both a keen observer of the natural world as well as someone building solutions to help solve some of its biggest challenges."

Founded in 1964, the NAE is a private, independent, nonprofit institution that provides engineering leadership in service to the nation. Its mission is to advance the welfare and prosperity of the nation by providing independent advice on matters involving engineering and technology, and by promoting a vibrant engineering profession and public appreciation of engineering. NAE membership is one of the highest professional honors accorded an engineer and is determined by current NAE members, including more than 2,000 senior professionals in business, academia, and government who are among the world's most accomplished engineers. It is the sibling organization of the National Academy of Sciences, to which Wright was elected as a member in 2021.

To view a full list of new members elected to the NAE, visit nae.edu/289843/NAENewClass2023.

CALENDAR

- 22-24 May, **STRATUS Conference.** For more information, visit http://stratus-conference.com/.
- 12-16 June, **ASPRS 2023 International Technical Symposium.** For more information, visit https://my.asprs.org/2023Symposium/.
- 16-19 October, **GIS-Pro 2023**, Columbus, Ohio. For more information, visit www.urisa.org/gis-pro.

PE&RS
PHOTOGRAMMETRIC ENGINEERING & REMOTE SENSING
The official journal for imaging and geospatial information science and technology
May 2023 Volume 89 Number 5

265 GIS Tips & Tricks — Checkerboards are for board games, not GIS!
Chad Lopez and Al Karlin, Ph.D. CMS-L, GISP

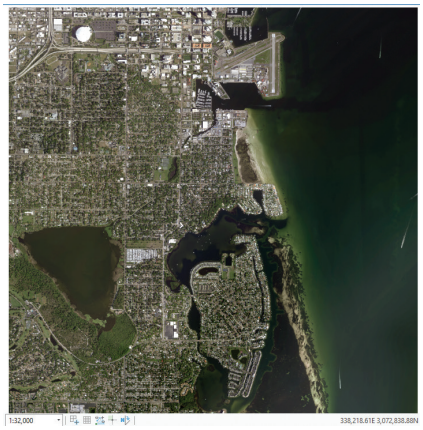

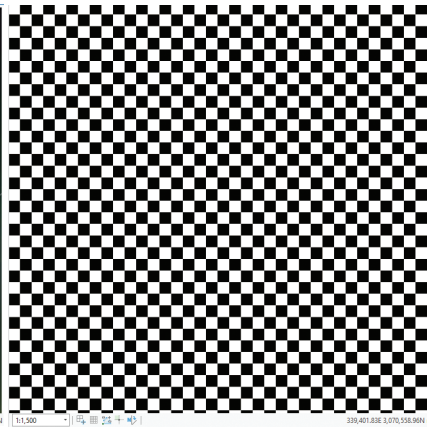

267 In Memoriam
Ron Ondrejka

COLUMNS

265 GIS Tips & Tricks — Checkerboards are for board games, not GIS!

ANNOUNCEMENTS

267 In Memoriam — Ron Ondrejka

269 Call for *PE&RS* Special Issue Submissions — Special Issue on the Scholarship and Impacts of Professor Nina S. N. Lam

270 New ASPRS Members
Join us in welcoming our newest members to ASPRS.

DEPARTMENTS

261 Industry News

262 Calendar

290 ASPRS Sustaining Members

299 In-Press *PE&RS* Articles

300 Who's Who in ASPRS

YEARBOOK

271 Introduction

272 ASPRS Presidential Address — Lorraine B. Amenda, PLS, CP

274 ASPRS Awards Program 2023

288 Annual Business Meeting & Installation of Officers

291 Automatic Satellite Images Ortho-rectification using K-means Based Cascaded Meta-heuristic Algorithm
Oussama Mezouar, Fatiha Meskine, and *Issam Boukerch*

Orthorectification of high-resolution satellite images using a terrain-dependent rational function model (RFM) is a difficult task requiring a well-distributed set of ground control points (GCPs), which is often time-consuming and costly operation. Further, RFM is sensitive to over-parameterization due to its many coefficients, which have no physical meaning. Optimization-based meta-heuristic algorithms appear to be an efficient solution to overcome these limitations. This paper presents a complete automated RFM terrain-dependent orthorectification for satellite images.

301 UAS-based Multi-temporal Rice Plant Height Change Prediction
Yuanyang Lin, Jing He, Gang Liu, Biao Mou, Bing Wang, and *Rao Fu*

Analyzing rice growth is essential for examining pests, illnesses, lodging, and yield. To create a Digital Surface Model (DSM) of three important rice breeding stages, an efficient and fast (compared to manual monitoring) Unoccupied Aerial System was used to collect data.

311 Spherical Hough Transform for Robust Line Detection toward a 2D-3D Integrated Mobile Mapping System
Bo Xu, Daiwei Zhang, Han Hu, Qing Zhu, Qiang Wang, Xuming Ge, Min Chen, Yan Zhou

Line features are of great importance for the registration of the Vehicle-Borne Mobile Mapping System that contains both lidar and multiple-lens panoramic cameras. In this article, a spherical straight-line model is proposed to detect the unified line features in the panoramic imaging surface based on the Spherical Hough Transform.

321 Blind and Robust Watermarking Algorithm for Remote Sensing Images Resistant to Geometric Attacks
Xinyan Pang, Na Ren, Changqing Zhu, Shuitao Guo, and *Ying Xiong*

To address the problem of weak robustness against geometric attacks of remote sensing images' digital watermarking, a robust watermarking algorithm based on template watermarking is proposed in this article, which improves the robustness of digital watermarking against geometric attacks by constructing stable geometric attack invariant features.

See the Cover Description on Page 264

facebook.com/ASPRS.org linkedin.com/groups/2745128 twitter.com/ASPRSorg youtube.com/user/ASPRS

COVER DESCRIPTION

The magnitude 7.8 and 7.5 earthquakes that struck southern Türkiye and western Syria on February 6, 2023, caused widespread destruction in both countries.

The initial earthquake emanated from a fault 18 kilometers (11 miles) below the land surface. The shallow depth meant the earthquake produced violent shaking that affected areas hundreds of kilometers from the epicenter. The first quake was followed by a 7.5 magnitude event about nine hours later, as well as hundreds of smaller aftershocks.

As news of the event spread, scientists at space agencies around the world—including NASA—began processing and analyzing satellite data relevant to the event.

"These were very large and powerful earthquakes that ruptured all the way up to the surface over a long series of fault segments," said Eric Fielding, a geophysicist at NASA's Jet Propulsion Laboratory. "This generated extremely strong shaking over a very large area that hit many cities and towns full of people. The rupture length and magnitude of the magnitude 7.8 earthquake was similar to the 1906 earthquake that destroyed San Francisco."

The preliminary damage proxy map above shows parts of the cities of Türkoğlu, Kahramanmaraş, and Nurdağı. Dark red pixels represent areas likely to have severe damage to buildings, homes, and infrastructure or changes to the landscape, while orange and yellow areas are moderately or partially damaged. Each pixel measures about 30 meters across (about the size of a baseball infield).

The Earth Observatory of Singapore - Remote Sensing Lab created the damage proxy map in collaboration with NASA's Jet Propulsion Laboratory and Caltech by processing data collected by the PALSAR-2 radar instrument on the Japan Aerospace Exploration Agency (JAXA) Advanced Land Observing Satellite-2 (ALOS-2) on February 8, 2023, and provided by Sentinel Asia. The satellite carries a synthetic aperture radar that sends pulses of microwaves toward Earth's surface and listens for reflections of those waves to map the landscape, including buildings. By comparing the February 8 data to observations made by the same satellite before the earthquake (on April 7, 2021, and April 6, 2022) scientists tracked the changes and began to identify areas that were likely damaged.

"The map covers only the central part of the affected area due to the narrow, 70-kilometer swath of the ALOS-2 fine-beam data used, but it includes the epicenters of both the magnitude 7.8 main earthquake and the magnitude 7.5 aftershock," said Fielding. "Note that the time intervals between the ALOS-2 acquisitions are up to a year apart, so the accuracy of the damage proxy map may be lower in areas of vegetation, such as in the mountains, due to seasonal variations." Some of the areas marked as damaged in vegetated areas may not have been damaged, and some areas showing no damage in vegetated areas may be damaged.

NASA Earth Observatory images by Joshua Stevens, using Landsat data from the U.S. Geological Survey and ALOS-2 data from the Japan Aerospace Exploration Agency/JAXA and the Earth Observatory of Singapore Remote Sensing Lab. Story by Adam Voiland.

For full article and references, visit https://landsat.visibleearth.nasa.gov/view.php?id=150949

Landsat imagery courtesy of NASA Goddard Space Flight Center and U.S. Geological Survey

PHOTOGRAMMETRIC ENGINEERING & REMOTE SENSING

JOURNAL STAFF

Publisher ASPRS
Editor-In-Chief Alper Yilmaz
Director of Publications Rae Kelley
Electronic Publications Manager/Graphic Artist
Matthew Austin

Photogrammetric Engineering & Remote Sensing is the official journal of the American Society for Photogrammetry and Remote Sensing. It is devoted to the exchange of ideas and information about the applications of photogrammetry, remote sensing, and geographic information systems. The technical activities of the Society are conducted through the following Technical Divisions: Geographic Information Systems, Photogrammetric Applications, Lidar, Primary Data Acquisition, Professional Practice, Remote Sensing Applications, and Unmanned Autonomous Systems. Additional information on the functioning of the Technical Divisions and the Society can be found in the Yearbook issue of *PE&RS*.

All written correspondence should be directed to the American Society for Photogrammetry and Remote Sensing, PO Box 14713, Baton Rouge, LA 70898, including general inquiries, memberships, subscriptions, business and editorial matters, changes in address, manuscripts for publication, advertising, back issues, and publications. The telephone number of the Society Headquarters is 301-493-0290; the fax number is 225-408-4422; web address is www.asprs.org.

PE&RS. *PE&RS* (ISSN0099-1112) is published monthly by the American Society for Photogrammetry and Remote Sensing, 8550 United Plaza Blvd, Suite 1001, Baton Rouge, Louisiana 70809 . Periodicals postage paid at Bethesda, Maryland and at additional mailing offices.

SUBSCRIPTION. *PE&RS* is available as an e-Subscription (single-site and multi-site licenses) and an e-Subscription with print add-on (single-site license only). PE&RS subscriptions are on a calendar-year, beginning in January and ending in December.

The rate for a single-site e-Subscription for the USA/Non-USA is $1040 USD, for Canadian* is $1092 USD.

The rate for a multi-site e-Subscription for the USA/Non-USA is $1040 USD plus $250 USD for each additional license, for Canadian* is $1092 USD plus $263 for each additional license.

The rate for e-Subscription with print add-on for the USA is $1525 USD, for Canadian* is $1612 USD, and for Non-USA is $1565 USD.

*Note: Subscription prices for Canada includes 5% of the total amount for Canada's Goods and Services Tax (GST #135123065). **PLEASE NOTE: All Subscription Agencies receive a 20.00 USD discount.**

POSTMASTER. Send address changes to PE&RS, ASPRS, PO Box 14713, Baton Rouge, LA 70898. CDN CPM #(40020812).

MEMBERSHIP. Membership is open to any person actively engaged in the practice of photogrammetry, photointerpretation, remote sensing and geographic information systems; or who by means of education or profession is interested in the application or development of these arts and sciences. Membership is for one year, with renewal based on the anniversary date of the month joined. Membership Dues include a 12-month electronic subscription to *PE&RS*. Annual Individual Membership dues are $175.00 USD and Student Membership dues are $50.00 USD. A tax of 5% for Canada's Goods and Service Tax (GST #135123065) is applied to all members residing in Canada.

COPYRIGHT 2023. Copyright by the American Society for Photogrammetry and Remote Sensing. Reproduction of this issue or any part thereof (except short quotations for use in preparing technical and scientific papers) may be made only after obtaining the specific approval from ASPRS. The Society is not responsible for any statements made or opinions expressed in technical papers, advertisements, or other portions of this publication. Printed in the United States of America.

PERMISSION TO PHOTOCOPY. The copyright owner's consent that copies of the article may be made for personal or internal use or for the personal or internal use of specific clients. This consent is given on the condition, however, that the copier pay the stated per copy fee through the Copyright Clearance Center, Inc., 222 Rosewood Drive, Danvers, Massachusetts 01923, for copying beyond that permitted by Sections 107 or 108 of the U.S. Copyright Law. This consent does not extend to other kinds of copying, such as copying for general distribution, for advertising or promotional purposes, for creating new collective works, or for resale.

GIS Tips & Tricks

Chad Lopez and Al Karlin, Ph.D.
CMS-L, GISP

Checkerboards are for board games, not GIS!

Most GIS-users know that GIS software can be great on some days and very frustrating on others. The difference in behavior can occur for no apparent reason, which just adds to the irritation. That apparently erratic behavior, coupled with the desire of most GIS mapmakers to include digital imagery as a basemap, can add to the frustration level when the image layers do not behave properly.

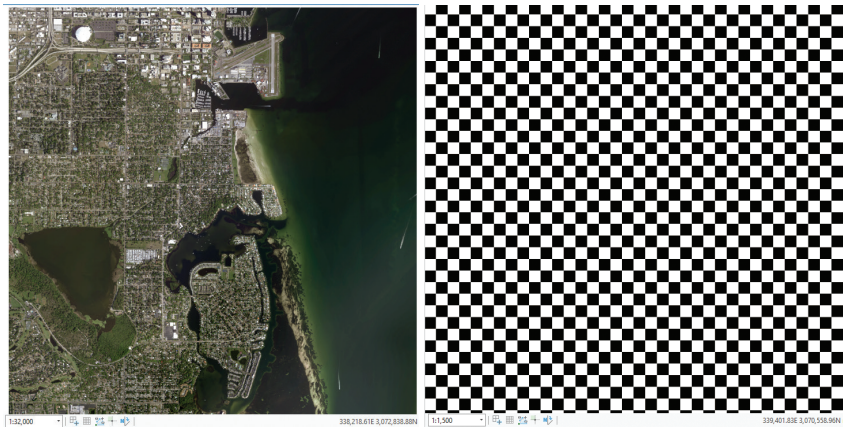

Figure 1. Mosaic Dataset viewed at a small scale (1:32,000; left) and the same Mosaic Dataset zoomed-in to a large scale (1:1,500; right) showing the checkerboard error.

A common format for managing and viewing basemap imagery in the Esri environment is as an Esri Mosaic Dataset in a file geodatabase. As can happen with all forms of geospatial data, you may encounter a mosaic dataset that displays properly one day, and the next day, it does not display as it should. This column identifies the two most common issues with displaying mosaic datasets; (1) the image draws correctly at small scales but disappears and presents a black & white checkerboard at larger scales (when you zoom in), and (2) the imagery draws correctly at large scales, but disappears and presents the black & white checkerboard at smaller scales (when you zoom out). The checkerboard display means that one or more mosaic dataset items are not accessible. Although Esri Mosaic Datasets may be displayed in other GIS environments, the "fixes" for Esri Mosaic Dataset issues illustrated below must be implemented in either the Esri Desktop or Pro environment. For convenience, we show only the ArcGIS Pro tools, but similar tools are also available in the ArcGIS Desktop environment.

TIP #1 — The raster dataset appears normally at small scales, but it displays as a black & white checkerboard when you zoom-in.

This error generally happens as a result of the mosaic dataset losing connection with the source imagery data because either, (1) the pathway to the source imagery is no longer valid, or (2) the source imagery is no longer in the specified path. The imagery displays at small scales because the image overviews, which were constructed during the mosaic processing, are being displayed, not the actual source imagery. To fix the file path(s) to the source imagery, use the "Repair Mosaic Dataset Paths" tool in the Data Management | Raster | Mosaic Dataset toolbox. Enter the new pathway to the image source data into the "New Path" box as in Figure 2 and run the tool.

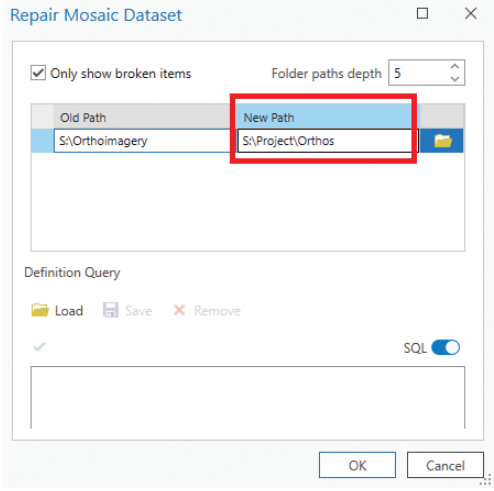

Figure 2. The "Repair Mosaic Dataset Paths" tool dialog in the Data Management Tools | Raster | Mosaic Dataset toolbox.

TIP #2 — The raster dataset appears normally at large scales, but it displays as a black & white checkerboard when you zoom-out.

Photogrammetric Engineering & Remote Sensing
Vol. 89, No. 5, May 2023, pp. 265-266.
0099-1112/22/265-266
© 2023 American Society for Photogrammetry and Remote Sensing
doi: 10.14358/PERS.89.5.265

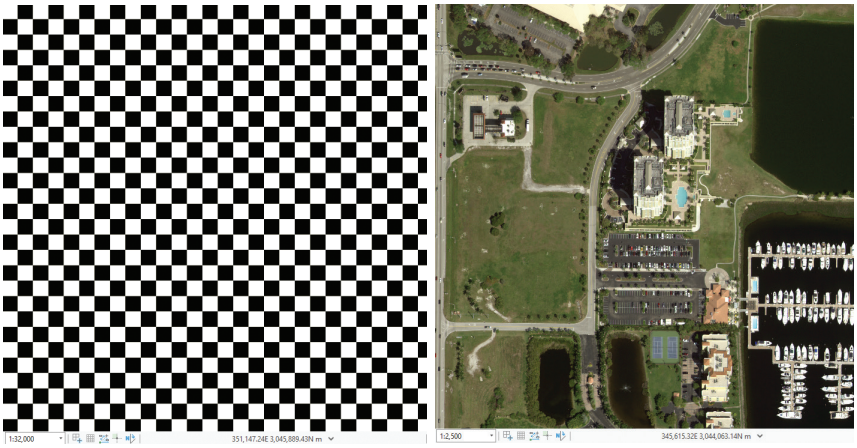

Figure 3. Mosaic Dataset viewed at a small scale (1:32,000; left) showing the checkerboard error, and the same Mosaic Dataset zoomed-in to a large scale (1:2,500; right).

TIP #3 — Both/Either the "Repair Mosaic Dataset" and the Build Overviews" tools can also be accessed by right-clicking on the mosaic dataset within a Catalog Pane or View.

TIP #4 — Lastly, the "Analyze Mosaic Dataset" tool (Figure 5), also found in the Data Management | Raster | Raster Mosaic toolbox, is a general diagnostic tool with several "Advanced Options" which can help determine what kind of issue or issues there are with your mosaic dataset.

This issue generally happens as a result of missing or corrupted overview items, not a file pathname as in Tip #1. Overviews which are built during the creation of the file geodatabase mosaic dataset are stored in a separate folder from the image data source. To fix invalid or corrupted overviews, simply build new ones to overwrite the old overviews using the "Build Overviews" tool, also in the Data Management | Raster| Mosaic Dataset toolbox, as in Figure 4 making certain to check the "Generate Overviews" checkbox.

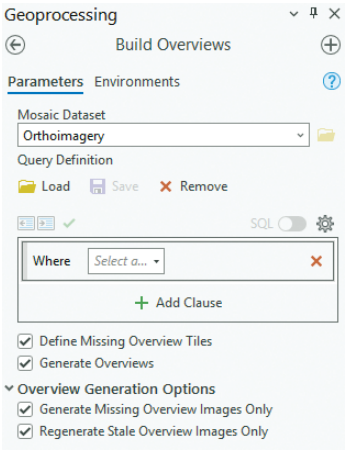

Figure 4. The "Build Overviews" tool dialog in the Data Management Tool | Raster | Mosaic Dataset toolbox.

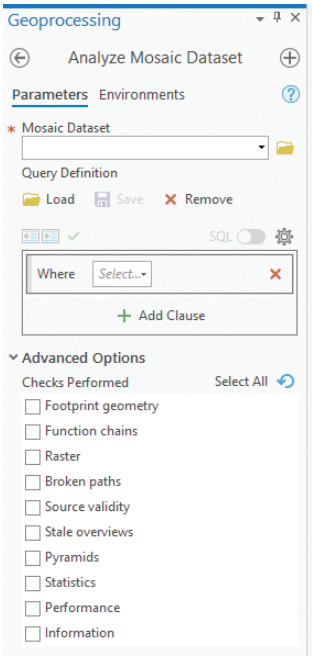

Figure 5. The "Analyze Mosaic Dataset" tool in the Data Management | Raster | Raster Mosaic toolbox has "Advanced Options" to help identify issues with Raster Datasets.

Send your questions, comments, and tips to GISTT@ASPRS.org.

Chad Lopez is a senior geospatial analyst with Dewberry's Geospatial and Technology Services group in Tampa, Florida. He has over 20-years of experience and has worked with all aspects of remote sensing and serves as a resource for most GIS/Remote Sensing software.

Al Karlin, Ph.D., CMS-L, GISP is a senior geospatial scientist with Dewberry's Geospatial and Technology Services group in Tampa, FL. Al works with all aspects of Lidar, remote sensing, photogrammetry, and GIS-related projects. Al also teaches beginning map making at the University of Tampa.

Ron Ondrejka

1933-2023

Ron Ondrejka, ASPRS Fellow, Cold War Reconnaissance Expert, beloved husband, father, and grandfather, passed away on March 11th, 2023, at the age of 89 from a sudden illness.

Early Life

Ron was raised in Milwaukee, Wisconsin. He grew up in a diverse area of the city and, in 1940 at the start of World War II, was a young lad of six. The diversity of Milwaukee led to an increased interest in both the war and military service. In the early 1950's, he graduated from high school, as class president, at a time when the military draft had been reinstated for the Korean War. He was offered the opportunity to sign up for three years and, at the end of his service, get a college education. He ended up in the U.S. Army Corps of Engineers and was sent to the mapping school at Fort Belvoir. After completing his training, he went to Korea and Japan where he supported the forces by updating maps from daily aerial photography. Every day, Ron would pick up the film from the aircraft, process it, and then interpret the imagery for changes. Details included locations of the North Korean and Chinese forces, as well as the location of the U.S. forces. This information was then relayed to the troops. He also managed to become the Far East Small Bore Rifle Champion during his enlistment.

With his well-developed interest in surveying and mapping, Ron returned to the U.S. where, using the GI-Bill, he began his formal education at the University of Wisconsin - Madison. There, he chose to study geodesy, photogrammetry and surveying under Amron Katz, a "super authority," later said to be one of the founders of the National Reconnaissance Office (NRO). While at the university, someone talked about a place called ITC. He continue. using the GI Bill and studied at ITC in the Netherlands. There, Ron completed his Master's of Science in Photogrammetry under the famous Dr. Willem Schermerhorn, who became the Netherlands Prime Minister after WWII.

Itek

On returning to the U.S., Ron was recruited by a company called Itek which grew out of Boston University. There he became the assistant to Dr. Claus Aschenbrenner. What Ron did not know at the beginning was that Itek was deep in the reconnaissance business and was super-secret. This is very ironic if you knew Ron because he liked to talk.

At Itek, Ron's initial responsibility covered aerial and satellite mapping applications with the U.S Army Topographic Center at Fort Belvoir, St. Louis, Missouri, and wherever else classified mapping activity was going on. The Itek Optical Bar Camera (OBC) was used on both the U-2 and the SR-71. One should note that the U.S. Air Force just retired the OBC camera in 2022.

Ron was involved in troubleshooting interesting problems across a range of mapping technologies. In one case, the cameras flown on spy satellites had horizon cameras to show the attitude of the spacecraft but the horizon images were fuzzy. Ron discovered the cameras being used were heating up where the filter frame was squeezing the filter and cracking the lenses.

Growing Responsibility

As the Korean War came to an end, Ron took over as the lead photogrammetrist at ITEK after Claus Aschenbrenner retired. In the 1960's, Ron worked on the panoramic cameras on the Corona satellites which was followed by the more sophisticated Hexagon series. (Perkin-Elmer made the panoramic camera for Hexagon, Itek made the 9x18" mapping camera.) At that time, the Corona and Hexagon Programs were well established with polar-orbiting satellites launched from California to go over the South Pole. In case there were any difficulties, they would crash in the ocean and not over land. If they were working properly when they reached the South Pole, you were in business and the satellite panoramic film cameras would then capture the areas of interest. Then, as the spacecraft got closer to Hawaii, it would slow down, turn

around, eject the film bucket so that the camera film package, which was attached to a parachute, could be grabbed as it was descending. The U.S. Air Force would then zip in, snag the bucket in mid-air, land, turn over the film, and ITEK would process it. The satellites always landed in the ocean at the same place so the Russians and Chinese would always be there in international waters hoping to get hold of the film canisters. With the film in hand, the whole idea was to get the film to Fort Belvoir and other places to be processed and interpreted so targeting maps could be updated.

For Hexagon, the Itek 9×18 inch mapping camera was dual use: 1) in NASA ER-2 aircraft for such things as forest inventory or. 2) hardened for use in spacecraft for security missions such as the Hexagon satellite. As noted above, the satellites were polar orbiting – as the earth turned, new areas were presented to be captured and you could turn the camera on and off to cover only the areas of interest. There were horizon cameras with short focal lengths for attitude and over time the focal length of the frame cameras increased. While Hexagon with longer focal length cameras came after Corona, Corona was the work-horse – and it was dual purpose – for spy satellites and uses such as the Apollo Moon Program where a 24-inch camera was used. Interestingly, none of the systems used for Apollo was ever lost. When he was lecturing to the University of Wisconsin students Ron was asked how they could tell which system was which – between the classified military and civilian 24-inch cameras. His response was: "we painted them different colors." In other words, there was no difference!

Itek also built the CCD cameras used in the Viking Lander Mission to Mars. Ron was at the Paris Air Show in 1976 when the first pictures came back. In typical Ondrejka humor, he would point to the first surface photograph of Mars on his office wall and remark, "we never did see anything move on the surface of Mars!"

ASPRS

When Ron came back from the Korean War and as he was getting into civilian applications of mapping, he was introduced to the American Society of Photogrammetry (ASP) by Dr. Claus Aschenbrenner at Itek. Ron developed all kinds of reasons to attend the ASP meetings such as networking with peers. Given the involvement of Itek in the spy satellite business and related systems, another reason for attending was the importance of politicians who were funding these major reconnaissance and mapping programs since ASP held many of the meetings in the Washington, DC area.

The significant growth of the ASP was because the imagery, initially for military applications, was being used by corporations, universities, and various government institutions.

Everyone started to realize that this tool helped them be more efficient in their activities whether it was earth sciences or military applications.

Ron noted that once a satellite was launched by NASA, the Air Force, or someone else, the interest was in extracting information from the data. You not only had to have a good device taking a picture – you also had to have a good reason for taking the picture. It was this extraction of data that promoted ASP activity and involvement.

Ron grew up in Wisconsin, near Lake Michigan, and returned to his roots. He was very active for decades with the Great Lakes Region of ASPRS and with remote sensing colleagues from around the world. He was particularly active with the Primary Data Acquisition Division (PDAD). Persons wishing to remember Ron are asked by his family to contribute to the ASPRS Western Great Lakes Scholarship Fund.

Direct contributions to the ASPRS WGL Scholarship Fund can be made by contacting:

Colin Lee, ASPRS WGL Treasurer
Email. colin.lee@state.mn.us
Work. 651 366 3433

More information about the ASPRS Western Great Lakes Region can be found at. http://wgl.asprs.org/

Ron will be deeply missed by his wife, son, grandchild, and countless remote sensing friends and colleagues from around the world. His stories, laughter, and kindness will live on in the hearts of all who knew him. Along the way, he may have helped prevent another global conflict.

Brian Huberty, Remote Sensing Advisor
Sharedgeo.org
ASPRS Western Great Lakes Region
http://wgl.asprs.org/2023/03/remembering-ron-ondrejka/

Ron Ondrejka out fishing on Big Lake, WI with granddaughter Meridian.

Call for *PE&RS* Special Issue Submissions

Special Issue on the Scholarship and Impacts of Professor Nina S. N. Lam

Expected Date for Publication: 2024

Special Issue Editors

Michael Leitner (mleitne@lsu.edu)
Jane Read (jaread@syr.edu)

This special issue recognizes Professor Nina S. N. Lam's ~45 years of contribution to Geographic Information and Environmental Sciences. From her first publications on spatial/areal interpolation methods in the early 1980s, she evolved into an internationally recognized scholar known for her leadership in diverse research areas, from scale, resolution, and fractals to environmental health, disaster resilience, and sustainability. Professor Lam, who currently holds the E. L. Abraham Distinguished Professor of Louisiana Environmental Studies title, has been the recipient of many honors and awards, including the inaugural Carolyn Merry Mentoring Award from the UCGIS (2016), being named a Fellow of both the AAG (2020) and the UCGIS (2016), as well as being named a LSU Rainmaker, recognizing one of the top 100 research and creative faculty (2008), and the LSU Distinguished Faculty Award (2006). Her legacy in research, teaching, and service continues through her many students, who are actively contributing to Geographic Information Science (GISc) in academia, government, and the private sector, including the second co-guest editor of this special issue.

This special issue celebrates the outstanding scholarly work of Professor Lam. We invite original contributions from her students, collaborators, and anyone impacted and influenced by her work. Topics covered should be broadly situated within remote sensing, disaster/environmental sciences, sustainability, environmental health, and GISc, including but not limited to subjects related to her research and impact. Please contact special issue editors for questions and suggestions.

Interested authors should send a manuscript title and short abstract (about 250 words, including the authors' names and affiliations) to the special issue editors (mleitne@lsu.edu; jaread@syr.edu) by July 15, 2023 (see complete publication timeline below).

Manuscript length should be around 5,000-6,000 words. All submissions will be subject to standard *PE&RS* peer review processes. See Instructions for authors (https://www.asprs.org/asprs-publications/pers/pers-instructions-for-authors-submitting-a-manuscript-for-peer-review). All submissions should be made online at the Photogrammetric Engineering and Remote Sensing Manuscript Central site (https://www.editorialmanager.com/asprs-pers/). Authors must select "Special Issue" when they reach the "Article Type" step in the submission process and identify the "Scholarship and Impacts of Professor Nina S. N. Lam Special Issue" in their cover letter. New users should first create an account. Once logged on to the site, submissions should be made via the Author Dashboard. Online user guides and access to a help desk are available on this website.

Timeline for publication of *PE&RS* Special Issue

Manuscript Proposal Deadline (Title and Abstract)	July 15, 2023
Submission Deadline	January 31, 2024
Information about Acceptance	On a rolling basis
Submission of Revised Manuscript Deadline	June 30, 2024
Publication in *PE&RS*	2024

JOURNAL STAFF

Editor-In-Chief
Alper Yilmaz, Ph.D., PERSeditor@asprs.org

Associate Editors
Valérie Gouet-Brunet, Ph.D., valerie.gouet@ign.fr
Petra Helmholz, Ph.D., Petra.Helmholz@curtin.edu.au
Dorota Iwaszczuk, Ph.D., dorota.iwaszczuk@tum.de
Desheng Liu, Ph.D., liu.738@osu.edu
Clement Mallet, Ph.D., clemallet@gmail.com
Sidike Paheding, Ph.D., spahedin@mtu.edu
Norbert Pfeifer, np@ipf.tuwien.ac.at
Rongjun Qin, Ph.D., qin.324@osu.edu
Ribana Roscher, Ph.D., ribana.roscher@uni-bonn.de
Zhenfeng Shao, Ph.D., shaozhenfeng@whu.edu.cn
Filiz Sunar, Ph.D., fsunar@itu.edu.tr
Prasad Thenkabail, Ph.D., pthenkabail@usgs.gov
Dongdong Wang, P.h.D., ddwang@umd.edu
Qunming Wang, Ph.D., wqm11111@126.com
Ruisheng Wang, Ph.D., ruiswang@ucalgary.ca
Jan Dirk Wegner, jan.wegner@geod.baug.ethz.ch
Bo Wu, Ph.D., bo.wu@polyu.edu.hk
Michael Yang, Ph.D., michael.yang@utwente.nl
Hongyan Zhang, zhanghongyan@whu.edu.cn

Contributing Editors

Highlight Editor
Jie Shan, Ph.D., jshan@ecn.purdue.edu

Feature Articles
Michael Joos, CP, GISP, featureeditor@asprs.org

Grids & Datums Column
Clifford J. Mugnier, C.P., C.M.S, cjmce@lsu.edu

Book Reviews
Sagar Deshpande, Ph.D., bookreview@asprs.org

Mapping Matters Column
Qassim Abdullah, Ph.D., Mapping_Matters@asprs.org

GIS Tips & Tricks
Alvan Karlin, Ph.D., CMS-L, GISP akarlin@Dewberry.com

SectorInsight
Youssef Kaddoura, Ph.D., kaddoura@ufl.edu
Bob Ryerson, Ph.D., FASPRS, bryerson@kimgeomatics.com
Hamdy Elsayed, Hamdy.Elsayed@teledyne.com

ASPRS Staff

Assistant Director — Publications
Rae Kelley, rkelley@asprs.org

Electronic Publications Manager/Graphic Artist
Matthew Austin, maustin@asprs.org

Advertising Sales Representative
Bill Spilman, bill@innovativemediasolutions.com

NEW ASPRS MEMBERS

ASPRS would like to welcome the following new members!

Jason Armbrust
Prosenjit Barman
Gleyn Edward Bledsoe, Ph.D.
Scott Chapman
Jake Anthony Chauvin
Evan William Cizler
Leeann Deslauriers
Kamila Dilmurat
Ameer Faisal, P. E.
Daniel Granda, P. E.
Yunyi Guan
Nicholas Daniel Hestand
Travis James Hoffman
Ronikka A. Hubert
Daniel Huseman
Yufang Jin
Drew Michael LeBoeuf
Jiawei Li
Pengfei Ma
Travis Martin
Michael Mercincavage
Robert Morse
Landon Michael Neil
Stephanie Padilla
Ethan Roberts
Taurai Justice Sadzauchi
Sumana Sahoo
Kelly L. Soverns
Greg Taillacq
Mark Topping
Reece D. Toups
My Thu Tran
Heidi Tubbs
Gregory Wehrli
Tim Wright
Molan Zhang

FOR MORE INFORMATION ON ASPRS MEMBERSHIP, VISIT
HTTP://WWW.ASPRS.ORG/JOIN-NOW

asprs THE IMAGING & GEOSPATIAL INFORMATION SOCIETY

ASPRS Staff Directory

Membership/*PE&RS* Subscription/ Conferences
Yuki Day
office@asprs.org

Advertising/Exhibit Sales
Bill Spilman
bill@innovativemediasolutions.com

Peer-Review Article Submission
Alper Yilmaz
PERSeditor@asprs.org

Highlight Article Submission
Jie Shan
jshan@ecn.purdue.edu

Feature Article Submission
Featureeditor@asprs.org

Certification
applications@asprs.org

Calendar
calendar@asprs.org

ASPRS Bookstore
office@asprs.org

ASPRS Foundation
foundation@asprs.org

Mailing Address
PO Box 14713
Baton Rouge, LA 70898

301-493-0290, 225-408-4422 (fax), www.asprs.org

ASPRS ANNUAL CONFERENCE 2023

at Geo Week February 13-15, 2023 Denver, CO, US

ASPRS Presidential Address

Lorraine B. Amenda

ASPRS Awards Program 2023

Society Awards
Region Awards
Roger Hoffer Membership Award
Outstanding Paper Awards
Scholarships

Geo Week Joint Awards

ASPRS Fellow Award
Estes Memorial Teaching Award
The ASPRS Lifetime Achievement Award
ASPRS Photogrammetric Award (Fairchild)
The ASPRS Outstanding Technical Achievement Award
The International Educational Literature Award (IELA)
George E. Brown, Jr. Congressional Honor Award

Annual Business Meeting and Installation of Officers

Recognition of Retiring Council Chairs
Installation of New Council Chairs
Recognition of Retiring Division Directors
Installation of New Division Assistant Directors
Recognition of Retiring President
Installation of Officers
Presentation of Birdseye Citation and President's Key to Retiring President

ASPRS PRESIDENTIAL ADDRESS

A Path to ASPRS Leadership

February 15, 2023

Lorraine B. Amenda, PLS, CP

There are probably as many paths to leadership positions in ASPRS as there are folks in those positions. I personally feel that mine is a somewhat improbable path. Following my High School graduation in Coalinga, CA, in 1982 I had no clear sense of what I wanted for my future other than no longer living in Coalinga. My original plan was to attend community college in Southern California while rooming with my sister who had just graduated from Pepperdine University. As the summer was ending, that plan fell apart and I ended up living with my grandmother and attending Fresno City College.

I primarily took business and secretarial courses, with a side of Calculus for fun. I expect I'm the only student there who ever took typing, shorthand, and calculus during the same semester! After 3 semesters I got a full-time job as the Administrative Assistant for the United Way of Fresno County. Fresno is an affordable place to live, but a support position at a non-profit didn't really provide enough funds to support myself comfortably. After 2 ½ years I decided to go back to college full-time in preparation to start a professional career. I originally expected to study business, probably accounting then took a detour into engineering. After 1 more year at Fresno City College to finish Calculus and work on engineering prerequisites, I decided to attend the Engineering Open House at Fresno State to see what options were available. A presentation from the Surveying Engineering (now Geomatics) program had some very interesting activities – including close-range photogrammetric mapping of horses. I decided to give it a try with a potential fall-back to Civil Engineering. After 3 years at Fresno State, I graduated with honors and a B.S. in Surveying Engineering and a job with the aerial mapping group at Towill, Inc., in San Francisco – where I continue working today, nearly 33 years later.

During my final semester at Fresno State I was debating between photogrammetry and field surveys, not making a final decision until the end of the year. I also attended the ASPRS/ACSM join conference held at the Denver Convention Center, where we are right now. I had joined ASPRS and ACSM as a student member that year. Then, like many students, decided to let my membership lapse when I received my first billing statement for a full membership. About 10 years later while attending the CSUF Geomatics Engineering Conference in January 2000 one of my co-workers was approached to help revitalize the Northern California Region of ASPRS that had been dormant for a couple of years. She asked me if I would do it with her, and I agreed. At that time we thought we were agreeing to join ASPRS and attend a few meetings. Apparently what we had agreed to was being a candidate for the Region's Board of Directors. At the conclusion of the election, I was a Region Director and my co-worker ended up leaving Towill to work with her husband on his newly established surveying business, never joining ASPRS or attending a Region meeting. I joined ASPRS and began my long stretch of involvement with ASPRS, primarily at the Region Level.

After a few years I moved from a Director to the National Director that represented the Northern California Region on the National Board of Directors. I was part of the core group that merged the Northern California Region (Northern California, Northern Nevada, and Hawaii) with the Southwest US Region (Southern California, Southern Nevada, and Arizona) to form the Pacific Southwest Region. Shortly after that I moved over to the Region's Secretary-Treasurer position and finally into the Region President position. While I was PSW Region President, I became involved with the Region Officers Council and stepped into the Deputy Chair position. Very shortly thereafter the Council Chair stepped down, and I was suddenly the Chair of the ROC at the point where it was still trying to find its

footing. I finished the remainder of the term for the Chair who stepped down and then finished my own two-year term, also agreeing to serve as the ASPRS Secretary during the final year of that term – that may have been one ASPRS job too many! It was at that point that I was invited to run for the ASPRS Vice Presidency.

ASPRS involvement can offer many different things depending upon your level of involvement as well as your individual circumstances. For me, ASPRS has become a place where I've been able to expand my professional network, which would otherwise be pretty limited since I've worked for the same employer for my entire career; particularly when you factor in that Towill has a pretty high rate of employees that have been there for 25 years or more. ASPRS has also been a place where I've been able to develop my public speaking/presentation skills and have become comfortable leading meetings prior to the time where that regularly became part of my day job.

ASPRS has had a lot of changes to make in the past few years as the world has shifted on-line and the nature of professional organizations have had to adapt. We have navigated many of the hurdles to come our way, and we know there are more coming our way soon, some that we can predict and others that will come as a surprise. But even as we adapt to these changes, ASPRS will continue to provide leadership in the adoption of new technologies or the application of our core technologies to even more users. There is also a need for the local programming made available by the ASPRS Regions – both in-person and increasingly on-line; especially as we emerge from COVID. Region sponsored technical sessions and conferences are a place where you can network with other geospatial professionals in your geographic area as well as learn what geospatial activities the local firms are utilizing.

Leadership at ASPRS can start with something as simple as volunteering to attend a local presentation sponsored by your Region or showing up at a meeting of one of the Technical Divisions. That one small step could be the start of a road that would lead you to be ASPRS President somewhere down the line. It just takes one small step followed by another small step that comes your way. Where will your own ASPRS path lead?

Outgoing ASPRS President Chris Parrish congratulating newly sworn in President Lorraine B. Amenda.

ASPRS AWARDS PROGRAM 2023

Denver, Colorado • February 13–15, 2023

AWARDS AND SCHOLARSHIPS

Through the ASPRS Foundation, ASPRS provides support to undergraduate and graduate student members of the society through their Scholarship program, and recognizes professionals who are contributors to the field of spatial and image sciences. Awards for Outstanding Papers, Professional Achievement, and Service activities are determined by committee selection; scholarships and academic awards are also determined by committee selection but are chosen from current applications. A comprehensive review of the awards program is available on the ASPRS webpage: https://www.asprs.org/education/asprs-awards-and-scholarships.

Society Awards

ASPRS Presidential Citations

Rae Kelley
For outstanding work as Director of Publications, including important changes to *PE&RS* that benefit authors, readers, and subscribers.

John McCombs
For supporting the society through meritorious service as ASPRS Treasurer.

Purpose: First awarded in 1992, Presidential Citations are presented by the ASPRS President to members of ASPRS and other societies, family members, and friends in recognition of special, personal, and meritorious contributions to the operation or advancement of the Society and its interests during the presidential year.

Donor: ASPRS. The Presidential Citation is a certificate.

John McCombs (right) receiving the ASPRS Presidential Citiation from outgoing ASPRS President Chris Parrish.

ASPRS Outstanding Service Award

Lauren McKinney-Wise
For development of new bylaws and operating procedures templates for student chapters, streamlining the process for creating new student chapters, and supporting the awards program.

Evon Silvia
For outstanding work as Chair of the ASPRS LAS Working Group, including publication of Version 2 of the LAS Topobathy Domain Profile.

Qassim Abdullah, Colin Lee, Riadh Munjy, Josh Nimetz, Michael Zotlek
For serving on the committee developing Edition 2 of the ASPRS Positional Accuracy Standards for Digital Geospatial Data.

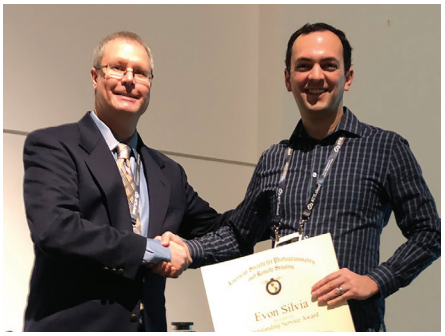

Evon Silvia (right) receiving the ASPRS Outstanding Service Award from outgoing ASPRS President Chris Parrish.

Qassim Abdullah (left) and Josh Nimetz (right) receiving the ASPRS Outstading Service Award from outgoing ASPRS President Chris Parrish.

Jim Gillis, Jeff Irwin, Jamie Gillis, Davic Kuxhausen, Colin Lee, Kyle Ince, Michael Zarlengo
For serving on the Survey Addendum Working Group working on the Positional Accuracy Standards.

Purpose: Established in 1991, The Outstanding Service Award is given in recognition of outstanding and unusual efforts in helping ASPRS develop and carry out its program over a sustained period. Recipients have performed outstanding service at the chapter, regional, or national level. Awardees' service includes any activities, including professional, that have helped the Society achieve its goals and objectives.

Donor: ASPRS. The Outstanding Service Award consists of a certificate.

Region Awards

Region of the Year: Florida Region

Region Web Site and Newsletter of the Year: Gulf South Region

Roger Hoffer Membership Award

Honorable Mention: Karen Schuckman

Purpose: First awarded in 1968 as the ASPRS Ford Bartlett Membership Award (which was originally sponsored by the firm of Lockwood, Kessler, and Bartlett, Inc.) to honor members for actively promoting membership in ASPRS. This award now marks the exceptional efforts of ASPRS Past President Roger Hoffer in managing the Membership Committee and recruiting hundreds of student members.

Donor: ASPRS. A member is eligible to receive the Award after sponsoring ten or more members in one year. Each recipient receives a hand-engrossed certificate and a one-year membership in the Society. An Honorable Mention is awarded to those who sponsor at least five new members.

Outgoing ASPRS President Chris Parrish presenting the Roger Hoffer Membership Award to Karen Schuckman (right).

Outgoing ASPRS President Chris Parrish presenting the ASPRS Outstanding Service Award to Davic Kuxhausen (center) and Jeff Irwin (right).

Outgoing ASPRS President Chris Parrish presenting the Region of the Year Award to Florida Region officer Matthew LaLuzerne (right).

Outgoing ASPRS President Chris Parrish presenting the Region of the Year Award to Florida Region representative Jeffrey Lovin (right).

Outgoing ASPRS President Chris Parrish presenting the Region Web site and Newsletter of the Year Award to Cody Condron (right).

Outstanding Paper Awards

The Esri Award for Best Scientific Paper in GIS

1st Place
Ravi Peters, Balázs Dukai, Stelios Vitalis, Jordi van Liempt, and Jantien Stoter for "Automated 3D Reconstruction of LoD2 and LoD1 Models for All 10 Million Buildings of the Netherlands." *PE&RS*, 88(3): 165–170.

2nd Place
Steven Spiegel, Casey Shanks, and Jorge Chen for "Effectiveness of Deep Learning Trained on SynthCity Data for Urban Point-Cloud Classification". *PE&RS*, 88(2): 113-120.

3rd Place
Feilin Lai and Xiaojun Yang for "Improving Land Cover Classification over a Large Coastal City Through Stacked Generalization with Filtered Training Samples." *PE&RS*, 88(7): 451–459.

Purpose: Established in 1991, the fully endowed Esri Award honors individuals who publish papers of scientific merit that advance our knowledge about GIS technology.

Donor: Esri, Inc. through the ASPRS Foundation. The First-Place award includes a cash award of $1,500 and a certificate; Second Place is a cash award of $900 and a certificate; Third Place is a cash award of $600 and a certificate.

John I. Davidson President's Award for Practical Papers

1st Place - Tie
Xuzhe Duan, Qingwu Hu, Pengcheng Zhao, and Shaohua Wang for "A Low-Cost and Portable Indoor 3D Mapping Approach Using Biaxial Line Laser Scanners and a One-Dimension Laser Range Finder Integrated with Microelectromechanical Systems." *PE&RS*, 88(5): 311–321.

1st Place - Tie
Thomas R. Loveland, Martha C. Anderson, Justin L. Huntington, James R. Irons, David M. Johnson, Laura E. P. Rocchio, Curtis E. Woodcock, and Michael A. Wulder for "Seeing Our Planet Anew: Fifty Years of Landsat." *PE&RS*: 88(7): 429-436.

Purpose: The John I. Davidson President's Award for Practical Papers was established in 1979 to encourage and commend individuals who publish papers of practical or applied value in *PE&RS*.

Donor: The ASPRS Foundation in memory of ASPRS Past President John I. Davidson. The First-Place award includes a cash award of $1,000 and a certificate; Second Place is a cash award of $600 and a certificate; Third Place is a cash award of $400 and a certificate.

Steven Spiegel (right) accepting The Esri Award for Best Scientific Paper in GIS (2nd Place) from incoming ASPRS President Lorraine B. Amenda.

Christopher McGinty accepting the John I. Davidson President's Award for Practical Papers (Loveland, *et. al*) from incoming ASPRS President Lorraine B. Amenda on behalf of the winners.

Talbert Abrams Award

Grand Award:
Itiya Aneece and Prasad S. Thenkabail for "New Generation Hyperspectral Sensors DESIS and PRISMA Provide Improved Agricultural Crop Classifications." *PE&RS*, 88(11): 715-729.

Incoming ASPRS President Lorraine B. Amenda presenting the Talbert Abrams Award to Itiya Aneece (center) and Prasad S. Thenkabail (right).

First Honorable Mention:
Clement E. Akumu and Sam Dennis for "Urban Land Cover/Use Mapping and Change Detection Analysis Using Multi-Temporal Landsat OLI with Lidar-DEM and Derived TPI." *PE&RS*, 88(4): 245-253.

Second Honorable Mention:
Thomas R. Loveland, Martha C. Anderson, Justin L. Huntington, James R. Irons, David M. Johnson, Laura E. P. Rocchio, Curtis E. Woodcock, and Michael A. Wulder for "Seeing Our Planet Anew: Fifty Years of Landsat." *PE&RS*: 88(7): 429-436.

Purpose: The Talbert Abrams Award was established in 1945 to encourage the authorship and recording of current, historical, engineering, and scientific developments in photogrammetry. The Award is determined from papers published in the Photogrammetric Engineering and Remote Sensing (*PE&RS*) journal.

Donor: The ASPRS Foundation. The award consists of a certificate and a check for $4,000 for the Grand Award, and a certificate for the First and Second Honorable Mentions.

Christopher McGinty (right) accepting the Talbert Abrams Award (2nd Honorable Mention) from incoming ASPRS President Lorraine B. Amenda on behalf of the winners.

Scholarships

Robert E. Altenhofen Memorial Scholarship

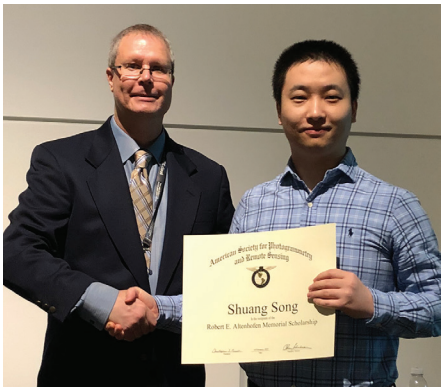

Shuang Song (right) accepting the 2023 Robert E. Altenhofen Memorial Scholarship from outgoing ASPRS President Chris Parrish.

2023 recipient: Shuang Song
Shuang Song earned a bachelor's degree from the School of Geographical Sciences at Guanghzhou University, China, an M. Eng. in photogrammetry and remote sensing from Wuhan University, China, and is currently a doctoral candidate in photogrammetry and remote sensing in the Department of Civil, Environmental, and Geodetic Engineering at The Ohio State University. Song has demonstrated a strong alignment with the criteria of Robert E. Altenhofen Memorial Scholarship with his strong background in rigorous photogrammetric concepts. Song's research focuses on mesh modeling from unstructured point clouds and its application to fuse multi-source 3D data to generate geospatially coherent datasets for reality-based modeling. Song also seeks to bring photogrammetry and image processing into other fields and has collaborated with researchers in anthropology, chemical engineering, public health, and civil engineering. Song has already built a strong publication record, including one book chapter, two journal papers, and multiple top-tier conference proceedings, with two additional journal papers under review.

Purpose: First given in 1986, the Robert E. Altenhofen Memorial Scholarship is intended to encourage and commend college students who display exceptional interest and ability in the theoretical aspects of photogrammetry.

Donor: The ASPRS Foundation. This award was originally established by Mrs. Helen Altenhofen as a memorial to her husband, Robert E. Altenhofen, past president of ASPRS. He was an outstanding practitioner of photogrammetry and made notable contributions to mathematical aspects of the science. The Altenhofen Scholarship consists of a certificate, a check for $2,000, and a one-year membership renewal in the Society.

Abraham Anson Memorial Scholarship

2023 recipient: Not awarded this year

Purpose: To encourage students who have an exceptional interest in pursuing scientific research or education in geospatial science or technology related to photogrammetry, remote sensing, surveying, and mapping to enter a professional field where they can use the knowledge of their discipline to excel in their profession.

Donor: This award is presented by the ASPRS Foundation from funds donated by the Anson bequest and contributions from the Society and the Potomac Region as a tribute to Abe Anson's many contributions to the field of photogrammetry, remote sensing, and long, dedicated service to the Society. The award consists of a certificate, a check for $2,000, and a one-year membership renewal in the Society.

John O. Behrens Institute for Land Information (ILI) Memorial Scholarship

2023 recipient: James Jones
James Jones is an undergraduate student in geomatics at Nicholls State University (NSU). Jones works as an undergraduate research assistant in the NSU Geospatial Technology Lab completing projects such as geocoding electric meter locations for a local municipality, creating a geographic information system of the utility easements for a local utilities department, researching sugarcane quality using hyperspectral data, and identifying vegetation with hyperspectral unmanned autonomous system (UAS) data. Jones is currently working on a project to support the NSU police department. Jones has presented his research at multiple meetings including the University of Louisiana at Lafayette Fall Undergraduate Research Conference in 2021 and 2022. He is the recipient of Nicholls Scholars Academic Honors, the 2020 Morris P. Hebert Scholarship for academic excellence in Geomatics, and the 2022 ASPRS Abraham Anson Memorial Scholarship. He is active in serving the community through local church groups and has been recognized for his service with the Knights of Columbus award, Louisiana Boys State, Rotary Club Service Above Self Award and Diocesan Youth Leadership Award. He is also an active member of NSPS, LSPS and ASPRS.

Purpose: To encourage students who have an exceptional interest in pursuing scientific research or education in geospatial science or technology or land information systems/records to enter a professional field where they can use the knowledge of this discipline to excel in their profession.

Donor: This award is presented by the ASPRS Foundation from funds donated by the (now dissolved) Institute for Land Information (ILI). The John O. Behrens ILI Memorial Scholarship was established by the ILI as a tribute to the many contributions of Mr. John O. Behrens to the field of geographic and land related information and technology. Mr. Behrens was a founder of the ILI and the author of many articles about the value of spatial information, land assessment and taxation, and land information policy. The Award consists of a certificate, a check for $2,000, and a one-year membership renewal in the Society.

Robert N. Colwell Memorial Fellowship

2023 recipient: Minho Kim
Minho Kim is a doctoral candidate in Landscape Architecture and Environmental Planning at the University of California, Berkeley. His dissertation topic is "Towards Transformative Resilience in the Wildland-Urban Interface (WUI): Combining High-Resolution Remote Sensing and Machine Learning-based Fire Spread Simulation." Kim plans to generate vegetation fuel maps and natural hazard information at unprecedented high spatial resolution, create a machine learning-based fire spread simulation model, and develop geospatial measures of wildfire risk for individual homeowners and communities. Kim's fire spread simulator will be applicable to different regions around the world, and will be capable of making timely updates based on changing local fuel conditions. Kim's ability to translate remote sensing and GIS into practical applications is demonstrated by the patent that he shares with colleagues based on his study on forecasting photovoltaic power generated from solar farms in Korea that combined meteorological data, sun geometry and time variables, and in-situ data with geostationary satellite images in a deep neural network. Kim's success as a teaching assistant for seven different geospatial courses led to his appointment as the lead instructor for a large multidisciplinary GIS course at UC Berkeley. He is quickly becoming a very versatile teacher who provides inclusive mentorship to students from diverse social, educational, and ethnic backgrounds. Kim's remote sensing skills and overall expertise have led to lead authorship of four peer-reviewed articles in top-tier journals.

Purpose: Established in 2006 to encourage and commend college/university graduate students or post-doctoral researchers who display exceptional interest, desire, ability, and aptitude in the field of remote sensing or other related geospatial information technologies, and who have a special interest in developing practical uses of these technologies.

Donor: This award is presented by the ASPRS Foundation, from funds donated by students, associates, colleagues, and friends of Robert N. Colwell. Over the course of more than a half century, Dr. Robert N. Colwell developed a reputation as one of the world's most respected leaders in remote sensing, a field that he stewarded from the interpretation of aerial photographs during World War II, to the advanced acquisition and analysis of many types of geospatial data from military and civilian satellite platforms. His career included nearly 40 years of teaching and research at the University of California, Berkeley, a distinguished record of military service reaching the rank of Rear Admiral, and prominent roles in private industry and as a consultant for many U.S. and international agencies. Among his many accolades, Dr. Colwell had the distinction of being one of the 25 Honorary Members of ASPRS. The Award consists of a certificate, a check for $8,000, and a one-year membership renewal in the Society.

William A. Fischer Memorial Scholarship

2023 recipient: Anuska Narayanan

Anuska Narayanan is a doctoral student in the Department of Geography at the University of Florida specializing in sustainability and global environmental change. Narayanan previously earned M.S. and B.S. degrees in geographic information systems and environmental science, respectively, at the University of Alabama. Required coursework in GIS and remote sensing during her undergraduate degree introduced Narayanan to the value of geospatial sciences across a range of domains and led to her master's research that focused on quantifying the impacts of deforestation on hydrologic systems in the Amazon River Basin. She has presented her research at local, national, and international conferences and engaged in developing peer-reviewed publications. Narayanan has also gained experience through various internships and work as a GIS contractor as well as serving as a teaching assistant and guest lecturer. Narayanan is currently studying earth-climate interactions. Her training in geospatial technologies and techniques are enabling Narayanan to combine her multidisciplinary training in hydrology, land use analysis, and climatology boundaries in order to understand land-climate interactions. Narayanan aims to become a professor in geography with a focus on geospatial applications to share her passion and motivate the next generation of geospatial scientists.

Purpose: The William A. Fischer Scholarship facilitates graduate studies and career goals of a worthy student adjudged to address new and innovative uses of remote sensing data and techniques that relate to the natural, cultural, or agricultural resources of the Earth. It was established in 1984.

Donor: The ASPRS Foundation through individual and corporate contributions in memory of William A. Fischer. The William A. Fischer Memorial Scholarship consists of a certificate, a check for $2,000, and a one-year membership renewal in the Society.

Government Services Scholarship

2023 recipient: Rebecca Bosworth

Rebecca Bosworth is completing a Master of Science degree in Geographic Information Science and Technology at the University of Southern California (USC). Bosworth previously completed a Bachelor of Arts degree in Atmospheric Science at the University of California Berkeley. As an undergraduate student, Bosworth completed a summer internship at NASA Goddard Space Flight Center testing satellite sensors. This experience introduced the field of remote sensing and led to Bosworth becoming a U.S. Air Force Intelligence Officer. Bosworth's experience using remote sensing within defense operations motivated her application to the USC Spatial Science Institute to pursue her master's degree, which coincided with her transfer to the U.S. Space Force as Deputy Commander of the SATCOM Intelligence Operations Detachment. At USC, Bosworth pairs her professional experience with her formal education to focus on projects working with remote sensing technologies. She led a team of five graduate students to attain recognition for the Most Innovative Analysis at the 2022 Los Angeles Geospatial Summit Esri Student Map Competition. Bosworth's research focuses on improving disaster relief response timelines based on geospatial information using satellite remote sensing techniques. She seeks to utilize networks of small satellites in low earth orbit with high revisit rates that offer reliable data and promote space sustainability by reducing satellite congestion. Bosworth will apply her education towards continued service in the U.S. Space Force partnering with civil, government, and commercial partners to protect human security. Bosworth aims to use satellite remote sensing to detect indicators threatening human security and social justice, promote equitable solutions, and advance sustainable policies protecting vulnerable communities.

Purpose: The newly established Government Services Scholarship, awarded for the first time this year, encourages upper-division, undergraduate- and graduate-level college students to pursue a course of study in photogrammetry and related topics leading to a career in the geospatial mapping profession in the government sector (federal, state, or local) within the United States. The Award also encourages geospatial professionals already in government service to pursue advanced degrees and provides a preference to U.S. veterans.

Donor: The ASPRS Foundation through the support of an anonymous donor who is a long-time supporter of ASPRS and the ASPRS Foundation. The Government Services Scholarship consists of a certificate, a check for $7000, and a one-year membership renewal in the Society.

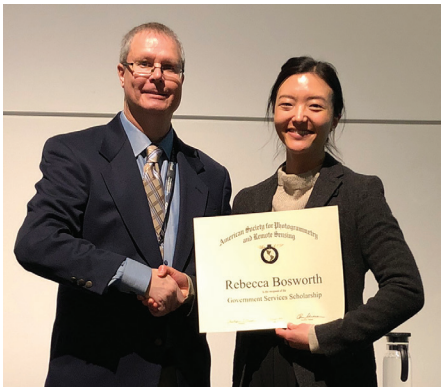

Rebecca Bosworth accepting the Government Services Scholarship from outgoing ASPRS President Chris Parrish.

Francis H. Moffitt Memorial Scholarship

2023 recipient: Oren Nardi
Oren Nardi is pursuing his BS degree in Geospatial Science and Technology at Cal Poly Humboldt in Arcata, California. His interest in geospatial information science (GIS) stems from his volunteer work with the California Conservation Corps working on the rehabilitation of trail systems in the wilderness portions of Yosemite National Park. With his experiences in working outdoors Nardi gained an appreciation in the field of natural resources he began his academic pursuits in Forestry but ultimately changed majors to Environmental Science with a concentration in GIS. Through summer internships Nardi gained experience with GIS tools and began a keen interest in unmanned autonomous system (UAS) technology. He has subsequently earned his license to fly drones and intends to use UAS technology in his research. Nardi's long-term professional career goal in the geospatial field is to spearhead commercial-grade UAS applications into solving real-world questions such as monitoring landscape-based vegetation treatments.

Purpose: The award was first presented in 2008 with the purpose of encouraging upper-division, undergraduate-level, and graduate-level college students to pursue a course of study in surveying and photogrammetry leading to a career in the geospatial mapping profession.

Donor: The ASPRS Foundation from funds donated to the Foundation from former students, associates, colleagues, and friends of Francis Moffitt. The award consists of a certificate, a check for $9,000, and a one-year membership renewal in the Society.

The Kenneth J. Osborn Memorial Scholarship

2023 recipient: Not awarded this year

Purpose: to encourage and commend college students who display exceptional interest, desire, ability, and aptitude to enter the profession of surveying, mapping, photogrammetry, or geospatial information and technology. In addition, the Award recognizes students who excel at an aspect of the profession that Ken demonstrated so very well, that of communications and collaboration.

Donor: The ASPRS Foundation from funds donated by the friends and colleagues of Kenneth J. Osborn. Recognized nationally and internationally, Ken was an outstanding practitioner of surveying, mapping, photogrammetry, and geospatial information and technology, and a great friend of the Society. As a professional cartographer with the U.S. Geological Survey, Ken made significant contributions to these fields. The award was first offered in 2005. The Award consists of a certification, a check for $2,000, and a one-year membership renewal in the Society.

Ta Liang Memorial Award

Outgoing ASPRS President Chris Parrish presenting the Ta Liang Memorial Award to Sierra Melton (right).

2023 recipient: Sierra Melton
Sierra Melton is a doctoral candidate and research/teaching assistant in the Geosciences Department at the Pennsylvania State University, where she also completed a Master of Science degree. Melton was the recipient of a National Science Foundation (NSF) Graduate Research Fellowship that supported completion of her master's degree that focused on iceberg calving and meltwater drainage at the ice-cliff terminus of Helheim Glacier, Greenland. Melton has an extensive work and research experience record including internships with the National Geospatial-Intelligence Agency and NSF funded research experiences in the United States and abroad. Melton has communicated her research through peer-reviewed publications and presentations. Melton is motivated to employ remote sensing, photogrammetry, and geophysical and geodetic survey methods to study hydrological and glaciological processes impacted by climate and environmental change. This summer, she will travel to Helheim Glacier in southeast Greenland to conduct field research to support her doctoral research analyzing the glacier using remote sensing and numerical modeling approaches. Her research will include development of digital elevations models derived photogrammetrically from UAV data to study how glacier surfaces change as a result of fracture and calving events. Melton has also been active in service activities including mentoring undergraduate researchers, being a Local Science Partner ambassador with the American Geophysical Union, co-chairing the Colorado College Students for Environmental Action (EnAct) and serving as a mentor with the Colorado College Learning Initiative in the Mountains (CCLIM).

Purpose: To facilitate research-related travel by outstanding graduate students in remote sensing, including field investigations, agency visits, participation in conferences, or other travel that enhances or facilitates graduate research.

Donor: Individual and corporate contributions to the ASPRS Foundation in memory of Ta Liang, a skilled civil engineer, an excellent teacher, and one of the world's foremost air photo interpreters, the award consists of a certificate, a check for $2,000 grant, and a one-year membership renewal in the Society.

Paul R. Wolf Memorial Scholarship

2023 recipient: Sheng Tan

Sheng Tan is presented the Paul R. Wolf Memorial Scholarship in recognition of his outstanding academic credentials and his plans and enthusiasm to become an education professional in surveying, mapping, photogrammetry, and related fields. Tan is currently a doctoral candidate in geomatics at Purdue University with a projected graduation date of May 2027. Tan has demonstrated a continued interest, dedication, enthusiasm, passion, and aptitude to become an education professional as exemplified by his outstanding work as a teaching assistant. Tan's career goal is to become a tenured teaching/research faculty member at a university, wishing to grow his skill set and continually learn new technologies in the geomatics field.

Purpose: To encourage and commend college students who display exceptional interest, desire, ability, and aptitude to enter the profession of teaching surveying, mapping, or photogrammetry.

Donor: the ASPRS Foundation from funds donated by the friends and colleagues of Paul R. Wolf. Recognized nationally and internationally, Dr. Wolf was an outstanding educator and practitioner of surveying, mapping, and photogrammetry and a great friend of the Society. As author, teacher, and mentor, Dr. Wolf made significant educational and academic contributions to these fields. The award was inaugurated in 2003 and includes a certificate, a check for $5,000, and a one-year membership renewal in the Society.

Geo Week Joint Awards

ASPRS Fellow Award

2023 recipients: Amr Abd-Elrahman and Prasad Thenkabail

Outgoing ASPRS President Chris Parrish presenting the ASPRS Fellow Award to Amr Abd-Elrahman.

Amr Abd-Elrahman

Dr. Amr Abd-Elrahman is recognized for his research contributions in artificial intelligence and machine learning and for his contributions to the Society. Amr Abd-Elrahman has developed and applied spatial analysis techniques for remote sensing datasets to address natural resource management and agricultural challenges using object-based image analysis of high-resolution imagery and image classification using machine and deep learning.

Abd-Elrahman is a Professor at the Gulf Coast Research and Education Center, School of Forest Resources and Conservation – Geomatics Program at the University of Florida (UF). Abd-Elrahman received B.Sc. and M.Sc. degrees in Civil Engineering from Ain Shams University in Cairo, Egypt in 1990 and 1994, respectively; and his Ph.D. in Civil Engineering in the Geomatics Program, with a minor in Computer and Information Engineering, from UF in 2001. Abd-Elrahman has advanced agricultural and natural resource monitoring through innovations in image classification, biophysical modeling, bathymetric mapping and machine and deep learning, especially using high-resolution imagery and lidar data acquired from UAS platforms.

Abd-Elrahman has secured over $7.1M in research funds from national and state agencies including the National Science Foundation, U.S. Department of Agriculture, U.S. Forest Service, National Oceanic and Atmospheric Administration, U.S. Army Corps of Engineers, National Institute of Food & Agriculture and the Florida Strawberry Research and Education Foundation. His work is published in top geospatial journals such as *Remote Sensing of Environment*, *ISPRS Journal of Photogrammetry and Remote Sensing, ISPRS International Journal of Geo-Information, GIScience & Remote Sensing, Remote Sensing, Sensors, Journal of Applied Remote Sensing, and the International Journal of Remote Sensing*. In recognition for his accomplishments in remote sensing, he recently received the Florida Surveying and Mapping Society Professional Excellence Award (2022), North American Colleges and Teachers of Agriculture Teaching Scholar Award (2022), and the UF College of Agricultural and Life Sciences 2022 Graduate Teacher/Advisor of the Year Award.

Abd-Elrahman is very active in ASPRS. In addition to teaching ASPRS workshops in object-based image analysis and machine and deep learning image classification, he has organized technical sessions and served as a panelist at several ASPRS conferences, served as the ASPRS Remote Sensing Application Division Director (2021–2023) and the ASPRS Education and Professional Development Committee Chair (2020–2023), and will become the ASPRS Vice-President at the 2023 Annual Conference.

Outgoing ASPRS President Chris Parrish presenting the ASPRS Fellow Award to Prasad Thenkabail.

Prasad Thenkabail

Dr. Prasad S. Thenkabail is recognized for his contributions to remote sensing science and his long-term commitment to the Society. Thenkabail is a leader in advancing remote sensing science and has been an exemplary presence in the global stage working in more than 25 countries.

Thenkabail is a Senior Scientist with the United States Geological Survey Western Geographic Science Center.

He conducts high impact research while being involved in applied research and remote sensing applications of great practical importance, including working for three International Institutes. Thenkabail has 146 peer-reviewed journal publications and has edited 9 books including the three-volume *Remote Sensing Handbook, Hyperspectral Remote Sensing of Vegetation*, and *Remote Sensing of Global Croplands for Food Security*. He received B.E. and M.E. degrees in civil engineering and hydraulics and water resources engineering, respectively, from Mysore University, India, and a Ph.D. in Agricultural Engineering from The Ohio State University. Thenkabail is Editor-in-Chief for *Remote Sensing,* an Associate Editor for *Photogrammetric Engineering and Remote Sensing* (*PE&RS*), chaired the International Society of Photogrammetry and Remote Sensing (ISPRS) Working Group VII (2013–2016), and is an editorial advisory board member for the ISPRS *Journal of Photogrammetric Engineering and Remote Sensing*. He also served as a member of the Landsat Science Team (2007–2011).

Thenkabail is an expert in remote sensing science with major contributions in hyperspectral data analysis and global food security support analysis data. Thenkabail pioneered original novel methodologies of hyperspectral data analysis of crops including development of full spectral analysis using such methods as quantitative spectral matching techniques, establishing optimal hyperspectral narrowbands that remove band redundancies to use ~20 to 30 optimal bands for the study of agriculture and vegetation, and creating new and unique hyperspectral vegetation indices. Thenkabail's work on global food security support analysis data led to production of the world's highest resolution global cropland product using multi-year Landsat 30 m data.

Thenkabail has been a member of ASPRS since 1988, an associate editor of *PE&RS* since 2017, has published award-winning papers in *PE&RS* (1994 Autometric Award as first author; 2008 ASPRS ERDAS award for best scientific paper in remote sensing as first author, 2018 ASPRS Davidson President's Award for practical papers as second author), and edited special issues for *PE&RS*.

Purpose: Started in 1992, the designation of Fellow is conferred on Society members who have been active for a total of at least ten years and who have performed exceptional service in advancing the science and use of the mapping sciences and related disciplines. It is awarded for professional excellence and for service to the Society.

Donor: ASPRS. The ASPRS Fellow Award includes a lapel pin and a certificate.

The Estes Memorial Teaching Award

2023 recipients: Randolph "Randy" Wynne and Timothy Warner

Outgoing ASPRS President Chris Parrish presenting the Estes Memorial Teaching Award to co-recipient Randolph "Randy" Wynne.

Randolph "Randy" Wynne

Dr. Randolph H. Wynne is a Professor in the Forest Resources and Environmental Conservation Department at Virginia Tech. He also serves as a member of the Landsat Science Team and Co-Director of the Interdisciplinary Graduate Education Program in Remote Sensing. He teaches courses focused on the environmental and natural resources applications of remote sensing at the freshman, senior, and graduate levels. Wynne's research interests are in the applications of remote sensing to forestry, natural resource management, ecosystem ecology, and earth system science.

Wynne is a highly knowledgeable, dynamic, and engaging teacher. His impact on the field of remote sensing in higher education has been profound, and he has made contributions in many ways. These include undergraduate teaching, undergraduate research and career mentorship, graduate teaching and mentorship (and faculty mentorship), undergraduate and graduate curriculum development, professional engagement, and research leadership. Through his classes, he has directly taught thousands of students, and through the professional academic success of some of his graduate students (and their subsequent teaching programs) he has indirectly impacted many more. He is also the co-author of an undergraduate textbook that is used domestically and internationally at numerous schools with over 40,000 copies in print.

Wynne is energetic, generous with his time, highly knowledgeable, rigorous in his expectations, passionate about the subject, fast thinking and able to draw his

students into eager participation with course material. Student testimonials demonstrate that Wynne is well respected by his students. While he is very cutting-edge in his knowledge of emerging trends in the remote sensing community, he also has a good understanding of the practical needs of the professional forestry community, and as such is able to relate to a broad umbrella of students in our department. In addition to classroom teaching, Wynne has mentored 15 M.S. and 14 Ph.D. students, and 4 post-docs. His graduate students have gone on to faculty positions at prestigious universities (e.g., University of Georgia, Texas A&M, Rochester Institute of Technology), research scientist positions (e.g., Virginia Tech, and U. Minnesota), federal and state agencies (e.g., USFS, USGS, Oak Ridge National Labs, Montana DNRC, Alaska Div. of Forestry, and Virginia Cooperative Extension), and private companies (e.g., Shell Oil, and Wells Fargo).

Wynne has an impressive research record when measured by external grantsmanship, publication record (with his students in particular), impact factors, or citations. He has won the Society of American Foresters Award in Forest Science (2017), the Virginia Tech College of Natural Resources and Environment Diversity Award (2008), and a NASA New Investigator Award (2001). In work with his students, he has earned First Honorable Mention for the 2005 ASPRS Talbert Abrams Award for best 2004 article in Photogrammetric Engineering and Remote Sensing, Second Place in the ASPRS Leica Geosystems Award for Best Scientific Paper in Remote Sensing in 2006, First Place in the ASPRS ERDAS Award for Best Scientific Paper in Remote Sensing in 2008, and the High Performance Computing Best Paper Award in the 2011 Spring Simulation Multiconference, Boston, Massachusetts.

Wynne's students benefit by being taught by a well respected and well connected leader in the discipline. His teaching efforts will have a long standing impact on the profession of remote sensing as a result of the well trained and motivated students that he has prepared and launched into successful careers across the field.

ASPRS WORKSHOP SERIES

It's not too late to earn Professional Development Hours

Miss one of our Live Online Workshops?
Not to worry! You can purchase the workshops now and watch when you are ready! Check out the workshops offered by visiting:

https://asprs.prolearn.io/catalog

Outgoing ASPRS President Chris Parrish presenting the Estes Memorial Teaching Award to co-recipient Timothy Warner.

Timothy Warner

Dr. Timothy A. Warner is a Professor Emeritus in the Department of Geology and Geography at West Virginia University (WVU). Warner taught at all levels from introductory to post-doctoral, in the disciplines of both geology and geography for over a quarter of a century. He also maintained a rigorous schedule of service and high research productivity. Warner's research interests include the spatial properties of remotely sensed images, lidar, high spatial resolution imagery, thermal imagery, machine learning classification, wildfire mapping, and information literacy with a particular interest in the use of remote sensing for promoting transparency and non-proliferation.

Warner is recognized as an exceptional teacher for the incredible kindness, generosity, and support he gave his students at WVU. He typically taught an annual Physical Geography course to more than 200 students alongside his introductory and advanced remote sensing courses. Student appreciation for Warner's teaching stemmed from both his creative style of teaching and the evolution of his courses to reflect changes within the discipline. Warner updated parts of his courses, or created entirely new courses, to ensure relevance of the material.

Warner mentored seven PhD students, five geology MS students, twenty-six geography MA students, and two post-doctoral researchers. He received the Outstanding Teacher Award in the Eberly College of Arts and Sciences at WVU, was a finalist for the West Virginia (the entire state) professor of the year, and earned the AmericaView Lifetime Achievement Award in 2019. In addition to classroom instruction, Warner also taught professional development courses and workshops for the International Atomic Energy Agency and the US Natural Resource Conservation Service, and held many scientific writing and publishing workshops.

He was also one of the originators of AmericaView, a nationwide remote sensing education, outreach, and research consortium and the PI for West Virginia View. AmericaView and West Virginia View have a strong focus in remote sensing, earth science, and geospatial education at the K-12, undergraduate, graduate, and professional levels.

While maintaining excellence in teaching and mentorship, Warner also served as an associate editor on editorial boards and, until recently, was editor-in-chief of the International Journal of Remote Sensing. He also received two Fulbright Scholarships to study and teach abroad. He published two books and has authored more than one-hundred peer-reviewed academic publications, many of which being co-authored or led by his students. Warner has an outstanding record as a scholar, mentor, and teacher who has made immense and long lasting contributions towards geographic education.

Purpose: To recognize individual achievement in the promotion of remote sensing and geographic information systems (GIS) technology and applications through educational efforts.

Donor: ASPRS with funding provided by the ASPRS Foundation and ASPRS. The Estes Memorial Teaching Award is made in honor of Professor John E. ("Jack") Estes, teacher, mentor, scientist, and friend of ASPRS. The award consists of a presentation plaque and a cash award of $3,000.

The ASPRS Lifetime Achievement Award

2023 recipients: James Campbell and Riadh Munjy

James Campbell

Dr. James Campbell is a Professor in the Department of Geography at Virginia Tech. Campbell has pursued a career in geography, remote sensing, and spatial analysis through teaching, research, and community outreach. He has worked closely with students and faculty in forestry, geology, agronomy, and environmental sciences.

As a native of Vermont, Campbell attended local schools, then Dartmouth College, before joining the U.S. Army. Campbell graduated from several service schools in the military and spent two years as an Aerial Survey Officer/ Photogrammetrist. After completing his military service, he enrolled in a Master of Science degree at the University of Kansas. He subsequently studied at the University of Nottingham in Britain before returning to the University of Kansas to complete his doctoral degree. In spring 2003, Campbell studied at the University of Rennes (France) as a guest faculty.

Campbell's recent interests focus on analysis of sequential imagery to examine human and environmental change in agricultural landscapes. His teaching has been devoted to developing student interests and skills in remote sensing, geomorphology, and spatial data analysis. Campbell is author of a leading remote sensing text, now in its 6th edition, and numerous refereed journal articles. He has successfully advised doctoral students who made significant research contributions in a wide range of journals, including *Remote Sensing, Urban Agriculture*, and *Forest Fragmentation*.

Campbell has been a long term contributor to ASPRS, including extensive committee service, and organization of a popular series of concise videos introducing topics such as aerial photography, lidar, and related topics. He was recognized by ASPRS with an Outstanding Service Award in 1994 and the Esri Award for Best Scientific Paper in Geographic Information Systems in 2016. Campbell was also recognized as an ASPRS Fellow in 1996 and received the SAIC Estes Memorial Teaching Award in 2014. Campbell has also been recognized by many other organizations. He was recognized with an AmericaView Lifetime Achievement Award, a Burr & Burton Academy Alumni Achievement Award, Virginia Tech's Alumni Award for Excellence in Undergraduate Academic Advising, an Outstanding Scholar in Geography from the Virginia Social Science Association, and an outstanding Service Medal from the Remote Sensing Specialty Group of the Association of American Geographers.

Riadh Munjy

Dr. Riadh Munjy is a Professor of Civil and Geomatics Engineering at California State University, Fresno (Fresno State). Munjy received a Master of Science in Civil Engineering in 1979, a Master of Science in Applied Mathematics in 1981, and a Ph.D. in Civil Engineering in 1982, all from the University of Washington. He has been a faculty member and an active researcher at Fresno State since 1982, attaining the rank of Professor in 1988. Munjy served as the Fresno State Geomatics Program Coordinator from 2012–2014, and the Chair of the Department of Civil and Geomatics Engineering from 2014–2022.

As a professor, Munjy has supervised hundreds of students studying in the field of geomatics, published numerous peer-reviewed papers in a wide range of technical journals in the field of photogrammetry. Munjy has over forty years of experience teaching courses in photogrammetry, GIS digital mapping, surveying and mapping, computer programming, and civil engineering. He has taught undergraduate and graduate students and has also provided workshops on diverse topics including interferometric radar mapping, GPS-controlled aerial triangulation, and close range photogrammetry.

Throughout his career, Munjy has served as a consultant to numerous national and international organizations, providing a diverse range of expertise in mapping and photogrammetry including software to support radar flight planning, orthorectification, and image management, specifications for GIS workstations, and software to

support photogrammetric adjustment and total station survey systems. Munjy's research interests are varied and include accident reconstruction using photogrammetry, close range and softcopy photogrammetry, and UAS mapping. He is a licensed civil engineer in California and a Certified Photogrammetrist. He has served as the chief scientist at CalGIS, Inc., Earth Data International, Inc., and Geomatics Technologies, LLC working on the development of the GeoSAR System. Munjy received the ASPRS Photogrammetric Fairchild Award in 2014 for his contribution to the science and art of photogrammetry in particular his work with camera self-calibration that led to the transition from conventional aerial triangulation to airborne-controlled aerial triangulation. Munjy is also credited with the introduction of the finite element approach for sensor calibration in photogrammetry, the introduction of an analytical approach to color balancing and enhancement of digital imagery, and the development of a full processing workflow for the GeoSAR system.

Munjy has been a long term supporter of ASPRS, providing service on multiple committees, serving as a *PE&RS* Associate Editor for theoretical and applied photogrammetry, and serving as the President of Pacific Southwest Region of ASPRS. In addition to the Photogrammetric Fairchild award, ASPRS presented Munjy with multiple meritorious service awards and he was named as a Fellow in 2020. Munjy has also been recognized by many other organizations including receiving a Faculty Award for Research Excellence at Fresno State four times, a Caltran Research Innovation Award, and the Halliburton Research Award .Munjy is an outstanding professional photogrammetrist whom the Society recognizes with the Lifetime Achievement Award for his excellent and far reaching achievements.

The ASPRS Lifetime Achievement Award (formerly the Honorary Lifetime Achievement Award and the Honorary Member Award) is the highest award an ASPRS member can receive, and there are only 25 living Lifetime Achievement Awardees of the Society at any given time. Candidates are chosen by a Nominating Committee made up of the past five recipients of the award and chaired by the most recent recipient.

Purpose: Initiated in 1937, this life-time award is given in recognition of individuals who have rendered distinguished service to ASPRS and/or who have attained distinction in advancing the science and use of the geospatial information sciences. It is awarded for professional excellence and for at least 20 years of service to ASPRS and consists of a plaque and a certificate.

Donor: ASPRS

ASPRS Photogrammetric Award (Fairchild)

2023 recipient: John Dolloff

ASPRS President Chris Parrish presenting the ASPRS Photogrammetric Award (Fairchild) to John Dolloff.

John Dolloff has over 40 years of experience in geospatial science and remote sensing, specializing in photogrammetry and applications of advanced linear algebra, estimation theory, and probability and statistics. He is currently employed as a senior scientist at KBR and was previously employed at BAE Systems and its legacy companies where he was a Technical Director and an Engineering Fellow. He holds a Bachelor's degree in Mathematics and a Master's degree in Applied Mathematics.

Dolloff invented the Replacement Sensor Model (RSM) and the Metric Information Network (MIN). RSM is operational today and provides full functionality (ground-to-image relationship, adjustability, predicted accuracy) equivalent to an arbitrary but original (physical) sensor model from which it is generated. As such, a "down-stream" user only requires the use of one sensor model (RSM) for exploitation of those imaging systems that provide corresponding RSM support data. The MIN sequentially fuses information from various image block adjustments into a self-generating and expanding network of ground control points that generally increases in area of coverage and that also increases in accuracy. The network also includes a rigorous full error covariance matrix for all points, including the cross-covariances (correlations) between all point pairs.

Dolloff's experience in the earlier phase of his career concentrated on tracking and navigation systems and aided his insight into future photogrammetric applications. In particular, he supported the development of Phases 0 and I of the NAVSTAR GPS system, including the design and implementation of algorithms that controlled and synchronized pseudo-lite time bases (or clocks) to each other

in real-time and to initial GPS satellites as they became available – transitioned to be operational at the Inverted Range Control Center, Yuma Proving Grounds, for the testing of early GPS receivers. Dolloff also designed and implemented numerous Kalman Filters for the real-time tracking of vehicles, ships, and aircraft for other navigation systems.

Purpose: The Photogrammetric Fairchild Award is designed to stimulate the development of the art of aerial photogrammetry in the United States. Practicability is the essence of the Award and is the basis for the review of all candidates.

Donor: ASPRS. The award consists of an engraved presentation plaque.

The ASPRS Outstanding Technical Achievement Award

Not awarded this year

Purpose: This grant is designed to reward the developer[s] of a specific breakthrough technology that causes quantum advances in the practice of photogrammetry, remote sensing or geographic information systems in the United States.

Donor: In 2011, the ASPRS Foundation received a generous individual donation from Lifetime Achievement Awardee and ASPRS Fellow Clifford W. Greve to endow a new Outstanding Technical Achievement Award. The Award was first given in 2012 and is fully endowed at the $8,000 level. This Award consists of a silver presentation plaque mounted on a wood panel and a check for $8,000.

The International Educational Literature Award (IELA)

Not awarded this year

Purpose: to improve the quantity and quality of the literature in the library of the recipient Institution that deals with the mapping sciences (i.e., photogrammetry, remote sensing, GIS, and related disciplines).

Donor: ASPRS. The Award consists of the following: A set of manuals published by ASPRS; A five-year e-subscription to Photogrammetric Engineering & Remote Sensing; Proceedings of the annual conference for a five-year period.

George E. Brown, Jr. Congressional Honor Award

Not awarded this year

Purpose: This award was established in honor of Congressman George E. Brown, Jr., and the contributions he made to advance the benefits of imagery and geospatial information to society. The award is given periodically to recognize members of the U.S. Congress whose leadership and personal efforts have advanced the science, engineering, application, education, and commerce of imaging and geospatial information.

Donor: ASPRS

ASPRS MEMBER BENEFIT!

The 4th Edition of the *Manual of Remote Sensing!*

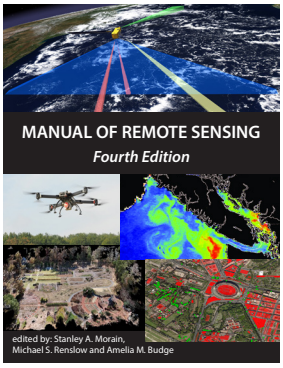

The *Manual of Remote Sensing, 4th Ed.* (MRS-4) is an "enhanced" electronic publication available online from ASPRS. This edition expands its scope from previous editions, focusing on new and updated material since the turn of the 21st Century. Stanley Morain (Editor-in-Chief), and co-editors Michael Renslow and Amelia Budge have compiled material provided by numerous contributors who are experts in various aspects of remote sensing technologies, data preservation practices, data access mechanisms, data processing and modeling techniques, societal benefits, and legal aspects such as space policies and space law. These topics are organized into nine chapters. MRS4 is unique from previous editions in that it is a "living" document that can be updated easily in years to come as new technologies and practices evolve. It also is designed to include animated illustrations and videos to further enhance the reader's experience.

MRS-4 is available to ASPRS Members as a member benefit or can be purchased by non-members. To access MRS-4, visit https://my.asprs.org/mrs4.

Annual Business Meeting and Installation of Officers

Recognition of Retiring Council Chairs
David Stolarz, Committee Chairs Council
Madeline Stewart, Early Career Professional Council
Lauren McKinney-Wise, Student Advisory Council

Installation of New Council Chairs
Youssef Kaddoura, Early Career Professional Council
Oscar Duran, Student Advisory Council

Recognition of Retiring Division Directors
Greg Stensaas, Primary Data Acquisition Division
Amr Abd-Elrahman, Remote Sensing Applications Division

Installation of New Division Directors
Srini Dharmapuri, Primary Data Acquisition Division
Tao Liu, Remote Sensing Applications Division

Installation of New Division Assistant Directors
Ravi Soneja, Primary Data Acquisition Division
Matt Elious, Professional Practice Division
Indu Jeyachandran, Remote Sensing Applications Division

Recognition of Retiring President
Jason Stoker, Immediate Past President

Installation of Officers
Amr Abd-Elrahman, Vice-President
Bandana Kar, President-Elect
Lorraine Amenda, President

Presentation of Birdseye Citation and President's Key to Retiring President
Lorraine Amenda
Christopher Parrish, Immediate Past-President

Purpose: The Col. Claude H. Birdseye President's Citation was established in 1965 as a tribute to one of the founders and the first president of the Society. Each year at the Annual Convention it is conferred on the outgoing president in recognition of her/his contributions to the Society.

Donor: ASPRS. The Birdseye Citation carries with it a gold Past President's Key, and a certificate. The retiring President will also receive the Presidential Gavel mounted on a walnut plaque.

Amr Abd Elrahman is sworn in as ASPRS Vice President

Chris Parrish is sworn in as ASPRS Immediate Past-President by President Lorraine Amenda

President Amenda presents Immediate Past-President Parrish with the ASPRS Birdseye Medal

Youssef Kaddoura is sworn in as the Early-Career Professional Council Chair

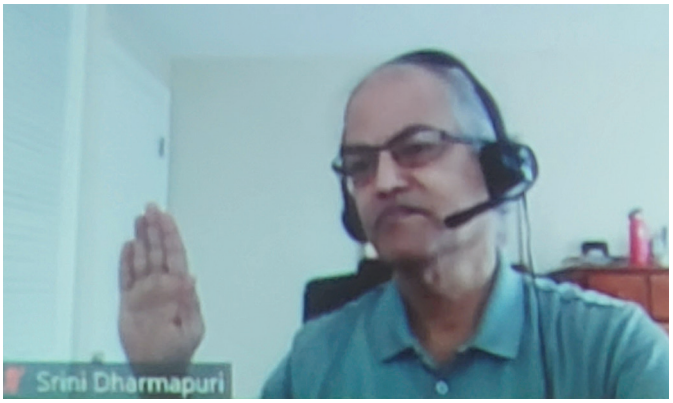

Srini Dharmapuri sworn in as Primary Data Acquisition Division Director

Tao Liu sworn in as Remote Sensing Applications Division Director

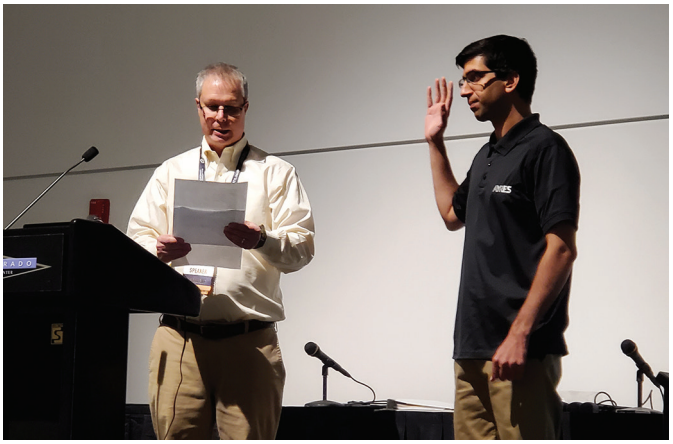

Ravi Soneja sworn in as Primary Data Acquisition Division Assistant Director

Indumathi Jeyachandran sworn in as Remote Sensing Applications Division Assistant Director.

Amanda Aragon is sworn in as the Committee Chairs Council Chair.

SUSTAININGMEMBERS

ACI USA Inc.
Weston, Florida
https://acicorporation.com/
Member Since: 2/2018

Aerial Services, Inc.
Cedar Falls, Iowa
www.AerialServicesInc.com
Member Since: 5/2001

Airworks Solutions Inc.
Boston, Massachusetts
Member Since: 3/2022

Applanix
Richmond Hill, Ontario, Canada
http://www.applanix.com
Member Since: 7/1997

Ayres Associates
Madison, Wisconsin
www.AyresAssociates.com
Member Since: 1/1953

Cardinal Systems, LLC
Flagler Beach, Florida
www.cardinalsystems.net
Member Since: 1/2001

CT Consultants
Mentor, Ohio
Member Since: 3/2022

Dewberry
Fairfax, Virginia
www.dewberry.com
Member Since: 1/1985

Esri
Redlands, California
www.esri.com
Member Since: 1/1987

GeoCue Group
Madison, Alabama
http://www.geocue.com
Member Since: 10/2003

Geographic Imperatives LLC
Centennial, Colorado
Member Since: 12/2020

GeoWing Mapping, Inc.
Richmond, California
www.geowingmapping.com
Member Since: 12/2016

GPI Geospatial Inc.
Orlando, Florida
www.aca-net.com
Member Since: 1/1994

Halff Associates, Inc.
Richardson, Texas
www.halff.com
Member Since: 8/2021

Keystone Aerial Surveys, Inc.
Philadelphia, Pennsylvania
www.kasurveys.com
Member Since: 1/1985

Kucera International
Willoughby, Ohio
www.kucerainternational.com
Member Since: 1/1992

L3Harris Technologies
Broomfield, Colorado
www.l3harris.com
Member Since: 6/2008

Merrick & Company
Greenwood Village, Colorado
www.merrick.com
Member Since: 4/1995

Nearmap
South Jordan, Utah
www.nearmap.com
Member Since: 6/2023

NV5 Geospatial
Sheboygan Falls, Wisconsin
www.quantumspatial.com
Member Since: 1/1974

Pickett and Associates, Inc.
Bartow, Florida
www.pickettusa.com
Member Since: 4/2007

PixElement
Belmont, Michigan
https://pixelement.com
Member Since: 2/2017

Riegl USA, Inc.
Orlando, Florida
www.rieglusa.com
Member Since: 11/2004

Robinson Aerial Surveys, Inc.(RAS)
Hackettstown, New Jersey
www.robinsonaerial.com
Member Since: 1/1954

Sanborn Map Company
Colorado Springs, Colorado
www.sanborn.com
Member Since: 10/1984

Surdex Corporation
Chesterfield, Missouri
www.surdex.com
Member Since: 12/2011

Surveying And Mapping, LLC (SAM)
Austin, Texas
www.sam.biz
Member Since: 12/2005

T3 Global Strategies, Inc.
Bridgeville, Pennsylvania
https://t3gs.com/
Member Since: 6/2020

Towill, Inc.
San Francisco, California
www.towill.com
Member Since: 1/1952

Woolpert LLP
Dayton, Ohio
www.woolpert.com
Member Since: 1/1985

SUSTAININGMEMBER**BENEFITS**

Membership

- ✓ Provides a means for dissemination of new information
- ✓ Encourages an exchange of ideas and communication
- ✓ Offers prime exposure for companies

Benefits of an ASPRS Membership

- Complimentary and discounted Employee Membership*
- E-mail blast to full ASPRS membership*
- Professional Certification Application fee discount for any employee
- Member price for ASPRS publications
- Discount on group registration to ASPRS virtual conferences
- Sustaining Member company listing in ASPRS directory/website
- Hot link to company website from Sustaining Member company listing page on ASPRS website
- Press Release Priority Listing in *PE&RS* Industry News
- Priority publishing of Highlight Articles in *PE&RS* plus, 20% discount off cover fee
- Discount on *PE&RS* advertising
- Exhibit discounts at ASPRS sponsored conferences (exception ASPRS/ILMF)
- Free training webinar registrations per year*
- Discount on additional training webinar registrations for employees
- Discount for each new SMC member brought on board (Discount for first year only)

*quantity depends on membership level

Automatic Satellite Images Orthorectification Using K–Means Based Cascaded Meta-Heuristic Algorithm

Oussama Mezouar, Fatiha Meskine, and Issam Boukerch

Abstract

Orthorectification of high-resolution satellite images using a terrain-dependent rational function model (RFM) is a difficult task requiring a well-distributed set of ground control points (GCPs), which is often time-consuming and costly operation. Further, RFM is sensitive to over-parameterization due to its many coefficients, which have no physical meaning. Optimization-based meta-heuristic algorithms appear to be an efficient solution to overcome these limitations. This paper presents a complete automated RFM terrain-dependent orthorectification for satellite images. The proposed method has two parts; the first part suggests automating the GCP extraction by combing Scale-Invariant Feature Transform and Speeded Up Robust Features algorithms; and the second part introduces the cascaded meta-heuristic algorithm using genetic algorithms and particle swarm optimization. In this stage, a modified K-means clustering selection technique was used to support the proposed algorithm for finding the best combinations of GCPs and RFM coefficients. The obtained results are promising in terms of accuracy and stability compared to other literature methods.

Introduction

Nowadays, accurate spatial information from satellite images is necessary for a wide range of remote sensing applications such as image matching, image registration, and mapping. Taking into consideration the rotation and curvature of the Earth, ground topography, sensor motion, and platform destabilization, the accurate spatial information depicts the Earth's three-dimensional surface (ground space) in a two-dimensional satellite image (image space). As a result, the internal and exterior geometric distortions are shown in raw remote sensing images, which necessitates adopting effective mapping models between image and Earth spaces for geometric correction (Kartal *et al.* 2018). In this regard, careful and accurate orthorectification is usually needed to georeference the satellite images. Orthorectification is a common technique for rectifying geometric distortions and displacement errors caused during the image acquisition process. It comprises geometric transformations between the image coordinate (row, column) and ground coordinate systems (longitude, latitude, and elevation).

There are two categories of transformation models: rigorous (sensor dependent) models, such as Orbital Parameter Models (Toutin 2004), and empirical (non-rigorous or also sensor independent) models, such as Rational Function Models (Tao and Hu 2001; Hu *et al.* 2004; Mezouar *et al.* 2021). The rigorous method is implemented using detailed information about the internal characteristics of the acquisition system, including sensor parameters, Charged Coupled Device (CCD) alignment within the focus plane, and offset angles with respect to the payload cube normal, all of which are well-known to the creator of the satellite (Konugurthi *et al.* 2016). Thereby, the main difficulty with using High-Resolution Satellite Images (HRSI) in rigorous models is that certain providers, like GeoEye, are unwilling to share the physical satellite parameters such as ephemeris data and interior orientation parameters (Yavari *et al.* 2012; Pan *et al.* 2016). Moreover, these models are difficult to perform in real applications because they are complex, and the imaging model might change depending on the sensor type (Boccardo *et al.* 2007). Contrarily, the Rational function model (RFM) is a type of empirical model frequently used in HRSI processing as an alternative to the rigorous model. RFM has been widely used in the remote sensing community owing to its simplicity of implementation and standardization; also, it is independent of image geometry and may be used with a variety of sensors with great results (Pan *et al.* 2016; Chen *et al.* 2006; Fraser and Hanley 2003). RFM is defined as a ratio of two cubic functions used to establish a relationship between object-space coordinates and image-space coordinates (Xiong and Zhang 2010).

There are two different computational models for RFM, namely terrain-independent and Terrain-dependent (Jannati and Valadan Zoej 2015). The unknown RFM coefficients, known as Rational Function Coefficients (RFCs) or Rational Polynomial Coefficients (RPCs), are estimated in the terrain-independent model using some physical information of the sensor as the attitude and orbital parameters, whereas they are calculated using numerous of well-distributed ground control points (GCPs) in the terrain-dependent model (Mezouar *et al.* 2021). In this case, to simplify the computations with the conventional RFM-based method, the first coefficients of the denominator polynomials are assumed to equal 1. As a result, there are 78 unknown RPCs, meaning that, to apply the traditional RFM-based method, at least 39 GCPs must be available. This concept suffers from an over-parameterization problem that requires a significant number of well-distributed GCPs to be determined, which is an explicit limitation because identifying acceptable GCPs is a time-consuming and expensive process (Gholinejad *et al.* 2019a). Moreover, the characteristics of the study areas and other difficulties in GCP selection, such as cloudy regions, dense forest areas, and certain difficult-to-reach places, the GCPs identification could be limited (Nguyen 2015). Developed automated methods for GCPs selection using image matching algorithms may be the best choice for getting GCPs and overcoming these limitations when the time cost and mistakes associated with manual processing are taken into account, especially where the access to satellite images has been simpler due to the availability of numerous sensors with varying resolutions, numbers, and sizes of images (Kartal *et al.* 2018), which has significantly risen the use of image matching techniques in GCPs selection and remote sensing applications as Harris in (Bentoutou *et al.* 2005; Misra *et al.* 2012), Speeded Up Robust Features (SURF) (Teke and Temizel 2010; Wang *et al.* 2019), and Scale Invariant Feature Transform (SIFT) (Huo *et al.* 2011; Ye *et al.* 2018).

Oussama Mezouar and Fatiha Meskine are with Communication Networks, Architecture and Multimedia (RCAM) Laboratory, Djillali Liabes University of Sidi-Bel-Abbes, Algeria (oussama.mezouar@univ-sba.dz).

Issam Boukerch is with National Higher School of Geodetic Sciences and Space Techniques - Algerian Space Agency, Arzew, Oran, Algeria.

Contributed by Rongjun Qin, August 26, 2022 (sent for review September 28, 2022; reviewed by Hessah Albanwan, Xiao Ling).

Photogrammetric Engineering & Remote Sensing
Vol. 89, No. 5, May 2023, pp. 291–299.
0099-1112/22/291–299
© 2023 American Society for Photogrammetry and Remote Sensing
doi: 10.14358/PERS.22-00113R2

In reality, RFM coefficients have no physical meaning, and since there are many coefficients in the RFM model; as a result, adjustment errors may occur owing to over-parameterization. Therefore, it is difficult to determine the optimum combination of them (Mezouar *et al.* 2021). To overcome this problem, meta–heuristics-based evolutionary algorithms appear to be a suitable solution. Among these methods, genetic algorithm (GA) and particle swarm optimization (PSO) are the most widely used for optimizing the RFM parameters and satellite images georeferencing. For example, we may reference the application of GAs in (Jannati and Valadan Zoej 2015; Naeini *et al.* 2017) and PSO in (Gholinejad *et al.* 2019a; Yavari *et al.* 2013).

This paper aims to present an automated orthorectification technique based on RFM of a terrain-dependent model using mainly two stages: one stage for automatically identifying and extracting the GCPs, while the other one tackles the limitations of RFM by proposing a novel cascaded meta-heuristic optimization based on two algorithms, GA and PSO (CM-RFM) in order to make more diversity in the population and avoid the optimum local phenomenon. To this end, GA is used for GCPs selection by adding a new selection procedure developed on the K-means clustering algorithm and PSO for determining the optimum RFM coefficients. The rest of the paper is organized as follows: in the next part, a theoretical review of RFM is presented in detail, then the automatic GCPs detection steps and the suggested CM-RFM for RFM optimization are both described in the third section. The fourth part includes a detailed presentation and discussion of the results, and finally, we finish the paper with a conclusion.

Rational Function Model

The RFM is a generalized sensor model that is used to approximate the rigorous model. The RFM model uses a pair of ratios from two polynomials to relate the geometry between an image point (r, c) and the corresponding object point (X, Y, Z), as given in the following equation (Chen *et al.* 2006):

$$r = \frac{P_1(X,Y,Z)}{P_2(X,Y,Z)}, \qquad c = \frac{P_3(X,Y,Z)}{P_4(X,Y,Z)} \tag{1}$$

where r and c correspond to the row and column index of pixels in the image; X, Y, and Z refer to point coordinates in-ground space, correspondingly, while polynomials P_i (i = 1, 2, 3, 4) are determined as:

$$\begin{aligned} P_i = {} & a_{i,0} + a_{i,1}X + a_{i,2}Y + a_{i,3}Z + a_{i,4}XY + a_{i,5}XZ + a_{i,6}YZ \\ & + a_{i,7}X^2 + a_{i,8}Y^2 + a_{i,9}Z^2 + a_{i,10}XYZ + a_{i,11}X^3 + a_{i,12}XY^2 \\ & + a_{i,13}XZ^2 + a_{i,14}X^2Y + a_{i,15}X^3 + a_{i,16}YZ^2 + a_{i,17}X^2Z \\ & + a_{i,18}Y^2Z + a_{i,19}Z^3 \end{aligned} \tag{2}$$

Unknown RPCs may be achieved using the linearized RFM form (Long *et al.* 2015; Tengfei *et al.* 2014), as in the Equations 3 and 4:

$$P_1(X, Y, Z) - rP_2(X, Y, Z) = 0 \tag{3}$$

$$P_3(X, Y, Z) - cP_4(X, Y, Z) = 0 \tag{4}$$

To simplify the calculation, the coefficients a_0 of the denominator polynomials (P_2 and P_4) are set to 1. As a consequence, there are 78 unknown RPCs, which require at least 39 GCPs to solve using the ordinary least squares (OLS) method; the above equations can then be written as in the following equations (Jannati *et al.* 2017):

$$y = AX + e \tag{5}$$

$$x = (A^TA)^{-1}A^Ty \tag{6}$$

where A is the design matrix, y denotes the observations vector, e is the residuals vector, and x represents a vector of unknown RPCs.

There are two distinct computational situations applicable to RFM. If the physical sensor model is accessible, an approximate of the model can be supplied by the RFM, called a terrain-independent solution that can serve as a substitute sensor model. In contrast, a terrain-dependent method uses a set of GCPs to estimate the RFM's unknown parameters (RPCs) (Tao and Hu 2001; Valadan Zoej *et al.* 2007). This set of detection ground points is categorized into three categories: ground control points (GCP), dependent check points (DCP), and independent check points (ICP). The GCPs are used with OLS to estimate the RPCs values, while DCPs are exploited to calculate the cost value of the optimization process, and the ICPs are used to evaluate the accuracy of the whole method.

Methodology

Regardless of the mathematical function used, the geometric correction can be carried out with the following processing steps (Toutin 2004):

- Obtaining image(s) and preprocessing metadata
- Acquiring ground control points with image coordinates (r, c) and map coordinates (X, Y, Z)
- The determination of mathematical functions' unknown parameters for the geometric rectification model of one or more images
- Image(s) could be rectified with or without DEM

Figure 1 depicts different steps of our proposed method. The proposed method suggests that the orthorectification procedure using RFM be completely automated. As a result, there are two parts in the proposed method: the first part is called automated GCPs detection, which is dedicated to the identification and detection of GCPs automatically, and the second part is named RFM optimization, which is devoted to selecting the best GCPs set with an optimum combination of RPCs.

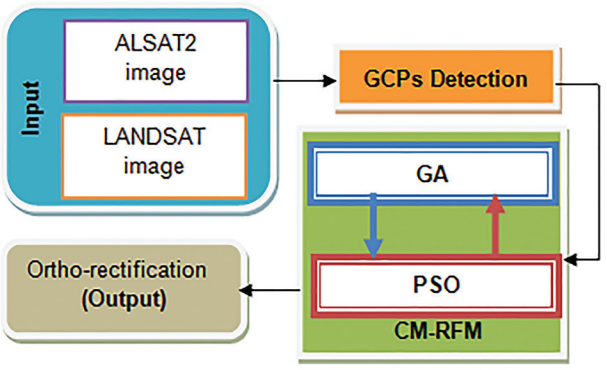

Figure 1. The flowchart steps of the suggested method.

The target images used in this paper are provided by the Algerian high-resolution satellite *ALSAT-2*, in which the images are taken over different cities. The first one was taken over Oran city (Algeria), while the second was over Djelfa city (Algeria). Compared to the first data set, which has an average elevation of 103 meters and a maximum elevation of 507 meters, the second data set is elevated with an average elevation of 650 meters and a maximum elevation of 2246 meters. Both data sets are in multispectral mode with a spatial resolution of 10 meters and a dimension of 1750 × 1750 pixels. Landsat images have a spatial resolution of 15 meters. They are used as reference images in this experiment study due they are the best-known high-resolution orthoimage reference databases available internationally (Konugurthi *et al.* 2016).

Automated GCPs Detection Steps

In this part of the method, there are five steps proposed for automated detection of GCPs: (band selection, contrast enhancement, Histogram Equalization, Gaussian Smoothening or filtration, and image matching).

(1) Band Selection

This section aims to extract the best band which has a high contrast to provide a maximum number of GCPs in the detection step; as a

result, we calculate the contrast ratio (CR) of each RGB band of the input images (*ALSAT-2* and Landsat) using the following formula (Peli 1990):

$$CR = \sqrt{\frac{1}{M \times N} \sum_{y=1}^{N} \sum_{x=1}^{M} \left(I(x\ y) - \beta \right)^2} \tag{7}$$

where x, y is the index pixel in the image I with M, N dimension, β defines the brightness:

$$\beta = \frac{1}{M \times N} \sum_{y=1}^{N} \sum_{x=1}^{M} \left(I(x,y) \right) \tag{8}$$

As shown in Figure 2, the average contrast ratio of red bands over all data sets (*ALSAT-2* and Landsat) provides a high contrast compared to other bands for the all data set evaluated; as a consequence the red band will be used in the next section.

The image histogram is a significant factor in any subjective image quality assessment, as illustrated in Figure 2, the histogram of the red bands still needs to be enhanced because does not have a great gray level distribution since most pixels are low gray level and do not cover the total gray level range. For this reason, prepossessing steps are applied to the red bands of the data sets with some techniques to enhance the pixel level distribution.

(2) Contrast Enhancement
Increasing the entropy and contrast in the image is crucial to enhance the probability of detecting points of interest (ground points). As a result, the Contrast Limited Adaptive Histogram Equalization (CLAHE) is applied to equalize and improve the contrast of the red band of *ALSAT-2* images. CLAHE is one of the image processing algorithms that is used for increasing image contrast; it is different from the conventional Adaptive Histogram Equalization in its contrast limiting, where it is based on tiles which is a small region in the image rather than enhancing the whole image. As a reason, it's ideal for increasing local contrast and enhancing edge definitions in different regions of an image (Boukerch *et al.* 2019; Pizer *et al.* 1990).

(3) Histogram Equalization
After CLAHE, we applied the Histogram Equalization to adjust the dynamic range and contrast on the entire image by modifying the intensity of the histogram. The intensity on the histogram can be better distributed with this algorithm and permits the areas with poor contrast to obtaining an increase in contrast (Boukerch *et al.* 2019).

Figure 3 represents the results of the application of CLAHE and Histogram Equalization, on the red bands of *ALSAT-2* and Landsat images. From the figure, we clearly observe, after the preprocessing steps are done as an initial enhancement of the red band images in each data set, an improvement in the histogram graph, which confirmed the great gray level distribution of the pixels that make the images ready to move for the next step of GCPs extraction.

(4) Gaussian Smoothening Filtration
Subsequent to the histogram equalized, the image was smoothed using a Gaussian smoothening filter of size 5 and sigma 1. This assists in the correction of non-uniform lighting (Indumathi and Sathananthavathi 2019). Figure 3 represents the results of the application of CLAHE, Histogram Equalization, and Gaussian Smoothening Filter on the red band of *ALSAT-2* and Landsat images. From the figure, we clearly observe, after the preprocessing steps are done as an initial enhancement of the red band images

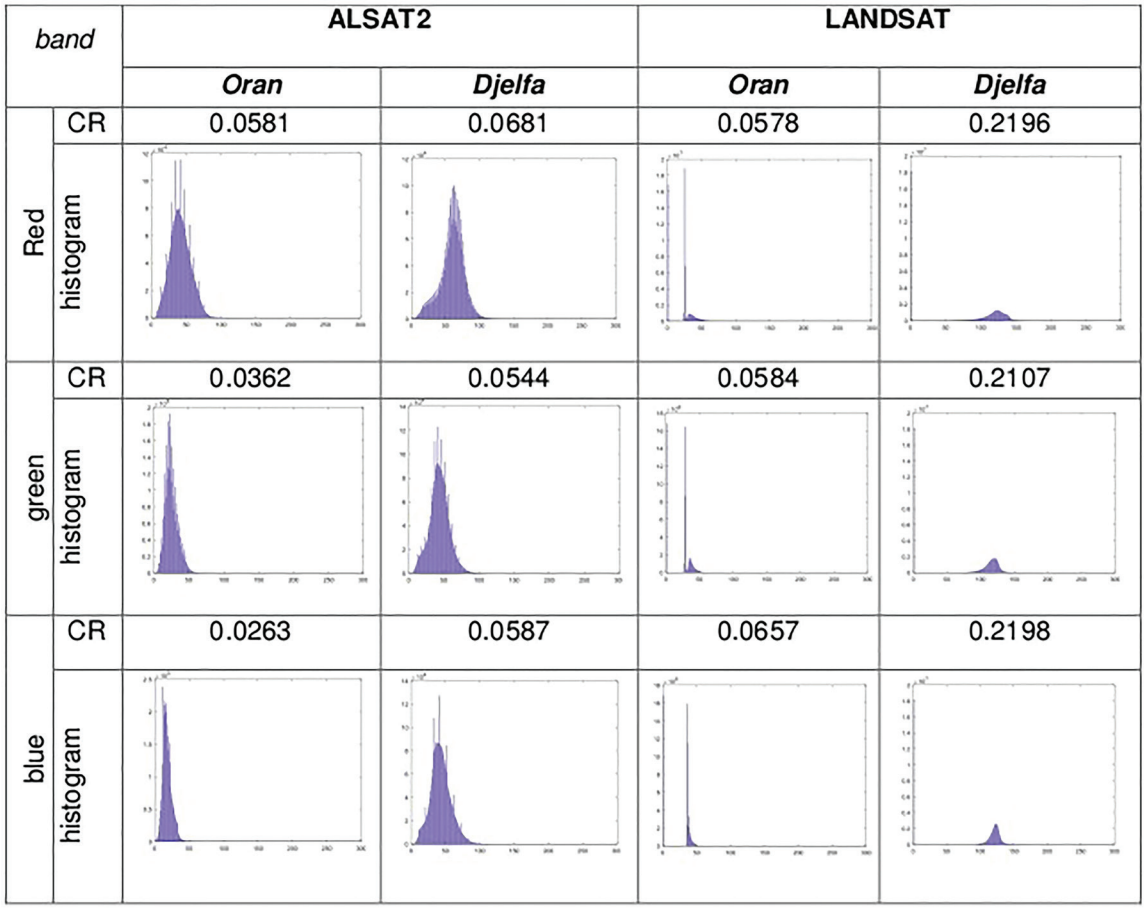

Figure 2. Histogram and contrast ratio of *ALSAT-2* image bands.

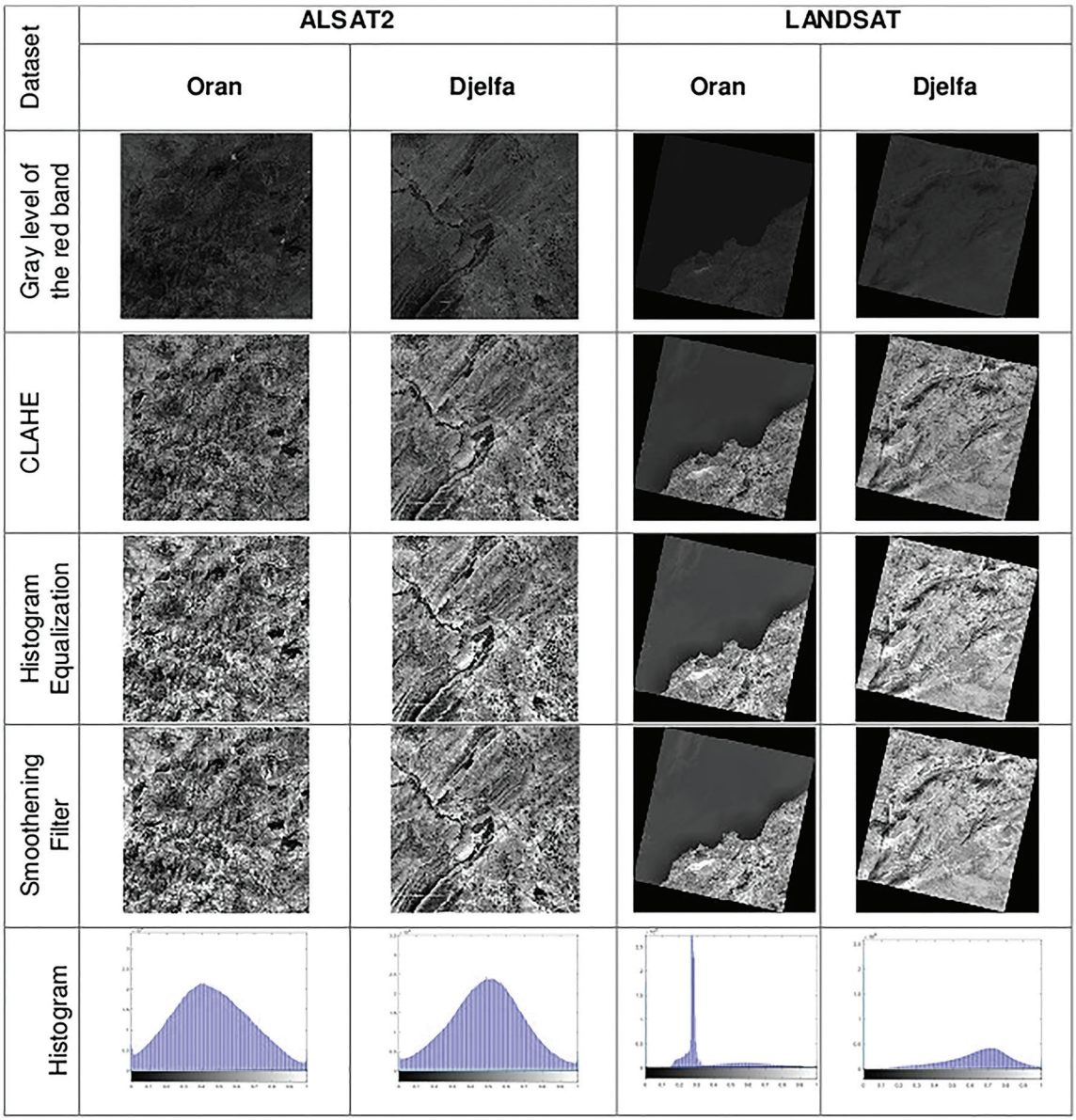

Figure 3. The histogram enhancement steps results.

in each data set, an improvement in the histogram graph, which confirmed the great gray level distribution of the pixels that make the images ready to move for the next step of GCPs extraction.

(5) Image Matching

This study is based on an image matching algorithm for the extraction and identification of GCPs, which are grouped into two groups, i.e., region-based matching and feature detector-descriptor methods. Compared to region-based methods, feature-based matching methods are theoretically more robust because they are invariant of scale and rotation and are thus less sensitive to noise and illumination variations (Indumathi and Sathananthavathi 2019). In regard, we use a feature-based matching method that combines two famous methods, Speeded Up Robust Features (SURF) and Scale-Invariant Feature Transform (SIFT), in which the SURF algorithm is used as a detector and SIFT as a descriptor. The authors in (Boukerch *et al.* 2019) have demonstrated that the combination of the two algorithms performs well than using each one separately for application on remote sensing images, especially with *ALSAT-2* images.

In this work, the databases of Landsat images are used as reference images with a spatial resolution of 15 meters. The *ALSAT-2* images with a spatial resolution of 10 meters in multispectral mode are considered target images. The brute-force technique is applied to match the extraction points from *ALSAT-2* images and reference images with the Lowe's ratio as in (Alhwarin *et al.* 2008; Bay *et al.* 2006) to determine the validated matches. Also, Random Sample Consensus (RANSAC) algorithm is used as second validation to reject and remove any other outliers, all the parameters of RANSAC in this paper are default settings using homography transformation model in Opencv. Finally, the corresponded elevation, longitude, and latitude of the extracted points from the reference image are determined using Shuttle Radar Topography Mission (SRTM) digital elevation model (DEM), which is obtained from the US Geological Survey's (USGS) official website (USGS EarthExplorer). In this way, the set of GCP is collected, where the coordinates' images (r, c) are taken from the target images (*ALSAT-2*), and the object coordinate (X, Y, Z) by matching the reference image with DEM. Figure 4 shows the result of these steps, also the number of the detected GCPs before and after the preprocessing steps .

The Proposed Optimization Algorithm CM-RFM

The most significant issue of optimization in RFM is determining the most efficient ground control points with the most appropriate RPCs, which makes the RFM optimization as multi-objective task. In this context, we may mention the research works in (Naeini *et al.* 2017;

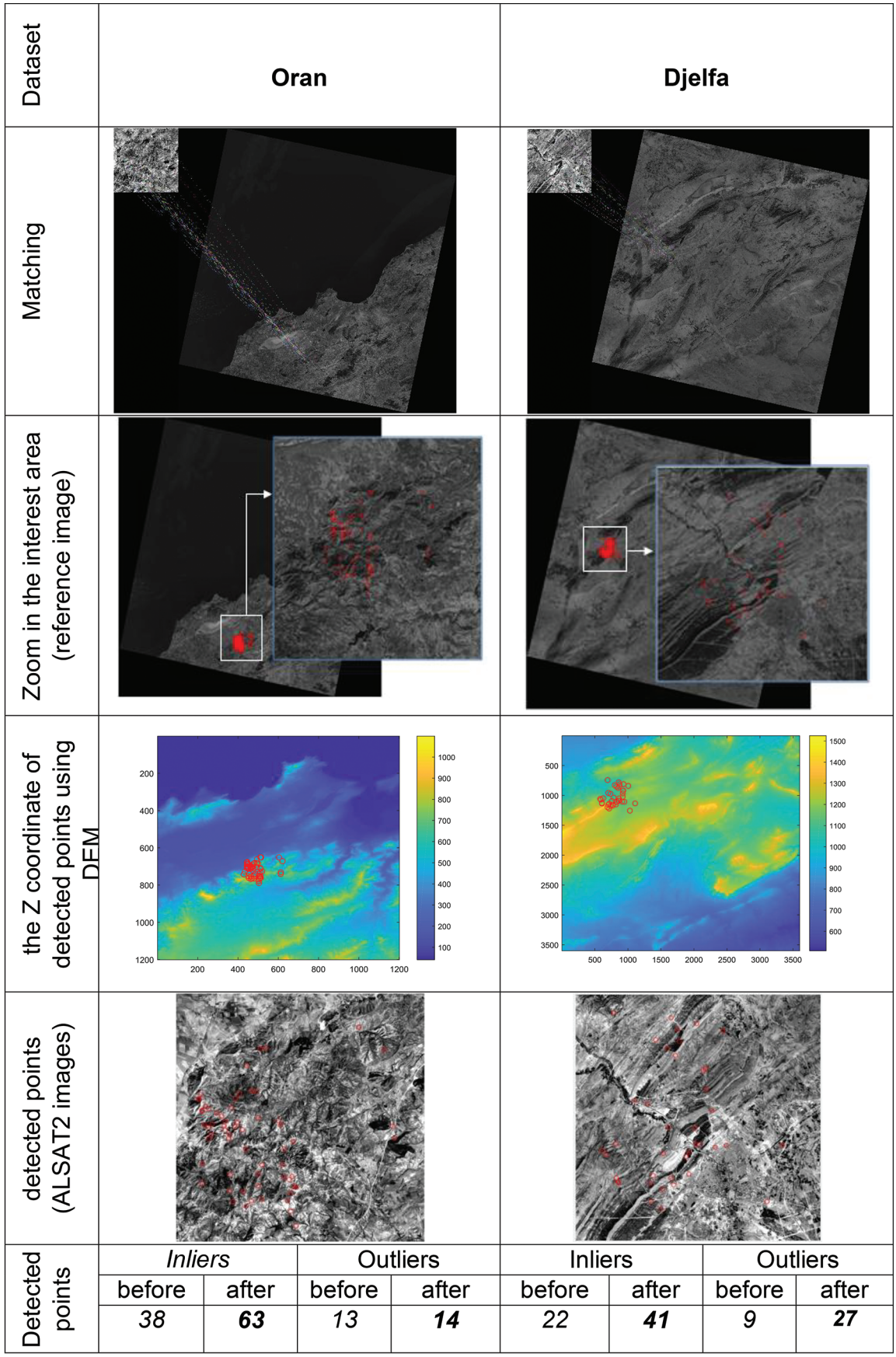

Detected points	*Inliers*		Outliers		Inliers		Outliers	
	before	after	before	after	before	after	before	after
	38	***63***	*13*	***14***	*22*	***41***	*9*	***27***

Figure 4. Extraction ground control points (GCPs) steps.

Gholinejad *et al.* 2019b) that used the multi-objective meta-heuristic algorithms for RFM optimization. However, the multi-objective algorithms suffer from some problems like the computational cost is significant because of the numerous optimization functions used, and also must have a relationship between these objectives' optimization functions, which makes it difficult to minimize/maximize both objective functions at the same time from a single location in the search space (Maghawry *et al.* 2021). For these reasons, this section describes a proposed cascaded meta-heuristic algorithm as a substitute for multi-objective algorithms to simultaneously determine and select the best GCPs with the optimum RPCs. Furthermore, this section gives the detailed procedure of the optimization algorithm.

(1) Structure of Individual

The suggested cascaded meta-heuristic algorithm combines GA with PSO with a modified selection mechanism based on the K-means clustering algorithm. To this end, the configuration of the chromosome/particle comprises two parts: a discrete part and a binary part. The first part is dedicated to GA initialized with discrete random values. Each value in a chromosome (called a gene) defines the index of the GCP and has a length equal to the number of GCPs set. The GCPs selected must be well-distributed; hence the K-means algorithm is applied to GCPs set identified in the previous step to obtain an optimum and well-distributed combination of GCPs. As a consequence, the number of genes in chromosomes is equal to K, where K is the number of clusters determined by the K-means algorithm applied to detected GCPs. The value of each gene is bounded between one and the maximum number of GCPs in each cluster, which means that the value of the first gene defines the index of GCP from the first cluster while the second defines the index of GCP from the second cluster and so on until the last gene which defines the index of GCP from the cluster "K".

The second part is reserved for PSO (the second stage), where the values in particles generated randomly with the values of 0 and 1 define the current position; it signifies that each particle is made up of a mix between one and zero, while the ones indicating the presence and zeros the absence of a corresponding coefficient in the RFM. The length of the particle equals 78, which is the number of coefficients in RFM (RPCs). This structure of chromosome/particle significantly decreased the research space because it divides into two (using two stages). A chromosome/particle sample used in the suggested algorithm is described in the following figure.

(2) GCPs/RPCs Optimization Procedure

The proposed cascaded meta-heuristic algorithm for RFM optimization, namely CM-RFM, is divided into two stages. In the first stage, the algorithm uses GA to search for the optimum set of GCPs, and in the second stage, the PSO is used to select the best combination of RPCs. At each iteration, the GA and PSO (two stages) communicate with each other to reach the best GCPs with the optimum combination of RPCs. Figure 6 illustrates the flowchart of the suggested model.

As is despite in Figure 6, the algorithm starts with the first stage (GA), in which a population of chromosomes is initialized with discrete random values; after the initialization, these chromosomes are combined with particles (binary part), which is steady in the first iteration all positions are equal one (all RPCs are present in the calculations), to calculate the fitness value (cost value) using a cost function determined by the root-mean-square error (RMSE) over the unselected points (DCPs). The formula of the cost function is given by:

$$\mathrm{RMSE} = \sqrt{\frac{\sum_{i=1}^{N}(x_i - \hat{x}_i)^2 + (y_i - \hat{y}_i)^2}{N}} \qquad (9)$$

where N is the number of DCPs , x_i, y_i are the estimate coordinate (x, y) value for the ith DCP point and $\hat{x}_i$,$\hat{y}_i$ are the actual coordinate (x, y) value for the ith DCP point.

Following that, the evolutionary mechanisms (selection, crossover, and mutation) are applied to the original chromosomes to generate offspring chromosomes; if the number of iterations is less than 40, the offspring chromosomes are clustered according to their cost value by the K-means algorithm (Kodinariya and Makwana 2013). The optimum value of "K" is chosen according to the elbow method from 2 and keeps increasing by 1 to the number of GCPs. Afterwards, one offspring chromosome is taken from each cluster, so there are "K" offspring chromosomes that get to the next stage ("K" sets of GCPs combination). We consider that the non-fit chromosomes may include good genes (good GCPs) that can guide the search process to a successful result; for that, we prefer to select different offspring for the next stage. If the iteration is more than 40, only the best offspring chromosome is picked, since generally the RFM optimization algorithm converges in less than 40 iterations (overall the population has the same value) (Mezouar *et al.* 2022).

In the next stage, the binary version of PSO is used to select the optimum combination of RPCs using the set of GCPs selected in the first stage. The fitness values of these particles are then determined and calculated with a set of GCPs selected by the GA (the best offspring chromosome); this manner of fitness calculation is applied if the number of iterations is more than 40, and if it is less than 40 iterations the whole population of PSO is divide into "K" subpopulation, where "K" is the number of clusters obtained by K-means algorithm in the first stage (the number of offspring get from the first stage). Each particle in the subpopulation of PSO is combined with the same chromosome (discrete part) from the K cluster, to calculate cost value, that mean all particles of the first subpopulation of PSO combined with the first chromosome (the first cluster) so on to the K subpopulation which combined with the chromosome K.

The best position of each particle (P_i) and the global best position of all particles (P_g) are then determined by the cost values, which are calculated using the two parts of the configuration chromosome/particle (GCPs + RPCs). While the fitness values of these particles are then determined using the same cost function of first stage (RMSE). Where at each iteration, the velocity of the particles is updated using the Equation 10, and it is bounded between a minimum and maximum velocity [vmin, vmax] (Eberhart and Shi 2001).

$$v_{ij}(t+1) = w(t).v_{ij}(t) + c_1.r_1(p_g(t) - x_{ij}(t) + c_2.r_2(p_i(t) - x_{ij}(t)) \qquad (10)$$

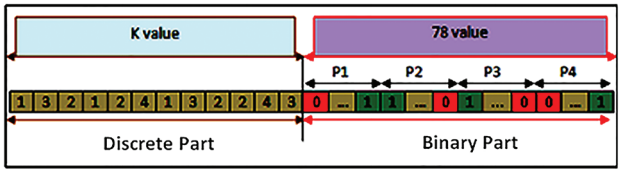

Figure 5. Chromosome/particle structure.

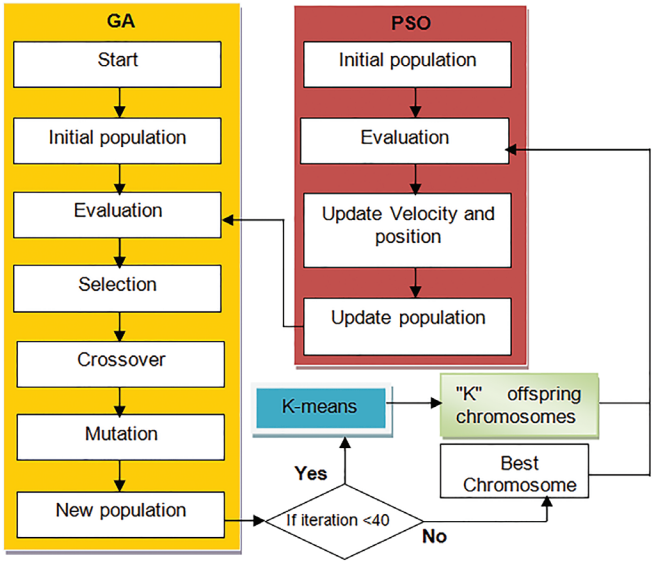

Figure 6. Flowchart of the CM-RFM algorithm.

where t is the number of iteration, i represent the index of particle, while j is the index of bit in each particle; r_1 and r_2 are two uniform random numbers in the interval [0,1]; c_1 and c_2 are two constant called acceleration coefficients, and $w(t)$ is the inertia weight. The particle position xi is updated in each iteration (t) using the following equations as in Yavari *et al.* (2013):

$$x_{ij}(t+1) = \begin{cases} 1, & \text{if} \quad r < \phi\left(v_{ij}(t+1)\right) \\ 0, & \text{otherwise} \end{cases} \tag{11}$$

$$\phi\left(v_{ij}(t+1)\right) = \begin{cases} \tanh\left(v_{ij}(t+1)\right), & \text{if} \quad v_{ij}(t+1) > 0 \\ 0, & \text{otherwise} \end{cases} \tag{12}$$

where tanh() is the hyperbolic tangent function. In the next iteration, the global best position is used in the first stage on the binary part of the individual to calculate the fitness function, not as the first iteration in which all RPCs are using in the calculation. This procedure is repeated until a stopping criterion is reached, which is the maximum iteration in this research (200 iterations). Table 1 lists the PSO and GA parameters used in this research.

Table 1. The parameters used in genetic algorithm (GA) and particle swarm optimization (PSO).

GA		PSO	
Population Size	80	Population Size	30
Selection Type	Roulette Wheel	V V_{max}	+3
		V V_{min}	–3
Crossover Type	Single point	W	0.7
Mutation Probability	0.001	C1	1.5
Crossover Probability	0.75	C2	1.5

Experiments Results and Discussion

To examine the quality of the results achieved by the suggested CM-RFM approach, a comparison was made with two competing literature methods, PSORFO (Yavari *et al.* 2013) and HPSO-RFM (Mezouar *et al.* 2021). In contrast to CM-RFM, which has a complete stage for automatic GCPs selection, these two approaches have focused only on finding the optimal RPCs while the GCPs are picked at random or by the user.

We used two data sets (Oran and Djelfa) with (10, 15, and 20) GCPs distribution chosen randomly for all the competing methods; where 15 well-distributed points are selected as ICPs to evaluate the algorithms. The unselected points from GCPs define the DCPs and are used to calculate the fitness function. The used ground points are detected automatically at the first step of the proposed orthorectification process. (see Figures 3 and 4). Two metrics are used to evaluate the quality of the results. The RMSE and standard deviation (STD) measured over RMSEs. The accuracy of the generated findings is determined by the RMSE computed over ICPs. The STD is an appropriate measure that evaluates the stability of the competing literature methods. To assess the efficiency of the algorithms in terms of stability and global accuracy, we calculate the average of the RMSEs from 10 runs because each execution of meta-heuristic algorithm produces a different result, noted Avg-RMSE (in pixels) in Table 2. The experiments have been implemented in MATLAB software using the software package "mexopencv". The obtained results for the two data sets showed that our suggested method outperform the other competing methods in terms of accuracy and stability in most cases.

Compared to PSORFO and HPSO-RFM, our suggested algorithm CM-RFM performs well because it has an additional stage dedicated to GCPs selection and uses the K-means as a selection operation. These steps give the algorithm a wider range of possible solutions, allowing the CM-RFM to determine the optimal combination of GCPs and the best RPCs for RFM simultaneously. On the other hand, PSORFO and HPSO-RFM neglected the selection of GCPs and devoted simply to optimizing the RPCs. The average of all RMSE scores shows that CM-RFM has improved the accuracy of HPSO-RFM by 33.69% and PSORFO by 73.76%. The results obtained from the second data set (Djelfa) demonstrate a reduction in the accuracy; this could be explained by the GCPs distribution over this data set, which is less than the first data set due to the landscape of this site, which is an elevated area compared to the first data set (Oran). The presences of mountains in this region (Djelfa) create the relief displacement error and introduce terrain distortions which affect the orthorectification accuracy.

In term of stability, which is presented in Table 2 (STD) in pixels, may reveal the most significant advantage of CM-RFM compared to PSORFO and HPSO-RFM, the proposed algorithm (CM-RFM) was more stable than the competing literature methods in all cases of the first data set, and almost cases of the second data set. As example, our algorithm achieved the best stability (STD) value which is only 1.0736 on the first data set while applying 15 GCPs.

Table 3 presents the optimum result (the best run with the lowest cost function of the 10 runs) of the proposed algorithm CM-RFM. The experiment results list the number of the best RPCs [P1, P2, P3, P4] founded at each combination of GCPs and the optimum RMSEs obtained over ICP. In simple terms and according to the study results, the CM-RFM algorithm has an acceptable accuracy for all GCPs distributions

Table 3. The optimum rational function model (RFM) achieved by CM-RFM.

Data Set	GCP/DCP/ICP	RMSE ICP (in Pixels)	Number of RPCs (P1, P2, P3, P4)
Oran	20/28/15	2.6969	4, 1, 4, 1
	15/33/15	2.5636	4, 0, 3, 0
	10/38/15	2.5042	3, 1, 4, 0
Djelfa	20/6/15	3.2264	4, 0, 5, 0
	15/11/15	3.1723	3, 0, 4, 0
	10/16/15	3.1716	4, 0, 4, 0

GCP = ground control points; DCP = dependent check points; ICP = independent check points; RMSE = root-mean-square error. RPC = Rational Polynomial Coefficients

Table 2. Result of the accuracy and the stability of CM-RFM, HPSO-RFM, and PSORFO.

		Avg-RMSE (in Pixel)			STD (in Pixel)		
Data Set	GCP/DCP/ICP	CM-RFM	HPSO-RFM	PSORFO	CM-RFM	HPSO-RFM	PSORFO
Oran	20/28/15	4.5812	5.8298	4.6920	1.7435	3.4204	2.4610
	15/33/15	4.0985	3.5845	3.5235	1.0736	2.6567	1.3811
	10/38/15	3.1328	3.4498	8.1749	0.3704	1.1779	11.0583
Djelfa	20/6/15	13.0621	32.2584	107.7184	8.1159	33.8128	113.0865
	15/11/15	11.2223	15.1181	12.6058	6.7545	11.8485	13.2123
	10/16/15	10.2253	9.6212	39.7970	7.2183	7.1700	36.0468

GCP = ground control points; DCP = dependent check points; ICP = independent check points; RMSE = root-mean-square error; STD = standard deviation.

with a minimum number of RPCs throughout the tested images. The RMSE over ICPs is equal to approximately 2 pixels for the first data set and about 3 pixels for the second data set.

The final optimal GCPs distributions with the optimum case (10 GCPs) for the two data sets are presented in Figure 7. For the Djelfa region, we notice a poor distribution of ground points over this image compared to the first data set (Oran), which had a higher number of GCPs detected in preprocessing steps. This is caused by the nature of the area covered that includes mountains with maximum elevation of 2246 meters as it is mentioned previously. That's why the accuracy of the second data set was slightly lower in this data set. In the overall analysis, the RMSE values show that the proposed algorithm's results are accurate sufficiently, even though it only uses a small number of GCPs (10 points).

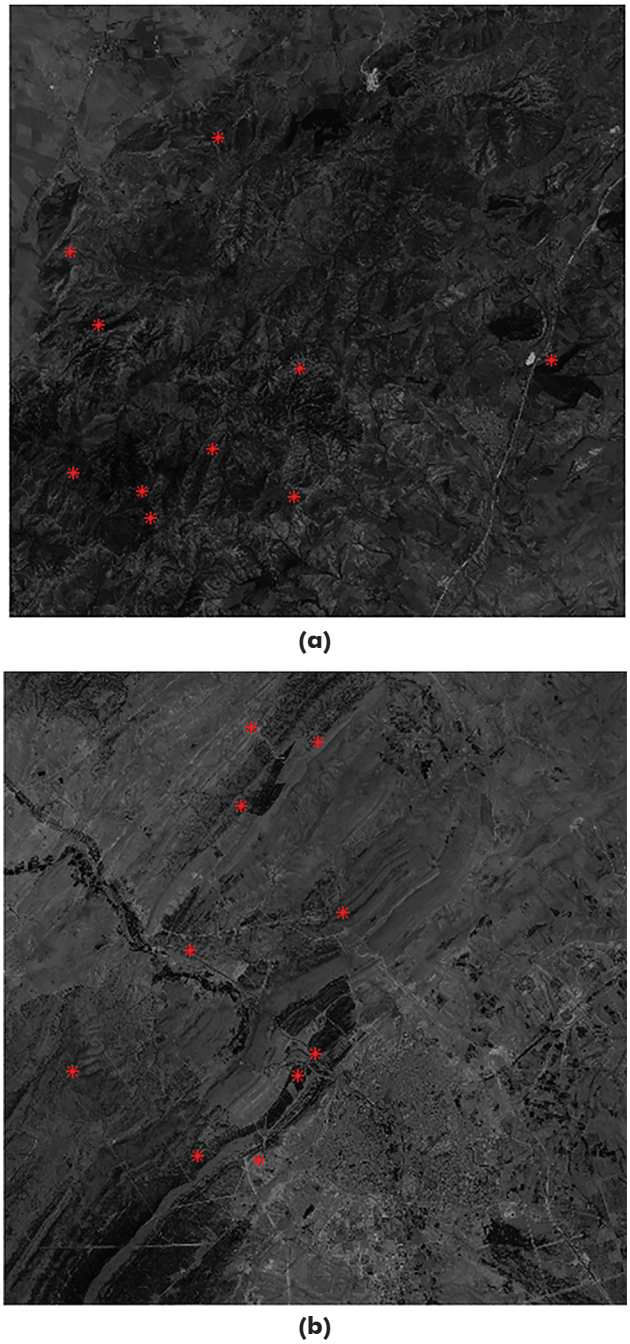

(a)

(b)

Figure 7. The final optimal ground control points (GCPs) distributions (10 points) with: (a) Oran, (b) Djelfa.

Conclusion

This paper presents the first completely automatic orthorectification chain based on a cascaded meta-heuristic algorithm and image matching method. The experimental results confirm the proposed method's reliability and high efficiency applied for *ALSAT-2* satellite images with different covered areas, while the number of GCPs extracted automatically is more than the conventional RFM need (more than 39 points). Furthermore, these detected points are optimized with an optimum combination of RPCs using the proposed CM-RFM algorithm, which achieved an acceptable accuracy and outperformed the competitive methods by accomplishing an improvement in accuracy that is approximately 73% better than PSORFO and 33% better than HPSO-RFM. The main advantage of CM-RFM is that it does not require any manual GCPs selection; additionally, it provides good performance and stability in the case of a few GCPs. The results show that the suggested method achieves satisfactory accuracy and stability while achieving optimal RFM with roughly three-pixel accuracy in the worst scenario.

Acknowledgments

The research being reported in this publication was supported by the Algerian Directorate General for Scientific Research and Technological Development (DGRSDT).

References

Alhwarin, F., C. Wang, D. Ristić-Durrant and A. Gräser. 2008. Improved SIFT-features matching for object recognition. Pages 179–190 in *Proceedings Visions of Computer Science-BCS International Academic Conference*. https://doi.org/10.14236/ewic/VOCS2008.16.

Bay, H., A. Ess, T. Tuytelaars and L. V. Gool. 2008. Surf: Speeded up robust features. *Computer Vision and Image Understanding* 110(3):346–359.

Bay, H., T. Tuytelaars and L. V. Gool. 2006. Surf: Speeded up robust features. *European Conference on Computer Vision.* Berlin, Heidelberg: Springer, 404–417.

Bentoutou, Y., N. Taleb, K. Kpalma and J. Ronsin. 2005. An automatic image registration for applications in remote sensing. *IEEE Transactions on Geoscience and Remote Sensing* 43(9):2127–2137. https://doi.org/10.1109/TGRS.2005.853187.

Boccardo, P., E. Borgogno Mondino, P. Claps and F. Perez. 2007. Image resolution effects for vegetation mapping from Landsat 7 ETM+ and Terra Modis data. *Water Resources Assessment under Water Scarcity Scenarios*:69–94.

Boukerch, I., B. Takarli, A. Boudaouie and A. Chaachoue. 2019. A framework for geometric quality evaluation and enhancement of Alsat-2A satellite imagery. *Sensors, Systems, and Next-Generation Satellites* XXIII(11151):501–508.

Chen, L. C., T. A. Teo and C. L. Liu. 2006. The geometrical comparisons of RSM and RFM for FORMOSAT-2 satellite images. *Photogrammetric Engineering & Remote Sensing* 72(5):573–579. https://doi.org/10.14358/PERS.72.5.573.

Eberhart and Shi Y. 2001. Particle swarm optimization: Developments, applications and resources. Pages 81–86 in *Proceedings of the 2001 Congress on Evolutionary Computation*, held in Seoul, South Korea, 27–30 May 2001.

Fraser, C. S. and H. B. Hanley. 2003. Bias compensation in rational functions for IKONOS satellite imagery. *Photogrammetric Engineering & Remote Sensing* 69(1):53–57. https://doi.org/10.14358/PERS.69.1.53.

Gholinejad, S., A. A. Naeini and A. Amiri-Simkooei. 2019a. Robust particle swarm optimization of RFMs for high-resolution satellite images based on K-fold cross-validation. *IEEE Journal of Selected Topics in Applied Earth Observations and Remote Sensing* 12(8):2594–2599. https://doi.org/10.1109/JSTARS.2018.2881382.

Gholinejad, S., A. A. Naeini and A. Amiri-Simkooei. 2019b. Handling ill-posedness and overparameterization of rational function model using bi-objective particle swarm optimization. *Earth Observation and Geomatics Engineering* 3(1):34–42. https://doi.org/10.22059/EOGE.2019.282476.1049.

Hu, Y., V. Tao and A. Croitoru. 2004. Understanding the rational function model: Methods and applications. *International Archives of Photogrammetry and Remote Sensing* 20(6):119–124.

Huo, C., C. Pan, L. Huo and Z. Zhou. 2011. Multilevel SIFT matching for large-size VHR image registration. *IEEE Geoscience and Remote Sensing Letters* 9(2):171–175.

Indumathi, G. and V. Sathananthavathi. 2019. Microaneurysms detection for early diagnosis of diabetic retinopathy using shape and steerable Gaussian features. In *Telemedicine Technologies*, 57–69. Cambridge, Mass.: Academic Press.

Jannati, M. and M. J. Valadan Zoej. 2015. Introducing genetic modification concept to optimize rational function models (RFMs) for georeferencing of satellite imagery. *GIScience & Remote Sensing* 52(4):510–525. https://doi.org/10.1080/15481603.2015.1052634.

Jannati, M., M. J. Valadan Zoej and M. Mokhtarzade. 2017. A knowledge-based search strategy for optimally structuring the terrain dependent rational function models. *Remote Sensing* 9(4):345. https://doi.org/10.3390/rs9040345.

Kartal, H., U. Alganci and E. Sertel. 2018. Automated orthorectification of VHR satellite images by SIFT-based RPC refinement. *ISPRS International Journal of Geo-Information* 7(6):229. https://doi.org/10.3390/ijgi7060229.

Kodinariya, T. and P. R. Makwana. 2013. Review on determining number of cluster in K-means clustering. *International Journal of Advance Research in Computer Science and Management Science* 1(6):90–95.

Konugurthi, P. K., R. Kune, R. Nooka and V. Sarma. 2016. Autonomous ortho-rectification of very high resolution imagery using SIFT and genetic algorithm. *Photogrammetric Engineering & Remote Sensing* 82(5):377–88. https://doi.org/10.1016/S0099-1112(16)82020-0.

Long, T., W. Jiao and G. He. 2015. RPC estimation via l1-norm-regularized least squares (L1LS). *IEEE Transactions on Geoscience and Remote Sensing* 53(8):4554–4567. https://doi.org/10.1109/TGRS.2015.2401602.

Maghawry, A., R. Hodhod, Y. Omar and M. Kholief. 2021. An approach for optimizing multi-objective problems using hybrid genetic algorithms. *Soft Computing* 25(1):389–405. https://doi.org/10.1007/s00500-020-05149-3.

Mezouar, O., F. Meskine and I. Boukerch. 2022. Rational function model optimization based on swarm intelligence metaheuristic algorithms. In *Artificial Intelligence and Its Applications*, *Lecture Notes in Networks and Systems*, edited by B. Lejdel, E. Clementini and L. Alarabi, 86–99. Cham: Springer International Publishing. https://doi.org/10.1007/978-3-030-96311-8_9.

Mezouar, O., F. Meskine, I. Boukerch and N. Taleb. 2021. A hybrid particle swarm optimization of the rational function model for satellite strip images ortho-rectification. *International Journal of Remote Sensing* 42(21):8056–8076. https://doi.org/10.1080/01431161.2021.1970270.

Misra, I., S. Manthira Moorthi, D. Dhar and R. Ramakrishnan. 2012. An automatic satellite image registration technique based on Harris corner detection and Random Sample Consensus (RANSAC) outlier rejection model. Pages 68–73 in *Proceedings 1st International Conference on Recent Advances in Information Technology (RAIT)*, held in Dhanbad, India. https://doi.org/10.1109/RAIT.2012.6194482.

Naeini, A. A., S. H. A. Moghaddam, S. M. J. Mirzadeh, S. Homayouni and S. B. Fatemi. 2017. Multiobjective genetic optimization of terrain-independent RFMs for VHSR satellite images. *IEEE Geoscience and Remote Sensing Letters* 14(8):1368–1372. https://doi.org/10.1109/LGRS.2017.2712810.

Nguyen, T. 2015. Optimal ground control points for geometric correction using genetic algorithm with global accuracy. *European Journal of Remote Sensing* 48(1):101–120. https://doi.org/10.5721/EuJRS20154807.

Pan, H., C. Tao and Z. Zou. 2016. Precise georeferencing using the rigorous sensor model and rational function model for ZiYuan-3 strip scenes with minimum control. *ISPRS Journal of Photogrammetry and Remote Sensing* 119:259–266. https://doi.org/10.1016/j.isprsjprs.2016.06.005.

Peli, E. 1990. Contrast in complex images. *Journal of the Optical Society of America A* 7(10):2032.

Pizer, S. M., R. E. Johnston, J. P. Ericksen, B. C. Yankaskas and K. E. Muller. 1990. Contrast-limited adaptive histogram equalization: Speed and effectiveness. Pages 337–345 in *Proceedings of the First Conference on Visualization in Biomedical Computing*, held in Atlanta, GA. https://doi.org/10.1109/VBC.1990.109340.

Tao, C. V. and Y. Hu. 2001. A comprehensive study of the rational function model for photogrammetric processing. *Photogrammetric Engineering and Remote Sensing* 67(12):1347–1358.

Teke, M. and A. Temizel. 2010. Multi-spectral satellite image registration using scale-restricted SURF. Pages 2310–2313 in *Proceedings 20th International Conference on Pattern Recognition*, held in Istanbul, Turkey. https://doi.org/10.1109/ICPR.2010.565.

Tengfei, L., J. Weili and H. Guojin. 2014. Nested regression based optimal selection (NRBOS) of rational polynomial coefficients. *Photogrammetric Engineering & Remote Sensing* 80(3):261–269. https://doi.org/10.14358/PERS.80.3.261.

Toutin, T. 2004. Review article: Geometric processing of remote sensing images: Models, algorithms and methods. *International Journal of Remote Sensing* 25(10):1893–1924.

Valadan Zoej, M. J., M. Mokhtarzade, A. Mansourian, H. Ebadi and S. Sadeghian. 2007. Rational function optimization using genetic algorithms. *International Journal of Applied Earth Observation and Geoinformation* 9(4):403–413. https://doi.org/10.1016/j.jag.2007.02.002.

Wang, R., Y. Shi and W. Cao. 2019. GA-SURF: A new speeded-up robust feature extraction algorithm for multispectral images based on geometric algebra. *Pattern Recognition Letters* 127:11–17.

Xiong, Z. and Y. Zhang. 2010. Bundle adjustment with rational polynomial camera models based on generic method. *IEEE Transactions on Geoscience and Remote Sensing* 49(1):190–202. https://doi.org/10.1109/TGRS.2010.2054833.

Yavari, S., M. J. V. Zoej, M. Mokhtarzade and A. Mohammadzadeh. 2012. Comparison of particle swarm optimization and genetic algorithm in rational function model optimization. *ISPRS—International Archives of the Photogrammetry, Remote Sensing and Spatial Information Sciences* 39B1:281–284.

Yavari, S., M. J. Valadan Zoej, A. Mohammadzadeh and M. Mokhtarzade. 2013. Particle swarm optimization of RFM for georeferencing of satellite images. *IEEE Geoscience and Remote Sensing Letters* 10(1):135–139. https://doi.org/10.1109/LGRS.2012.2195153.

Ye, F., Y. Su, H. Xiao, X. Zhao and W. Min. 2018. Remote sensing image registration using convolutional neural network features. *IEEE Geoscience and Remote Sensing Letters* 15(2):232–236. https://doi.org/10.1109/LGRS.2017.2781741.

In-Press

Zhikang Lin, Wei Liu, Yulong Wang, Yan Xu, Chaoyang Niu. Change Detection in SAR Images through Clustering Fusion Algorithm and Deep Neural Networks.

Hongbin Luo, Wanqiu Zhang, Cairong Yue, and Si Chen. Strategies for Forest Height Estimation by High-Precision DEM Combined with Short-Wavelength PolInSAR TanDEM-X.

Yunping Chen, Yue Yang, Lei Hou, Kangzhuo Yang, Jiaxiang Yu, and Yuan Sun. High-Resolution Aerosol Optical Depth Retrieval in Urban Areas Based on Sentinel-2.

Xiaoguang Ruan, Fanghao Yang, Meijing Guo, and Chao Zou. 3D Scene Modeling Method and Feasibility Analysis of River Water-Land Integration.

Jinlong Chen, Yueming Sun, Xiao Huang, Hongsheng Zhang. Multi-level Perceptual Network for Urban Building Extraction from High-Resolution Remote Sensing Images.

Linfeng Wu, Huajun Wang, and Huiqing Wang. A Lightweight Conditional Convolutional Neural Network for Hyperspectral Image Classification.

Elaina Gonsoroski, Yoonjung Ahn, Emily W. Harville, Nathaniel Countess, Maureen Y. Lichtveld, Ke Pan, Leslie Beitsch, Samendra P. Sherchan, and Christopher K. Uejio. Classifying Building Roof Damage Using High Resolution Imagery for Disaster Recovery.

WHO'S WHO IN ASPRS

Founded in 1934, the American Society for Photogrammetry and Remote Sensing (ASPRS) is a scientific association serving thousands of professional members around the world. Our mission is to advance knowledge and improve understanding of mapping sciences to promote the responsible applications of photogrammetry, remote sensing, geographic information systems (GIS) and supporting technologies.

BOARD OF DIRECTORS

BOARD OFFICERS

President
Lorraine B. Amenda, PLS, CP
Towill, Inc

President-Elect
Bandana Kar
Oak Ridge National Lab

Vice President
Amr Abd-Elrahman
University of Florida

Past President
Christopher Parrish, Ph.D
Oregon State University

Treasurer
John McCombs
NOAA

Secretary
Harold Rempel
ESP Associates, Inc.

COUNCIL OFFICERS

ASPRS has six councils. To learn more, visit https://www.asprs.org/Councils.html.

Sustaining Members Council
Chair: Ryan Bowe
Deputy Chair: Melissa Martin

Technical Division Directors Council
Chair: Hope Morgan
Deputy Chair:

Standing Committee Chairs Council
Chair:
Deputy Chair:

Early-Career Professionals Council
Chair: Youssef Kaddoura
Deputy Chair:

Region Officers Council
Chair: Demetrio Zourarakis
Deputy Chair: Jason Krueger

Student Advisory Council
Chair: Oscar Duran
Deputy Chair:

TECHNICAL DIVISION OFFICERS

ASPRS has seven professional divisions. To learn more, visit https://www.asprs.org/Divisions.html.

Geographic Information Systems Division
Director: Denise Theunissen
Assistant Director: Jin Lee

Lidar Division
Director: Ajit Sampath
Assistant Director: Mat Bethel

Photogrammetric Applications Division
Director: Ben Wilkinson
Assistant Director: Hank Theiss

Primary Data Acquisition Division
Director: Srini Dharmapuri
Assistant Director: Ravi Soneja

Professional Practice Division
Director: Hope Morgan
Assistant Director: Matt Elious

Remote Sensing Applications Division
Director: Tao Liu
Assistant Director: Indu Jeyachandran

Unmanned Autonomous Systems (UAS)
Director: Jacob Lopez
Assistant Director: Bahram Salehi

REGION PRESIDENTS

ASPRS has 13 regions to serve the United States. To learn more, visit https://www.asprs.org/regions.html.

Alaska Region

Cascadia Region
Jimmy Schulz

Eastern Great Lakes Region
Craig Fry

Florida Region
Matt LaLuzerne

Gulf South
Cody Condron

Heartland Region
Whit Lynn

Mid-South Region
David Hughes

North Atlantic Region
Kurt Lutz

Northeast Region

Pacific Southwest Region
Omar Mora

Potomac Region
Jason Brown

Rocky Mountain Region
Trent Casi

Western Great Lakes Region
Adam Smith

UAS-Based Multi-Temporal Rice Plant Height Change Prediction

Yuanyang Lin, Jing He, Gang Liu, Biao Mou, Bing Wang, and Rao Fu

Abstract

Analyzing rice growth is essential for examining pests, illnesses, lodging, and yield. To create a Digital Surface Model (DSM) of three important rice breeding stages, an efficient and fast (compared to manual monitoring) Unoccupied Aerial System was used to collect data. Outliers emerge in DSM as a result of the influence of environment and equipment, and the outliers related to rice not only affect the extraction of rice growth changes but are also more challenging to remove. Therefore, after using ground control points uniform geodetic level for filtering, statistical outlier removal (SOR) and quadratic surface filtering (QSF) are used. After that, differential operations are applied to the DSM to create a differential digital surface model that can account for the change in rice plant height. Comparing the prediction accuracy before and after filtering: R^2 = 0.72, RMSE = 5.13cm, nRMSE = 10.65% for the initial point cloud; after QSF, R^2 = 0.89, RMSE = 2.51cm, nRMSE = 5.21%; after SOR, R^2 = 0.92, RMSE = 3.32cm, nRMSE = 6.89%. The findings demonstrate that point cloud filtering, particularly SOR, can increase the accuracy of rice monitoring. The method is effective for monitoring, and after filtering, the accuracy is sufficiently increased to satisfy the needs of growth analysis. This has some potential for application and extension.

Introduction

With two-thirds of China's urban and rural residents relying on rice as their food ration, ensuring food security is of importance to people's lives. Even more difficulties for food production are posed by deteriorating quality of arable land, water scarcity, and climate change. In order to preserve our food security and maintain the ecological balance between humans and nature, prompt and accurate access to the size of rice production is necessary (Yu *et al.* 2016). A crucial component of precision agriculture is quick and precise access to information about crop development, which aids in crop management decisions, risk assessment, and also makes up for the manpower shortage (Guo *et al.* 2015; Gil-Docampo *et al.* 2020; Tang *et al.* 2020). Due to the need for crop growth surveys to collect data on rice growth, field monitoring of the crop during the growing season is essential. Traditional manual crop growth monitoring techniques, such as measuring crop height with a steel ruler or gathering data on crop development with various handheld tools, could endanger the crop. Additionally, the workload is heavy and ineffective, and varying measuring requirements among different measurers may have an impact on accuracy and decrease productivity (Li *et al.* 2015; Jimenez-Berni *et al.* 2018). It can greatly raise the cost, particularly when crops are cultivated over large regions or monitored in places that are difficult to access (Chang *et al.* 2011). Rice growth can only be predicted on a large scale at the national, provincial, and county levels due to low resolution and cloud cover occlusion in satellite imaging. This is especially true for hilly areas in southern China where the accuracy of satellite imaging is insufficient for monitoring changes in rice growth height (Matese *et al.* 2015; Cen *et al.* 2019). Although ground-based systems (like lidar) can quickly capture dense point clouds with high accuracy for target features, the cost of three-dimensional (3D) laser scanners restricts precision agricultural research and production. Unoccupied aerial vehicle platforms and sensor prices have dramatically dropped over the past few years, making it possible to obtain remote sensing data with improved spatial and temporal resolution (Candiago *et al.* 2015; Burkart *et al.* 2018). Unoccupied Aerial System (UAS) are more versatile, easier to use, and have higher spatial resolution than satellites for crop monitoring. They can produce high-resolution data products and gather a variety of information about crops, making it simple for farmers to keep an eye on and manage their crops (Rasmussen *et al.* 2016; Zhou *et al.* 2017).

Among the many phenotypic traits derived from UAS, crop height is a key predictor of crop evapotranspiration, yield, biomass, and health as well as its resilience to pests and overturning (Olson and Anderson 2021). Crop height can be extracted using products made from high-resolution photos captured by UAS. Matese *et al.* (2017) collected vineyard photos with a UAS equipped with a high-resolution digital camera and created digital terrain model (DTM) to determine the height of the grape plants. Ziliani *et al.* (2018) used a fixed-wing UAS to capture Red-Green-Blue photos of crops and create a Digital Surface Model (DSM) to determine crop canopy height, while Bendig *et al.* (2014) used multi-temporal Crop Surface Models (CSMs) to extract barley plant height. However, due to weather conditions and system equipment errors, computer-generated point clouds can have non-geomorphic anomalous point clouds, also called outlier point clouds. Outlier point clouds are classified into three categories: isolated outliers, isolated and clustered outliers, and randomly distributed outliers close to the objects and/or ground (Zeybek 2021b). Outlier point clouds, particularly the third one, can influence crop height extraction accuracy, but manual extraction and removal of outlier clouds based on experience are time-consuming and expensive, so automatic identification and removal of outlier points can extract plant height more quickly and accurately. The point clouds were filtered by Zeybek and Şanlıoğlu (2019) using four filtering algorithms, and the results demonstrate that these semi-automatic filtering procedures achieved a desirable accuracy in comparison to the operator accessibility of complex area filtering and time reduction with automation.

This study used a consumer-grade UAS to gather remote sensing data on rice in Qingbaijiang, Sichuan, China, during crucial developmental stages in order to construct high-precision digital orthophoto maps (DOM) and DSM (Lear 1997). Fewer studies have examined the removal of outlier point clouds from feature surfaces, despite the fact that numerous studies have concentrated on crop height extraction. In this study, the ground control points (GCP) is used to geographically align the images of each phase to ensure that all data are on the same geoid. Statistical outlier removal (SOR) and quadratic surface filtering (QSF) filtering were used to remove the outlier point clouds, and finally the extraction accuracy of rice plant height change values before and after

Yuanyang Lin, Jing He, Biao Mou, Bing Wang, and Rao Fu are with the School of Earth Sciences, Chengdu University of Technology, Chengdu 610059, China (xiao00yao@163.com).

Gang Liu is with the School of Earth Sciences, Chengdu University of Technology, State Key Laboratory of Geological Hazard Prevention and Geological Environment Protection, Chengdu 610059, China.

Contributed by Filiz Sunar, August 10, 2022 (sent for review August 26, 2022; reviewed by Michael J. Campbell, Mustafa Zeybek, Mustafa Zeybek).

Photogrammetric Engineering & Remote Sensing
Vol. 89, No. 5, May 2023, pp. 301–310.
0099-1112/22/301–310
© 2023 American Society for Photogrammetry and Remote Sensing
doi: 10.14358/PERS.22-00107R2

the point cloud filtering was compared. The focus of this study is to achieve spatial coordinate unification, investigate the effect of removing outlier points on rice height extraction, improve the accuracy of plant height extraction, and provide a high precision and low-cost agricultural monitoring technology for dynamic monitoring of plant growth.

Materials and Methods

Data Sources

The study area, which covers around 28 acres, is situated in Yao Du Town, Qing Baijiang, Chengdu City, Sichuan Province. It is situated in northeastern Chengdu City (103°18'–104°20'E, 30°47'–30°49'N), in the shallow slopes of the Longquan Mountain Range, at a height of roughly 480 m, and enjoys a humid subtropical climate.

Rice is the main crop farmed in the research area, and there are two different planting techniques: automated transplanting (Figure 1) and hand planting. Regions A, B, and C were chosen as the three study areas where rice plant height would be manually measured. One–year-old rice was planted in a mechanized way in areas A and B, whereas artificially planted one–year-old rice was in area C. The research area's location and regional dispersion are depicted in Figure 2.

The high-definition images were acquired at four critical periods of rice growth: the tillering stage (22 June 2021), the long spike stage (3 July 2021), the fruiting stage (13 August 2021), and the maturity stage (28 September 2021), respectively. As a large number of weeds were growing in the rice fields during the tillering period, farmers were mechanically spraying pesticides for weed control. The experiments were conducted using a PHANTOM 4 PRO UAS equipped with a position and orientation system (POS) to collect image data. The UAS had a takeoff weight of 1388 g, an image size of 5472 × 3648, a lens of FOV 84° 8.8 mm/24 mm, and a maximum flight time of 30 minutes.

The flyer must examine the topography, climate, and weather in the study area before beginning flying operations, as well as the connections between the flight equipment. The pre-trip preparation process was a crucial step in ensuring the accuracy of the data collected. Particularly, the research area was carefully inspected and scouted for buildings, trees, etc. that would act as high barriers. Areas that would act as barriers were avoided when constructing the path. Because the volatility of the solar zenith angle is small, image acquisition is done when the sunlight intensity is consistent and the sky is clear and

Figure 1. Transplanting rice seedlings by rice transplanter.

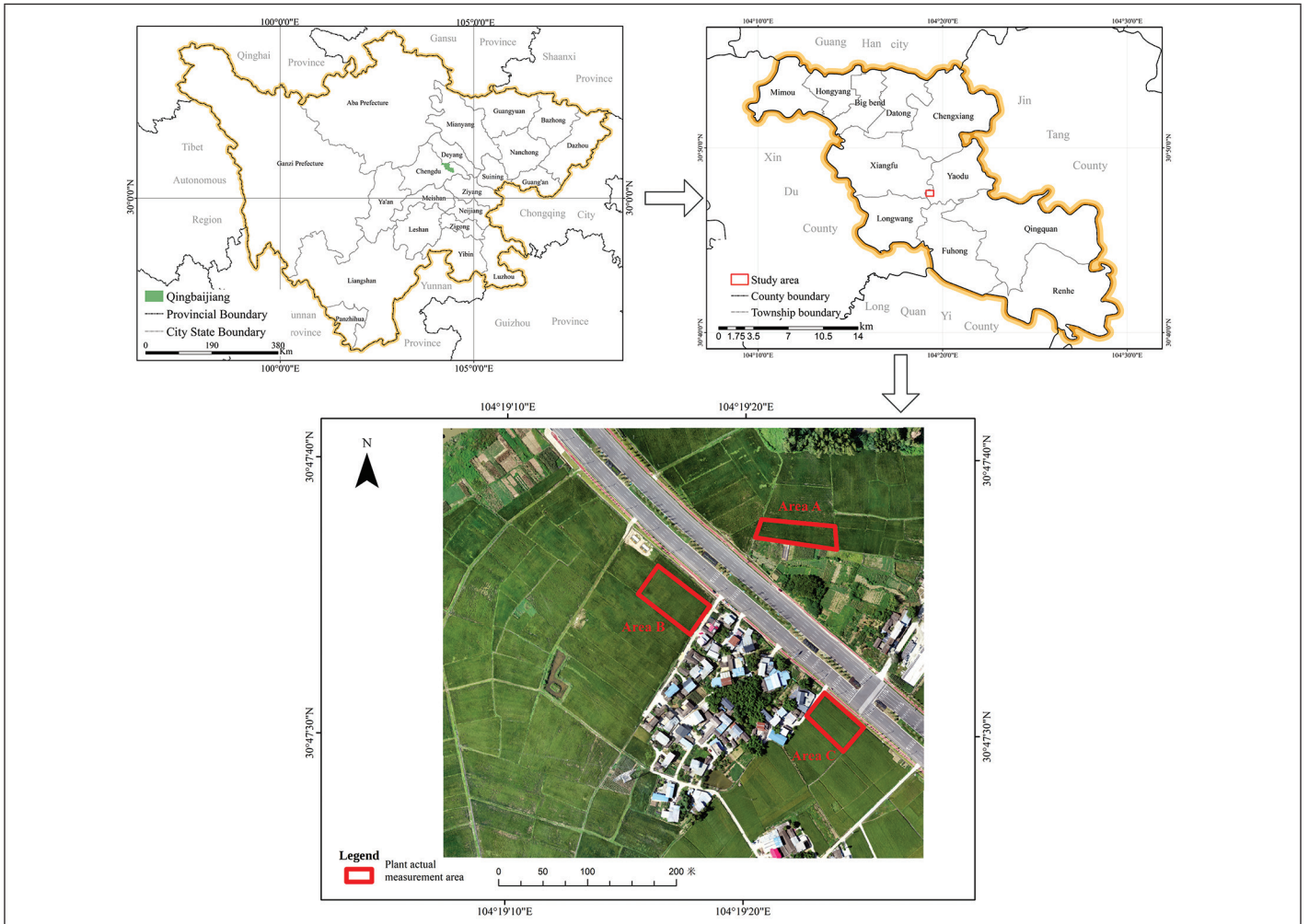

Figure 2. Location and regional distribution of the study area.

cloudless (Wang *et al.* 2021). Data collection took place between 11:00 and 14:00 local time, at a flight altitude of 100 meters, with a heading overlap of 80% and a side overlap of 70%. Each data collection produced about 800 photos.

The plant heights H of the three critical periods of rice growth were collected under windless conditions after the unoccupied aerial vehicle flights at the rice tillering stage (22 June 2021), the long spike stage (3 July 2021), and the fruiting stage (13 August 2021), respectively: the height of the rice plant was measured using a tape measure, using the height from the planting ground to the top leaves as the reference (Yue *et al.* 2018). In each of A, B, and C, twelve 1 m × 1 m sampling spots were randomly chosen (Figure 3). Five rice plants were gathered from the center of each sampling point, and the average value was used to determine the rice plants' measured height in that location. A total of 180 rice plants were measured in the three areas for each data collection.

In order to calibrate the spatial coordinates of the UAS aerial survey using GCP (Zeybek 2021a), 30 ground control points were laid out uniformly in the study area using STONEX s9 II RTK with the National Geodetic 2000 coordinate system as a reference. In this study, Global Navigation Satellite System differential positioning is performed using the Qianxun SI FindCM: a centimeter-level differential data broadcasting service based on RTK technology, where the terminal device receives the differential data and then decodes its own satellite observation data for positioning accuracy.

Data Processing

Pix4Dmapper (Pix4D Inc., San Francisco, CA, USA) is used to process UAS remote sensing photos. It uses structure from motion (SfM) and multi-view 3D reconstruction approaches to optimize camera settings and produce high-resolution DSM and DOM. Through iterative bundle adjustment techniques, SfM automatically resolves information such as camera orientation and scene geometry. Additionally, it uses nonlinear least squares techniques for continuous optimization and automatic feature matching (Lowe 2004; Snavely *et al.* 2008; Chang *et al.* 2017). However, the 3D point cloud data only has an image-space coordinate system, so it must be transformed into a real-world space coordinate system. GCP can increase absolute positioning accuracy, reduce radial and tangential distortion by optimizing calibration settings, and change picture coordinates to a reference coordinate system (Westoby *et al.* 2012; Mesas-Carrascosa *et al.* 2015). In this study, the DSM is rebuilt using structure from motion, and the point cloud is rebuilt using the "dense" feature density. Figure 4 depicts the specific flow of data processing.

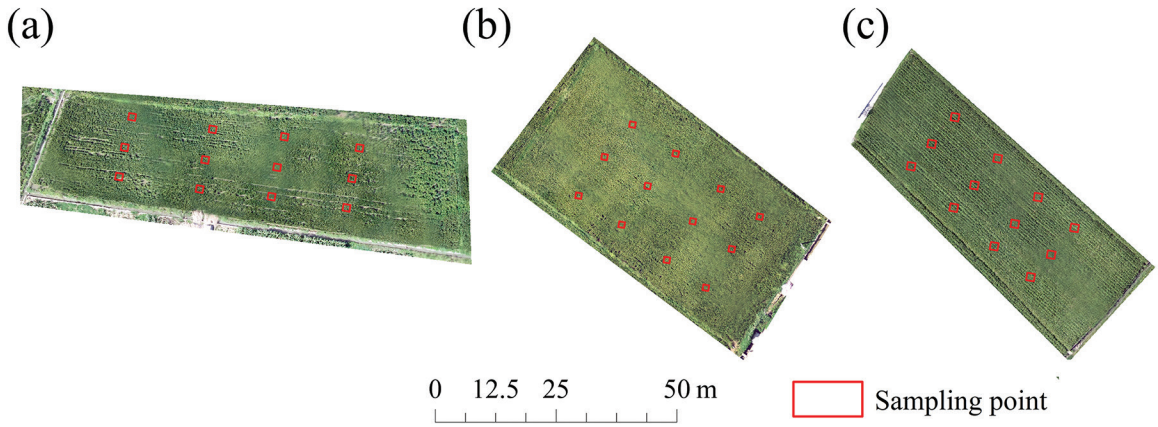

Figure 3. Ground-truthing plant height sampling points. (a) Area A sampling point, (b) Area B sampling point, (c) Area C sampling point.

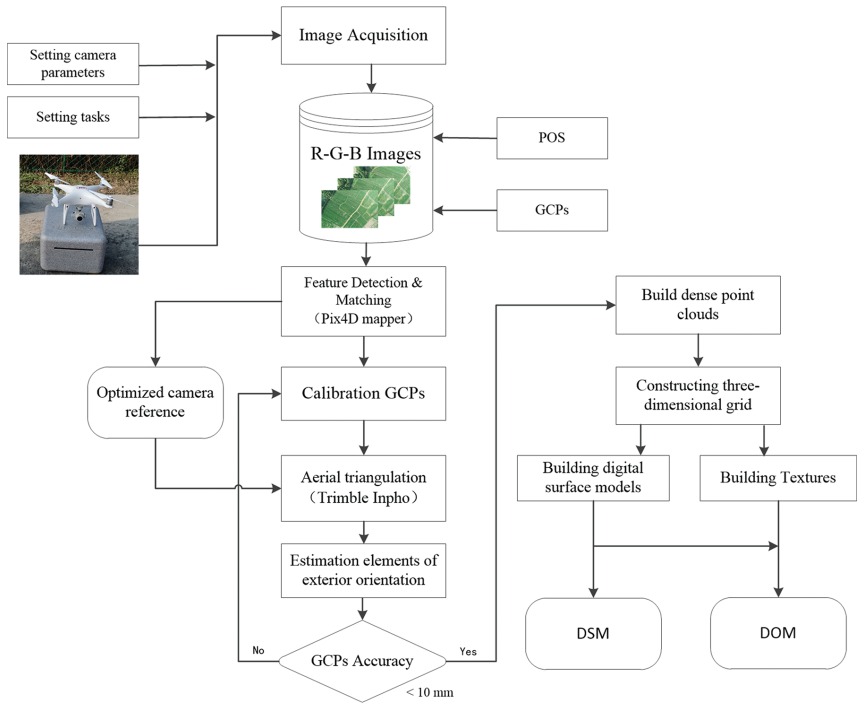

Figure 4. Flow chart of building Digital Surface Model (DSM) and digital orthophoto maps (DOM).

Principles of Rice Growth Prediction

The Difference Digital Surface Model (DDSM), which represents the value of rice plant height change at that growth stage, is produced by performing the difference operation of DSM for various fertility stages. It can be used as a monitoring index for rice growth. The calculation method for DDSM is as follows, and its principle is illustrated in Figure 5.

$$DSM_2 - DSM_1 = DDSM_1 \quad (1)$$

$$DSM_3 - DSM_2 = DDSM_2 \quad (2)$$

Point Cloud Filtering

When dense point clouds are produced from high-definition drone photos, outlier point clouds may appear. Outlier point clouds can be caused by interference within the sensor, arbitrary errors in multipath reflections, as well as environmental factors (sunlight reflections from the surface of the feature), and systematic errors in reconstructing the point cloud (Nurunnabi *et al.* 2018). Prior to conducting any analysis of the point cloud, it is normally necessary to identify and delete any aberrant point clouds that are either too big or too little in these outlier point clouds.

First, SOR filtering is used to test whether each point in the data is an outlier according to the relationship of normality in the distribution of distances to neighboring points(Rusu *et al.* 2008). SOR filtering is frequently used as one of the techniques to remove anomalous point clouds in the preprocessing of point cloud data since it has no prerequisites for topography and features and is more adaptable to doing so. Zeybek and Şanlıoğlu (2019) collected data from tens of millions of points in both urban and rural settings, and they discovered that the SOR filtering algorithm was effective in removing outliers. Sun *et al.* (2021) used a lidar measuring system to gather 3D point cloud data from rice fields and were successful in applying the SOR technique to successfully reduce anomalous point clouds that were far from the intended subject. Xianping *et al.* (2019) removed a significant portion of anomalous point clouds from non-target crops from the soybean canopy using the SOR algorithm in order to increase the efficacy and accuracy of plant height and volume extraction. As can be observed, the majority of the topography and vegetation are effectively filtered using the SOR algorithm. Second, as an enhancement to the conventional surface fitting approach, Professor Xiaohong Zhang of Wuhan University proposed QSF in 2004. The fundamental concept is that the terrain surface can be represented by a complicated spatial surface, and the relationship between the point cloud and the fitted surface is what determines whether or not to reject the point cloud. Su *et al.*(2009) used multi-level surface filtering to filter three typical terrain areas, and the filtering effect is the best in the area where there is a mixture of multiple features such as roads, vegetation, and buildings. The height threshold adaptive coefficient was introduced into the QSF method by Ji *et al.* (2021) in order to better identify ground points from non-ground locations. When Man *et al.* (2019) used lidar to scan the structure of the peanut canopy and a curve-fitting method to fit it, the height of the extracted peanut canopy was more precisely determined. As can be observed, the vegetation canopy can also benefit from point cloud filtering thanks to the QSF filtering method. In order to increase the accuracy of UAS monitoring of rice height change, two filtering techniques—SOR and QSF—are applied in this article.

SOR filtering algorithm: It determines the average separation between each point and its surroundings before excluding any that are more than many times the standard deviation away. The specific process of the SOR algorithm is as follows:

(1) Set the domain radius r and the standard deviation multiplier m
(2) Search for adjacent points within radius r and calculate the average value of the distance from the point to the adjacent points. The formula is as follows:

$$d_i = \frac{1}{n}\sum_{j=1}^{n}\left|x_i - x_j\right| \quad (3)$$

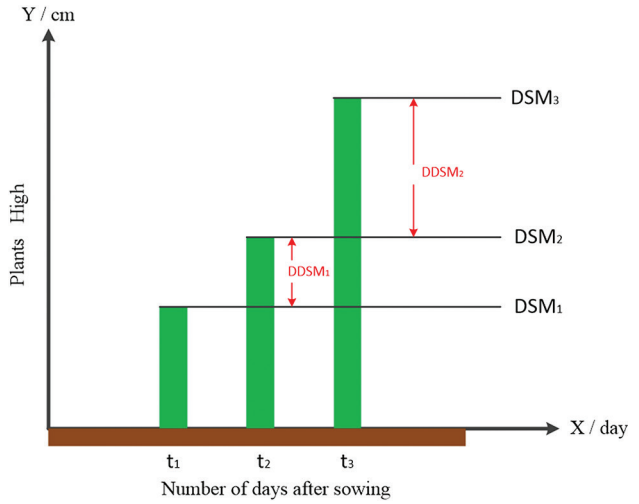

Figure 5. Principle of rice growth extraction. The Y-axis represents the height of rice growth, the X-axis represents the number of days of rice growth after sowing ($t_1 < t_2 < t_3$), and DSM_i (i = 1, 2, 3) is the height of rice after t_i (i = 1, 2, 3) days of growth after sowing.

(3) Calculate the mean value, standard deviation, and maximum distance to the point of these distance averages. The formula is as follows:

$$\mu = \frac{1}{n}\sum_{i=1}^{n} d_i \quad (4)$$

$$\partial^2 = \frac{1}{n}\sum_{i=1}^{n}\left(d_i - \mu\right)^2 \quad (5)$$

$$d_{max} = \mu + \mathrm{m} * \partial \quad (6)$$

If d_i is greater than d_{max}, the point is removed as an outlier, and vice versa, the point is retained and all point cloud data are traversed to complete the filtering.

The specific idea of QSF is: First, the point cloud is gridded, and a quadratic surface can be used to form a rough initial feature surface in a window of set size. All points within the window are statistically analyzed, and a height difference threshold is set to compare with the distance from the point cloud to the fitted surface within the window, and the points that exceed the given height difference threshold are eliminated. The expression for a quadratic surface is as follows:

$$Z_i = A_1 + A_2X_i + A_3Y_i + A_4X_iY_i + A_5X_i^2 + A_6Y_i^2 \quad (7)$$

In the formula: A_1–A_6 are the coefficients of the polynomial; X_i and Y_i denote the plane coordinates of the ith data point in the grid, and Z_i denotes its elevation.

Unified Geoid

In the current 3D point cloud reconstruction, the elevation value is one of the most challenging to control dimensions. Güngör *et al.* (2022) obtained a DOM with good spatial accuracy by measuring the coordinates using the Continuously Operating Reference Stations- Global Positioning System (CORS-GPS) technique and 10 GCPs. To produce DTMs and DOMs with high accuracy, Bayramoğlu and Uzar (2023) calibrated the UAS's digital cameras and measured the GCPs. When comparing the accuracy of the accuracy with and without GCPs, Senkal *et al.* (2021) collected UAS data on an archaeological site to create DSMs and DOMs. The results showed that the use of GCPs reduced the discrepancy from around 1 m to 5 cm. The change of rice plant height is derived by the DSM difference operation in different periods, and the geoid in each period needs to be consistent in order to get the genuine height change of rice plant height. Therefore, the GCP is more important for the unified geoid in order to obtain higher accuracy of rice plant height change.

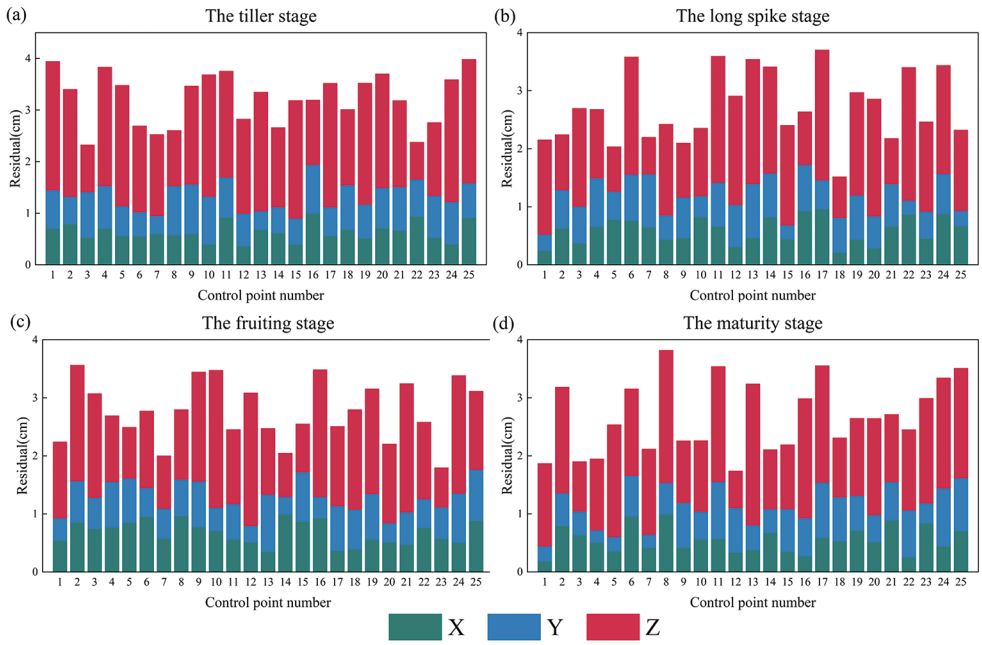

Figure 6. Residuals of image coordinates and measured coordinates of control points in each period (a) Control point residuals at the tiller stage, (b) Control point residuals at the long spike stage, (c) Control point residuals at the fruiting stage, (d) Control point residuals at the maturity stage.

Accuracy Evaluation Methods

The height of rice plant height change extracted using DDSM was subjected to linear regression analysis with the height of rice plant height change actually measured on the ground. The growth value of the rice as determined by DDSM was used as the independent variable in a regression analysis model, and the measured plant height served as the dependent variable. Indicators chosen to assess the model's accuracy include the coefficient of determination R^2, the root-mean-square error (RMSE), and the normalized root-mean-square error (nRMSE) (Jacovides and Kontoyiannis 1995; Moriasi *et al.* 2007). The model fits better when R^2 is closer to one, and the model's prediction accuracy increases with decreasing RMSE and nRMSE. The calculating equations are as follows, in order:

$$R^2 = \frac{\sum_{i=1}^{n}\left(X_i - \bar{X}\right)^2\left(Y_i - \bar{Y}\right)^2}{\sum_{i=1}^{n}\left(X_i - \bar{X}\right)^2\sum_{i=1}^{n}\left(Y_i - \bar{Y}\right)^2} \quad (8)$$

$$\mathrm{RMSE} = \sqrt{\frac{\sum_{i=1}^{n}\left(Y_i - X_i\right)^2}{n}} \quad (9)$$

$$\mathrm{nRMSE} = \frac{\mathrm{RMSE}}{\bar{X}} \times 100\% \quad (10)$$

In the formula: X_i, $\bar{X}$, Y_i, $\bar{Y}$, respectively, the measured value, the average value of the measured value, the predicted value and the average value of the predicted value, n denotes the number of model samples.

Results

Calibration

Although the UAS may theoretically obtain coordinates with centimeter-level accuracy, the UAS is constantly moving at a fast pace throughout the actual flying operation. While the UAS simultaneously gets signals directly from satellite navigation and maintains real-time communication with the remote control through its mapping and flight control systems. The positioning accuracy of the UAS will be degraded by the delay and interference between various signals. Therefore, it is required that the coordinates of the same name feature points of the images in each period correspond strictly. Before generating the DSM, the planar coordinates of the images of each period were corrected using 25 ground control points measured (30 ground control points were measured, but discarded because five control points could not be shown clearly in the images). The distribution of the residuals between the image coordinates of each control point and the measured coordinates after calibration (Figure 6) shows that the X and Y calibration errors of each control point are less than 10 mm, Z-axis residuals are around 1.5 cm, which can meet the accuracy requirements.

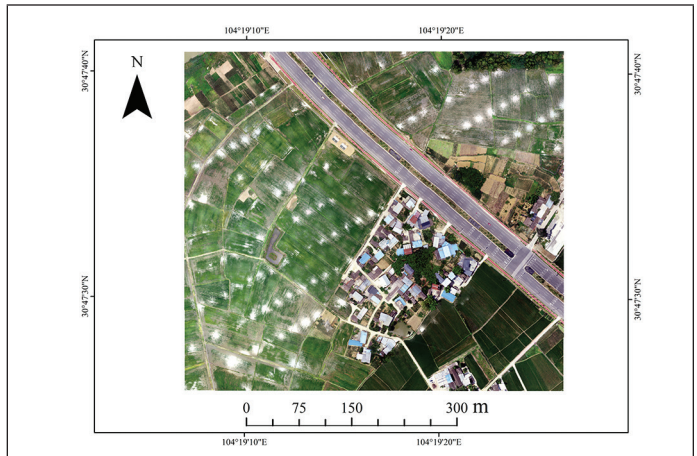

Figure 7. Digital orthophoto maps (DOM) at tiller stage.

At the tillering stage, the water surface of the rice field strongly reflected sunlight, which caused a significant number of white spots to develop on the DOM (Figure 7) and a significant number of outlier point clouds to form at the white spots in the DSM. Throughout the creation of the DSM, a few outlier point clouds still show up even if there aren't any white dots on the DOM during other stages. The accuracy of elevation datum correction is impacted by outlier point clouds near buildings, and the calculation error of DDSM is also increased by outlier point clouds over rice fields. The outlier point clouds must be taken out of the point cloud data for each period in order to increase the accuracy of the height of rice plant height change.

The DSM was filtered at each stage using SOR and QSF. By changing the parameters for the two outlier point cloud removal methods, it

was possible to assess the impact of parameter change on the outcomes of outlier point cloud removal. The initial count of point clouds was 154 420 032, and after establishing various filtering parameters, the changes in the number of point clouds and point cloud removal rate were determined (Tables 1 and 2). To achieve various filtering effects for QSF filtering, the window size and grid size should be jointly adjusted. The size of the QSF filtering window is determined here as a small window of 3 × 3, due to the limited space that rice plants occupy.

This study compares the point clouds of the concrete ground, houses, and strong sunlight reflection in the rice area before and after filtering (Figure 8) to assess the filtering effect. This study also looks to see if the number and geometry of the discrete points surrounding the filtered features are maintained in order to assess the filtering algorithm's ability to remove outliers. A high point cloud removal rate does not necessarily indicate a successful point cloud removal effect, as both filtering methods reveal local voids in the feature point clouds once the removal rate is larger than 5% (Figure 9). This increases the error of obtaining the plant growth height.

After comparing various parameters, it was found that the SOR filtering algorithm with the parameter settings r = 5 and m = 2 maintained 146 343 864 point clouds, had a decent outlier removal impact, and had a 4.2% point cloud removal rate. QSF filtering algorithm parameter setting: The moving window is 3 × 3, the grid size is 2, the height difference threshold is 2, the number of retained point clouds is 146 868 893, and the outlier, the removal effect is good, and the removal rate of the point cloud is 4.88%.

After point cloud filtering, the DSM of the crop became smoother and was able to remove the white spots caused by strong sunlight reflection during the tillering period.

Growth Extraction and Analysis

From the beginning of June until the end of September, rice in the research area grows and develops, and the plant height rises along with it. To get the DDSM that can extract the value of rice plant height change, the initial point cloud (IPC) (unfiltered) and the point cloud filtered by SOR and QSF were both subjected to the difference operation (Figure 10). The plant height of rice in that grid is determined by the DDSM using the average value of the point cloud in the grid of sampling points.

With maximum plant height growth values of 0.35 m, 0.65 m, and 0.18 m for Tiller stage to long spike stage (TTS), Fruiting stage to maturity (FTM), and Long spike stage to fruiting stage (LTF) rice, respectively, the DDSM plot's plant height growth was better in line with the actual growth. The aerial drone scan in September was conducted after the zone C rice crop had been harvested, hence the zone's plant height growth value was negative. Outlier points with a maximum positive growth value of 1.15 m and a maximum negative growth value of 2.25 m were visible in the IPC's DDSM. These anomalies' values deviate from the normal height change of rice plants. The filtered DDSM's values for

Table 1. Changes in outlier point clouds removal after filtering by statistical outlier removal (SOR) algorithm.

r	*m*	Number of Points	Point Cloud Removal Rate (%)
5	1	137 688 284	10.83
5	2	146 343 864	5.23
5	5	152 566 992	1.12
8	1	137 511 039	10.95
8	2	145 757 069	5.61
8	5	152 319 920	1.36
10	1	136 569 077	11.56
10	2	145 494 555	5.78
10	5	152 227 268	1.42

Note: The domain radius *r* and the standard deviation multiplier *m*.

Table 2. Changes in outlier point clouds removal after filtering by quadratic surface filtering (QSF) algorithm.

Grid Size	Height Difference	Number of Point Clouds	Point Cloud Removal Rate (%)
3	0.3	153 617 048	0.52
3	0.2	147 702 761	4.35
3	0.1	140 583 998	8.96
2	0.3	153 045 694	0.89
2	0.2	146 868 893	4.88
2	0.1	140 012 644	9.33
1	0.3	152 551 550	1.21
1	0.2	146 513 727	5.12
1	0.1	138 947 145	10.02

Figure 8. Point clouds of local cavity after filtering (top view).

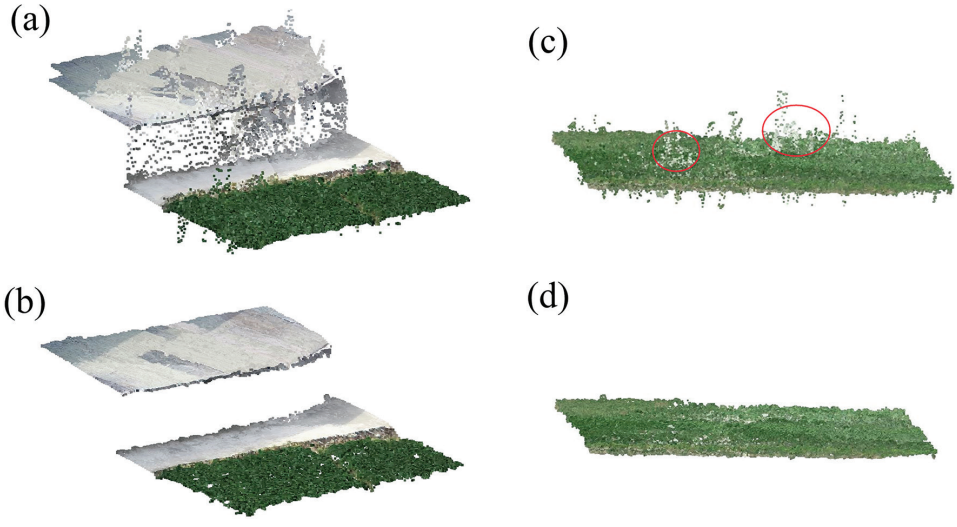

Figure 9. Comparison of the effect before and after filtering. (a) concrete and house before filtering, (b) concrete and house after filtering, (c) rice field before filtering, (d) rice field after filtering.

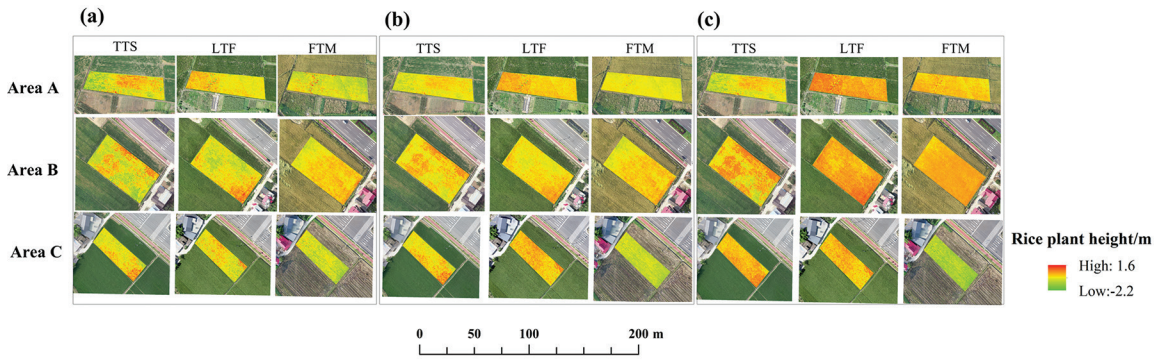

Figure 10. Extraction of rice growth based on differential digital surface model (DDSM). (a) DDSM of initial point cloud (IPC), (b) DDSM of quadratic surface filtering (QSF), (c) DDSM of statistical outlier removal (SOR). FTM, Fruiting stage to maturity; LTF, Long spike stage to fruiting stage; TTS, Tiller stage to long spike stage.

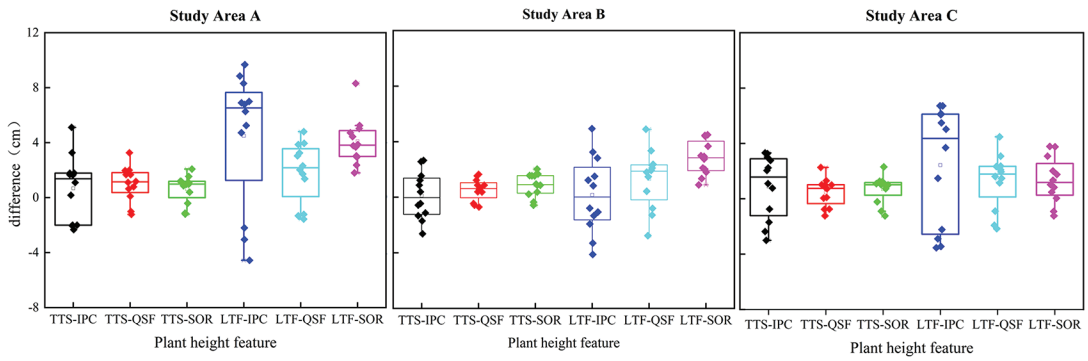

Figure 11. Difference between differential digital surface model (DDSM)-estimated rice plant height and measured plant height. Difference = measured rice height-DDSM estimated rice plant height. TTS-IPC, initial point cloud from tiller stage to long spike stage; TTS-QSF, quadratic surface filtering from tiller stage to long spike stage; TTS-SOR, statistical outlier removal filtering from tiller stage to long spike stage; LTF-IPC, initial point cloud from long spike stage to fruiting stage; LTF-QSF, quadratic surface filtering from the long spike to the fruiting stage; LTF-SOR, statistical outlier removal filtering from the long spike to the fruiting stage.

rice plant height change were within the expected range, there were no longer any outlier points, and the DDSM's surface was smoother.

Evaluation of Growth Prediction Accuracy

Statistical difference between the growth height extracted by DDSM and the measured height (Figure 11).

Figure 11 shows that the highest IPC departure from the observed value is 9 cm; however, the maximum deviation following filtering is just 5 cm. Indicating that both filtering algorithms improve the extraction of rice plant height change values, improve the accuracy of DDSM in estimating plant height change values, and have obvious effects on removing abnormal rice point clouds, the deviation values of both QSF and SOR are smaller than IPC. Despite the fact that the deviation value of SOR at TTS was significantly lower than that at QSF, it was slightly higher at LTF. The projected values were regressed against the measured values, and the coefficient of determination R^2 was compared with the root mean square error RMSE heat map to confirm the DDSM's accuracy in assessing rice plant height change (Figure 12).

We discovered that the filtered point cloud increased the accuracy of plant height change values by comparing the accuracy of rice plant height change of IPC with that of rice plant height change after using filtering. During different stages of rice development, the R^2 of IPC varied from 0.6 to 0.71; the R^2 of QSF was a maximum of 0.92 and a minimum of 0.73, mainly centered around 0.85; and the R^2 of SOR was a minimum of 0.84. Only in B TTS did the RMSE of IPC fall below 2 cm; otherwise, it increased to a maximum of 6.5 cm. After filtering, the RMSE of SOR varies greatly among the point clouds for each period, with a maximum of 4.41 cm and a minimum of 0.88 cm. The RMSE of QSF, on the other hand, was more stable and concentrated at around 2 cm, with a minimum of 0.79 cm. Regression analysis was performed on the pooled data from the three locations (Figure 13) to examine the accuracy improvement brought on by point cloud filtering over time.

The accuracy improvement is more influenced by filtering. R^2 grew during the TTS time from 0.63 to 0.84 and 0.87; during the LTF period, R^2 increased from 0.72 to 0.89 and 0.92; nRMSE fell during the TTS period from 10.85% to 6.67% and 6.41%; and during the LTF period from 10.65% to 5.21% and 6.89%. In both periods, the R^2 after filtering was higher than 0.8. Figure 13 demonstrates filtering the point cloud can more effectively eliminate outlier point clouds and increase accuracy. In general, SOR has a higher R^2 than QSF (0.92 versus 0.89; 0.89 versus 0.85), and the difference in RMSE between the two is not significant.

The outcomes demonstrate that filtering can increase the forecast accuracy of the UAS-based rice plant height change values. When the two filtering techniques are compared, it is discovered that the point cloud data after SOR filtering can more accurately forecast the fluctuation in rice plant height, making it the method with the potential for agricultural monitoring.

Discussion

The Causes of Abnormal Point Clouds Appearing

The reason there are so many white dots in Figure 7 is that the region saw a significant amount of rain in June, which resulted in a higher level of water in the paddy field. However, young rice seedlings can't totally block the water's surface because of their low height and frail branches. When the drone took pictures during periods of intense sunlight, the water surface in the rice field would significantly reflect the light, overexposing the pictures. During the tillering stage, this causes white spots in the DOM, which causes the DSM to additionally display a significant number of outlier point clouds. Outliers can also

be seen in Figure 9 near certain features. These outliers appear due to point clouds derived from high elevation features such as houses and trees near sidewalks when reconstructing point clouds from images. Rice fields near roads or houses will receive this outlier interference.

Filtering Error (False Positive Errors)

In this study, numerous outlier point clouds in DSM are removed using a filtering technique, including clustered outliers caused by intense sunlight reflections, outliers caused by feature diffraction, and outliers caused by systematic equipment defects. Although outlier point clouds can be more effectively removed using filtering techniques, when the filtering parameters vary, it is possible that the real feature point clouds will also be filtered out (false positive errors). It is required to recover these erroneously filtered points through extra processing because when the outlier point clouds are totally removed, the actual feature's point clouds are likewise partially filtered. Eight different interpolation approaches are used by Akar (2017) to generate DEMs for flat and sloping terrain, and kriging interpolation methods provide better DEMs for both terrain types. So point cloud interpolation might be seen as a way to get back points that were filtered erroneously. Other filtering algorithms (surface-based filtering, local outlier factor (LOF)-based filtering, etc.) weren't investigated in this study besides SOR algorithm filtering and QSF. Therefore, more research is required to show the enhancement of various filtering techniques on the precision of rice plant height change prediction.

Analysis of Rice Plant Height Growth

Figure 11 shows that the height of rice plants varies significantly at the TTS, FTM, and LTF phases, with values of 0.35 m, 0.65 m, and 0.18 m, respectively. This is due to rice's anisotropic growth. The growth rate of rice is not consistently maintained. From the seedling to the mature stage, the growth rate of rice changes, going from slow, to quick, to slow once more. Slow growth in rice seedlings; the rice will grow more quickly under conditions with more fertilizer, moisture, and heat. Once the rice has begun to progressively mature, the rate of plant height development slows down once more. During the TTS period, rice plant height varies more, and the DDSM surface is rougher. This is so that bare soil can remain between nearby rice plants due to the sparse branches and leaves of rice during the tillering stage. Following a time of growth and development, the leaves thicken and spread out in all directions. Additionally, the leaves of nearby rice plants will cross one another and provide shade for the surrounding area. The rice plant height change will be higher than usual if the previous bare ground height is subtracted from the current rice height. However, some rice is malnourished or grows slowly as a result of pests and diseases, causing it to be stunted or even wilt. This rice will have low (or negative) height change values. The values of rice plant height change are more evenly distributed when the rice is mature, and the canopy has grown to the point where it may shade the lower mat and make a level surface in the canopy.

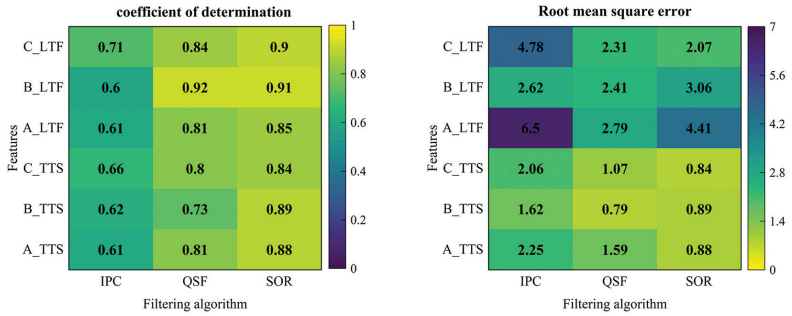

Figure 12. Heat map of correlation coefficient and root mean square error between measured plant height and estimated plant height after different filtering algorithms. A_TTS, area A from tiller stage to long spike stage; B_TTS, area B from tiller stage to long spike stage; C_TTS, area C from tiller stage to long spike stage; A_LTF, area A from the long spike to the fruiting stage; B_LTF, area B from the long spike to the fruiting stage; C_LTF, area C from the long spike to the fruiting stage.

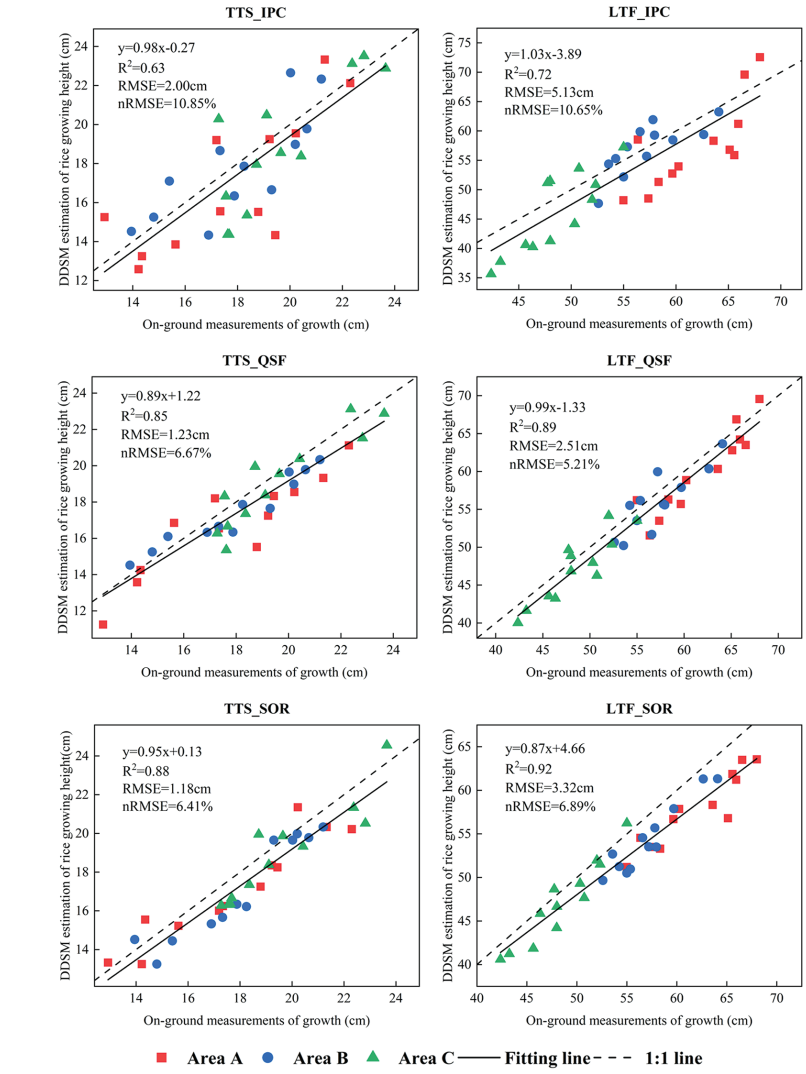

Figure 13. Comparison of differential digital surface model (DDSM) estimated rice plant height and measured growth. TTS_IPC, initial point cloud from tiller stage to long spike stage; TTS_QSF, quadratic surface filtering from tiller stage to long spike stage; TTS_SOR, statistical outlier removal filtering from tiller stage to long spike stage; LTF_IPC, initial point cloud from long spike stage to fruiting stage; LTF_QSF, quadratic surface filtering from the long spike to the fruiting stage; LTF_SOR, statistical outlier removal filtering from the long spike to the fruiting stage. Note: The TTS and LTF rice plant height change scales are different, and therefore the horizontal and vertical coordinate ranges in the plots are also different.

Analysis of the Accuracy of Rice Plant Height Prediction

The DDSM in Figure 13 demonstrates that while the values of growth change predicted by the IPC DDSM always created bigger swings around the observed height, the values of rice plant height change assessed by the filtered DDSM were all only marginally lower than the measured height. This might be because, during the actual measurement, the height of the top branches of the rice was measured by straightening them rather than by the weight of the rice ears causing the top of the rice to droop downward. The differences between projected and measured DDSM heights varied over time as a result of the anisotropy of rice growth rate. For instance, the LTF deviation was more than the TTS deviation: the average LTF deviation was 3.65 cm greater than the average TTS deviation of 1.47 cm. The average plant height change of LTF was 48 cm greater than the average plant height change of TTS, which was 18 cm, and the accelerated growth rate increased the deviation of the DDSM forecast rice plant height, which was the reason for this.

Future

The current hot topic in fine agriculture is the use of UAS to swiftly and effectively gather crop information and conduct research on crop growth and development, fertilizer distribution, etc. Crop growth prediction by DSM offers significant application value for the use of fine-grained agriculture. There are many other factors that affect the accuracy of crop monitoring, such as the spatial resolution of UAS data and field wind magnitude under the same UAS equipment conditions, which need to be discussed in order to further increase the accuracy of UAS monitoring of crop growth. The spatial resolution of the data is determined by the UAS's flight altitude. If there is a link between flight altitude and point cloud information, there is a need for additional models to calibrate and validate this relationship. The wind is also one of the key factors in obtaining high-quality images. During the flight of the UAS, not only the natural wind but also the wind speed generated by the UAS over the crop (the intensity increases as the flight altitude decreases). High winds in the field can move the crop canopy and introduce positional errors when the UAS photographs the same crop at different locations; when the wind has a downward slope to the crop canopy, the crop height extracted from the UAS data may be lower than the actual crop height. As a result, it will be crucial to overcome the major problems that currently prevent UAS from accurately monitoring crops in the future. Instead of laborious semi-automatic extraction of crop growth, crop monitoring should enable an integrated and automated image-gathering method to simulate crop growth.

Conclusion

In this work, UAS photos, GCP data, and POS data were used to construct DSM and DOM. After using the GCP unified geodetic level, removing the interference of outlier point clouds is a key issue in predicting the rice plant height change. The following findings in this study were reached through experimentation.

(1) This study suggests choosing correction points on characteristics that do not change over time, unifying the DSM datum for each period, and creating a datum correction model in order to unite the datum. The unified benchmark improves the accuracy of rice plant height extraction and eliminates the influence of rice topography and water surface in different periods.

(2) SOR and QSF are used to eliminate the outlier point clouds produced during the creation of the DSM. The findings demonstrate that, in comparison to IPC estimation, the filtered estimation's accuracy has greatly increased. In particular, there is a strong correlation between predicted rice height and actual measured plant height following filtering using the SOR algorithm.

In comparison to uncorrected UAS data, the approach used in this work improves the extraction of rice height and offers improved accuracy of rice height prediction. The technique is more efficient and practical, removes subjective errors, and is more practical. It has a larger capacity for use in large-scale agricultural production.

Acknowledgments

This research was assisted by the GIS_RS Laboratory, College of Earth Sciences, Chengdu University of Technology. This work was supported by the Chengdu Science and Technology Innovation R&D Project (2022-YF05-01090-SN), the National Natural Science Foundation of China (NSFC) (41871303), the Sichuan Provincial Science and Technology Program (2021YFG0365), the Sichuan Provincial Department of Natural Resources Scientific Research Project (KJ-2021-3), and the Chengdu University of Technology Postgraduate Quality Project (2022YJG022).

References

Akar, A. 2017. Evaluation of accuracy of DEMs obtained from UAV-point clouds for different topographical areas. *International Journal of Engineering and Geosciences* 2(3):110–117. https://doi.org/10.26833/ijeg.329717.

Baluja, J., M.P. Diago, P. Balda, R. Zorer, F. Meggio, F. Morales, and J. Tardaguila. 2012. Assessment of vineyard water status variability by thermal and multispectral imagery using an unmanned aerial vehicle (UAV). *Irrigation Science* 30(6):511–522. https://doi.org/10.1007/s00271-012-0382-9.

Bayramoğlu, Z. and M. Uzar. 2023. Performance analysis of rule-based classification and deep learning method for automatic road extraction. *International Journal of Engineering and Geosciences* 8(1):83–97. https://doi.org/10.26833/ijeg.1062250.

Bendig, J., A. Bolten, S. Bennertz, J. Broscheit, S. Eichfuss, and G. Bareth. 2014. Estimating biomass of barley using crop surface models (CSMs) derived from UAV-based RGB imaging. *Remote Sensing* 6(11):10395–10412. https://doi.org/10.3390/rs61110395.

Burkart, A., V. L. Hecht, T. Kraska, and U. Rascher. 2018. Phenological analysis of unmanned aerial vehicle based time series of barley imagery with high temporal resolution. *Precision Agric* 19(1):134–146. https://doi.org/10.1007/s11119-017-9504-y.

Candiago, S., F. Remondino, M. De Giglio, M. Dubbini, and M. Gattelli. 2015. Evaluating multispectral images and vegetation indices for precision farming applications from UAV *Images. Remote Sensing* 7(4):4026–4047. https://doi.org/10.3390/rs70404026.

Cen, H., L. Wan, J. Zhu, Y. Li, X. Li, Y. Zhu, H. Weng, W. Wu, W. Yin, C. Xu, Y. Bao, L. Feng, J. Shou, and Y. He. 2019. Dynamic monitoring of biomass of rice under different nitrogen treatments using a lightweight UAV with dual image-frame snapshot cameras. *Plant Methods* 15(1):32. https://doi.org/10.1186/s13007-019-0418-8.

Chang, A., J. Jung, M. M. Maeda, and J. Landivar. 2017. Crop height monitoring with digital imagery from Unmanned Aerial System (UAS). *Computers and Electronics in Agriculture* 141:232–237. https://doi.org/10.1016/j.compag.2017.07.008.

Chang, A., Y. Eo, S. Kim, Y. Kim, and Y. Kim. 2011. Canopy-cover thematic-map generation for Military Map products using remote sensing data in inaccessible areas. *Landscape and Ecological Engineering* 7(2):263–274. https://doi.org/10.1007/s11355-010-0132-1.

Gil-Docampo, M. L., M. Arza-García, J. Ortiz-Sanz, S. Martínez-Rodríguez, J. L. Marcos-Robles, and L. F. Sánchez-Sastre. 2020. Above-ground biomass estimation of arable crops using UAV-based SfM photogrammetry. *Geocarto International* 35(7):687–699. https://doi.org/10.1080/10106049.2018.1552322.

Guo, G., Q. Wen, and J. Zhu. 2015. The impact of aging agricultural labor population on farmland output: From the perspective of farmer preferences. mathematical problems in engineering. 2015:1–7. https://doi.org/10.1155/2015/730618.

Güngör, R., M. Uzar, B. Atak, O. S. Yilmaz, and E. Gümüş. 2022. Orthophoto production and accuracy analysis with UAV photogrammetry. *Mersin Photogrammetry Journal* 4(1):1–6. https://doi.org/10.53093/mephoj.1122615.

Jacovides, C. P. and H. Kontoyiannis. 1995. Statistical procedures for the evaluation of evapotranspiration computing models. *Agricultural Water Management* 27(3–4):365–371. https://doi.org/10.1016/0378-3774(95)01152-9.

Jimenez-Berni, J. A., D. M. Deery, P. Rozas-Larraondo, A. (Tony) G. Condon, G. J. Rebetzke, R. A. James, W. D. Bovill, R. T. Furbank, and X.R.R. Sirault. 2018. High throughput determination of plant height, ground cover, and above-ground biomass in wheat with LiDAR. *Frontiers in Planet Science* 9:237. https://doi.org/10.3389/fpls.2018.00237.

Ji, YT. Zhang, CK. Yin, Y. 2021. An Adaptive Filtering Algorithm for Airborne LiDAR Point Cloud. *Journal of Geomatics Science and Technology.* 38(2): 142-147.

Li, W., Z. Niu, N. Huang, C. Wang, S. Gao, and C. Wu. 2015. Airborne LiDAR technique for estimating biomass components of maize: A case study in Zhangye City, Northwest China. *Ecological Indicators* 57:486–496. https://doi.org/10.1016/j.ecolind.2015.04.016.

Lear, A. C. 1997. Digital orthophotography: Mapping with pictures. *IEEE Computer Graphics and Applications* 17(5):12–14. https://doi.org/10.1109/38.610196.

Lowe, D. G. 2004. Distinctive image features from scale-invariant keypoints. *International Journal of Computer Vision* 60(2):91–110. https://doi.org/10.1023/B:VISI.0000029664.99615.94.

Man, C., C. Zhenjiang, and N. Wang. 2019. System design for peanut canopy height information acquisition based on LiDAR. *Transactions of the Chinese Society of Agricultural Engineering* 35(1):1002–6819.

Matese, A., S. F. Di Gennro, and A. Berton. 2017. Assessment of a canopy height model (CHM) in a vineyard using UAV-based multispectral imaging. *International Journal of Remote Sensing* 38(8–10):2150–2160. https://doi.org/10.1080/01431161.2016.1226002.

Matese, A., P. Toscano, S. Di Gennaro, L. Genesio, F. Vaccari, and J. Primicerio, C. Belli, A. Zaldei, R. Bianconi, and B. Gioliet. 2015. Intercomparison of UAV, aircraft and satellite remote sensing platforms for precision viticulture. *Remote Sensing* 7(3):2971–2990. https://doi.org/10.3390/rs70302971.

Mesas-Carrascosa, F.-J., J. Torres-Sánchez, I. Clavero-Rumbao, A. García-Ferrer, J.-M. Peña, I. Borra-Serrano, and F. López-Granadoset. 2015. Assessing optimal flight parameters for generating accurate multispectral orthomosaicks by UAV to support site-specific crop management. *Remote Sensing* 7(10):12793–12814. https://doi.org/10.3390/rs71012793.

Moriasi, D. N., J. G. Arnold, M. W. Van Liew, R. L. Bingner, R. D. Harmel, and T. L. Veith. 2007. Model evaluation guidelines for systematic quantification of accuracy in watershed simulations. *Transactions of the ASABE* 50(3):885–900. https://doi.org/10.13031/2013.23153.

Nurunnabi, A., Y. Sadahiro, and D. F. Laefer. 2018. Robust statistical approaches for circle fitting in laser scanning three-dimensional point cloud data. *Pattern Recognition* 81:417–431. https://doi.org/10.1016/j.patcog.2018.04.010.

Olson, D. and J. Anderson. 2021. Review on unmanned aerial vehicles, remote sensors, imagery processing, and their applications in agriculture. *Agronomy Journal* 113(2):971–992. https://doi.org/10.1002/agj2.20595.

Rasmussen, J., G. Ntakos, J. Nielsen, J. Svensgaard, R. N. Poulsen, and S. Christensen. 2016. Are vegetation indices derived from consumer-grade cameras mounted on UAVs sufficiently reliable for assessing experimental plots? *European Journal of Agronomy* 74:75–92. https://doi.org/10.1016/j.eja.2015.11.026.

Rey-Caramés, C., M. Diago, M. Martín, A. Lobo, and J. Tardaguila. 2015. Using RPAS multi-spectral imagery to characterise vigour, leaf development, yield components and berry composition variability within a vineyard. *Remote Sensing* 7(11):14458–14481. https://doi.org/10.3390/rs71114458.

Rusu, R. B., Z. C. Marton, N. Blodow, M. Dolha, and M. Beetz. 2008. Towards 3D point cloud based object maps for household environments. *Robotics and Autonomous Systems* 56(11):927–941. https://doi.org/10.1016/j.robot.2008.08.005.

Senkal, E., G. Kaplan, and U. Avdan. 2021. Accuracy assessment of digital surface models from unmanned aerial vehicles' imagery on archaeological sites. *International Journal of Engineering and Geosciences* 6(2):81–89. https://doi.org/10.26833/ijeg.696001.

Snavely, N., S. M. Seitz, and R. Szeliski. 2008. Modeling the world from internet photo collections. *International Journal of Computer Vision* 80(2):189–210. https://doi.org/10.1007/s11263-007-0107-3.

Su, W., Z.-p. Sun, D.-l. Zhao, C.-l. Sun, C. Zhang, and J.-yu Yang. 2009. Hierarchical moving curved fitting filtering method based on LIDAR data. *Journal of Remote Sensing* 13:827–832.

Sun, Y., Y. Luo, X. Chai, P. Zhang, Q. Zhang, L. Xu, and L. Wei. 2021. Double-threshold segmentation of panicle and clustering adaptive density estimation for mature rice plants based on 3D point cloud. *Electronics* 10(7):872. https://doi.org/10.3390/electronics10070872.

Tang, Y., M. Chen, C. Wang, L. Luo, J. Li, G. Lian, and X. Zou. 2020. Recognition and localization methods for vision-based fruit picking robots: A Review. *Frontiers in Plant Science* 11:510. https://doi.org/10.3389/fpls.2020.00510.

Wang, J., B. Wu, M. V. Kohnen, D. Lin, C. Yang, X. Wang, A. Qiang, W. Liu, J. Kang, H. Li, J. Shen, T. Yao, J. Su, B. Li, and L. Gu. 2021. Classification of rice yield using UAV-based hyperspectral imagery and lodging feature. *Plant Phenomics* 2021:1–14. https://doi.org/10.34133/2021/9765952.

Westoby, M. J., J. Brasington, N. F. Glasser, M. J. Hambrey, and J. M. Reynolds. 2012. 'Structure-from-Motion' photogrammetry: A low-cost, effective tool for geoscience applications. *Geomorphology* 179:300–314. https://doi.org/10.1016/j.geomorph.2012.08.021.

Xianping, G., L. Kuan, Q. Baijing, D. Xiaoya, and X. Xinyu. 2019. Double-threshold segmentation of panicle and clustering adaptive density estimation for mature rice plants based on 3D point cloud. *Transactions of the Chinese Society of Agricultural Engineering* 35(23):1002-6819.

Xie, T., J. Li, C. Yang, Z. Jiang, Y. Chen, L. Guo, and J. Zhang. 2021. Crop height estimation based on UAV images: Methods, errors, and strategies. *Computers and Electronics in Agriculture* 185:106155. https://doi.org/10.1016/j.compag.2021.106155.

Yu, N., L. Li, N. Schmitz, L. F. Tian, J.A. Greenberg, and B. Diers. 2016. Development of methods to improve soybean yield estimation and predict plant maturity with an unmanned aerial vehicle based platform. *Remote Sensing of Environment* 187:91–101. https://doi.org/10.1016/j.rse.2016.10.005.

Yuantian, J., Z. Chunkang, and Y. Yao. 2021. An adaptive filtering algorithm for airborne LiDAR point cloud. *Journal of Geomatics Science and Technology* 38(2):1673–6338.

Yue, J., H. Feng, X. Jin, H. Yuan, Z. Li, C. Zhou, G. Yang, and Q. Tian. 2018. A comparison of crop parameters estimation using images from UAV-mounted snapshot hyperspectral sensor and high-definition digital camera. *Remote Sensing* 10(7):1138. https://doi.org/10.3390/rs10071138.

Zeybek, M. 2021a. Accuracy assessment of direct georeferencing UAV images with onboard global navigation satellite system and comparison of CORS/RTK surveying methods. Measurement Science and Technology 32(6):065402. https://doi.org/10.1088/1361-6501/abf25d.

Zeybek, M. 2021b. Inlier point preservation in outlier points removed from the ALS point cloud. *Journal of the Indian Society of Remote Sensing* 49(10):2347–2363. https://doi.org/10.1007/s12524-021-01397-4.

Zeybek, M. and İ. Şanlıoğlu. 2019. Point cloud filtering on UAV based point cloud. *Measurement* 133:99–111. https://doi.org/10.1016/j.measurement.2018.10.013.

Zhou, X., H. B. Zheng, X. Q. Xu, J. Y. He, X. K. Ge, X. Yao, T. Cheng, Y. Zhu, W. X. Cao, and Y. C. Tian. 2017. Predicting grain yield in rice using multi-temporal vegetation indices from UAV-based multispectral and digital imagery. *ISPRS Journal of Photogrammetry and Remote Sensing* 130:246–255. https://doi.org/10.1016/j.isprsjprs.2017.05.003.

Ziliani, M., S. Parkes, I. Hoteit, and M. McCabe. 2018. Intra-season crop height variability at commercial farm scales using a fixed-wing UAV. *Remote Sensing* 10(12):2007. https://doi.org/10.3390/rs10122007.

Spherical Hough Transform for Robust Line Detection Toward a 2D–3D Integrated Mobile Mapping System

Daiwei Zhang, Bo Xu, Han Hu, Qing Zhu, Qiang Wang, Xuming Ge, Min Chen, and Yan Zhou

Abstract

Line features are of great importance for the registration of the Vehicle-Borne Mobile Mapping System that contains both lidar and multiple-lens panoramic cameras. In this work, a spherical straight-line model is proposed to detect the unified line features in the panoramic imaging surface based on the Spherical Hough Transform. The local topological constraints and gradient image voting are also combined to register the line features between panoramic images and lidar point clouds within the Hough parameter space. Experimental results show that the proposed method can accurately extract the long strip targets on the panoramic images and avoid spurious or broken line-segments. Meanwhile, the line matching precision between point clouds and panoramic images are also improved.

Introduction

The Vehicle-Borne Mobile Mapping System, equipped with panoramic cameras, laser scanners, access to the Global Positioning System, and an Inertial Measurement Unit, has been widely used for highway inventory (Cui *et al.* 2016; Hussnain *et al.* 2021; Puente *et al.* 2013). The data acquired from these systems integrate rich geometry and spectral information, thus enabling new solutions to the understanding and modeling of roads and their ancillary facilities (Ren *et al.* 2022; Yuan *et al.* 2022). However, considerable misalignment often exists between the panoramic images and the lidar point clouds because of inaccurate pre-calibrated parameters. The main reasons for this misalignment are the unforeseen movement of the independent sensors during relocation and the projection deformation of images (Bao *et al.* 2022). Therefore, the relevant extrinsic parameters must be calibrated manually and frequently, which is laborious. Many studies have explored the use of panoramic cameras and laser scanners (Akca 2010; Alba *et al.* 2011; Cui *et al.* 2016; Zhang and Cui 2022), which can be separated into three categories (Li *et al.* 2018): area-based, multi–view-based and feature-based.

Area-based methods iteratively project the point clouds to the image surface and calculate the statistical correlation between the projected results and the two-dimensional (2D) images, i.e., using mutual information (Miled *et al.* 2016) or grayscale similarity. The relevant extrinsic parameters are then decided by maximizing the statistical correlation. The main problem with such methods is that the correlation between depth information and color information is not significant in many scenes (Wang *et al.* 2012). Because of the difficulties of 2D–three-dimensional (3D) registering between different data models, multi–view-based approaches first generate 3D point clouds from multiple view images and then convert the issue into 3D–3D registration. The main difficulty with such approaches is that the image point clouds are influenced by drift, leading to a non-rigid transformation between the two point clouds (Li *et al.* 2018).

Compared with the above methods, feature-based methods are more efficient and adaptive (Miled *et al.* 2016) and are thus widely used in current applications. In feature-based methods, the key factor is to find the correct matching feature pairs between images and point clouds regardless of the point (i.e., SIFT (Lowe 2004), ASIFT (Morel and Yu 2009)), line (i.e., the Line Segment Detector (LSD) (Von Gioi *et al.* 2008)) or plane features. Because images and point clouds have different modes and dimensions, point-based features may have low consistency or repetition rates, leading to misalignment (Yang and Chen 2015). Plane-based features require regular shaped human-made objects for planar surfaces, such as buildings, which may not be available in scenes such as highways. As a result, line-based methods with high repetition rates and ease of expressing the scene structure have drawn increasing attention (Zhang *et al.* 2008). The problem with feature-based methods is the distortion of panoramic images. For example, a straight line in space appears as a curve on a panoramic image because of image deformation. Current studies mainly deal with this issue via the distortion correction of panoramic images, which limits the corrected image to a specific perspective but decreases matching precision and efficiency.

Figure 1. Distortion of straight lines on a panoramic image of a highway scene.

To address this issue, this work proposes the spherical straight line model, which directly constructs the connection between the 3D straight lines within the Hough space. This work makes two main contributions:

Daiwei Zhang, Qing Zhu, and Qiang Wang are with the Faculty of Geomatics, Lanzhou Jiaotong University, Lanzhou, China.

Bo Xu, Han Hu, Xuming Ge, Qing Zhu, and Min Chen are with the Faculty of Geosciences and Environmental Engineering, Southwest Jiaotong University, Chengdu, China (xubo@swjtu.edu.cn).

Yan Zhou is with the School of Resources and Environment, University of Electric Science and Technology, Chengdu, China and The Key Laboratory of Urban Land Resources Monitoring and Simulation, Ministry of Natural Resources, Shenzhen, China.

Contributed by Bo Wu, August 21, 2022 (sent for review October 11, 2022; reviewed by Ningning Zhu, Yuan Li).

Photogrammetric Engineering & Remote Sensing
Vol. 89, No. 5, May 2023, pp. 311–320.
0099-1112/22/311–320
© 2023 American Society for Photogrammetry and Remote Sensing
doi: 10.14358/PERS.22-00112R2

1. It describes the spherical straight lines on the panoramic images and the corresponding line extraction approach based on the Hough transform (HT).
2. It presents a robust 2D–3D line matching strategy for point cloud and panoramic images by combining local topological constraints and gradient image voting.

The remainder of the paper is organized as follows. The section "Related Work" reviews and analyzes the related work. The details of the 3D straight line feature extraction and matching strategy are introduced in the section "Methodology". Experimental analysis and evaluation of the proposed approach are provided in the "Experiment and Results" section. The last section concludes the paper.

Related Work

Research online feature detection and matching dates to the early stage of computer vision research. Because we mainly consider the corresponding line features between a 2D panoramic image and 3D lidar point clouds in the highway scene, we first review the detection methods for line segments for both 2D images and 3D point cloud. Then, we introduce the representative line matching strategies.

2D Line Segments from Images

Generally, the extraction of 2D image line segments can be divided into three major categories: growing-based, fitting-based, and learning-based approaches.

Growing-based approaches adopt a bottom-up strategy, starting with the edge or corner pixels and growing them to meet the requirement of the lines (You and Lin 2011). State-of-the-art methods include the well-known LSD (Von Gioi *et al.* 2008) and Edge Drawing (Akinlar and Topal 2011; Topal and Akinlar 2012) methods. These methods are relatively fast and simple and can support real-time applications. However, they are sensitive to noise, and a long line segment might be broken into several pieces.

Fitting-based methods use a top-down strategy that extracts true straight lines before they are broken into segments. Such methods must be able to detect the object edges, first using the Canny (1986) or Edison edge detector and then fitting the lines using an algorithm such as the HT (Rahmdel *et al.* 2015) or random sample consensus (RANSAC) (Choi *et al.* 2009) methods. Once the best line parameters are extracted, the endpoints of the line segments can be generated by projecting the outermost edge pixels to the true lines. Many studies have adopted such a strategy using the HT and RANSAC families (Aggarwal and Karl 2006; Ballard 1981; Duda and Hart 1972; Fernandes and Oliveira 2008). These methods have been shown to be robust in the presence of noise and to be able to detect long and broken line segments. However, they are limited by high computation and memory costs and inaccuracy in detecting short lines.

In recent years, end-to-end deep learning approaches have been used to extract image line segments directly (Li *et al.* 2021; Ahmad *et al.* 2017; Zhang *et al.* 2019; Zhou *et al.* 2019). In (Law and Deng 2018), line segments are extracted as a pair of key points. Lee *et al.* (2017) extract the semantic straight line based on the two-branch pipeline of faster Region-Based Convolutional Neural Networks. Other works detect line segments in wire-frame parsing (Huang *et al.* 2018; Zhou *et al.* 2019). In work of (Li *et al.* 2021), the line features on the panoramic image surface are also detected. However, such approaches are limited by their high demand for training data and the migration ability. In addition, because the line-wise feature is often extracted based on LoI(Line of Interest) pooling, the contextual information can be inadequate.

3D Line Segments from Point Clouds

Studies on 3D line segments are relatively scarce and can be generally divided into three categories (Lu *et al.* 2019): point-based, plane-based, and image-based.

Point-based approaches (Awrangjeb 2016; Bazazian *et al.* 2015; Lin *et al.* 2017) detect the boundary points first and then fit the 3D line segments. The boundaries can be found via data-driven methods such as convex hull algorithms, the alpha shape method or triangulation network tracking (Sampath and Shan 2007). In addition, based on the designed features, classification methods can be used in boundary and non-boundary categories (Hackel *et al.* 2016; Weber *et al.* 2010). Once boundary points are generated, the line features can be fitted using RANSAC, HT, or least square methods. The main limitations of these methods are that they are susceptible to noise and that spurious line segments can be extracted given uneven point density and holes caused by occlusion.

Plane-based methods consider the lines as intersections of adjacent planar surfaces (Xu *et al.* 2017). These methods have shown advantages in urban scenes containing many buildings. The points from building roofs are first divided into plane segments based on segmentation methods such as region growing or RANSAC (Xu *et al.* 2016), and the existence of line segments is determined according to the plane topology analysis (Elberink and Vosselman 2009), i.e., by considering the number of points near the mathematical line. Although the intersected lines are more precise in theory, the range of scenes for which they are suitable is limited, and they have problems dealing with boundaries of small or narrow planes.

Image-based methods extract planar surfaces first and then convert the points within the plane into images with point color, intensity, or depth (Lin *et al.* 2015). 2D line detection algorithms such as LSD (Von Gioi *et al.* 2008) can be used to extract line segments from the converted image; then, these 2D line segments are back-projected to the 3D space to obtain the final results. However, such methods are limited regarding the generation strategy of the converted image, including the determination of image resolution and the viewpoints.

2D–3D Line Matching

Unlike traditional point-wise matching between images and point clouds, research online-based 2D–3D matching is still in an early stage, mainly because of difficulties in identifying the similarities of features with different dimensions and modes. Thus, many studies convert the data into the same dimensions first, mostly by projecting the point clouds into the image plane. The color values of the projected images can then be represented by a great deal of information, including intensity, depth, and RGB colors. The main problem is that existing line matching models use a 2D–3D linear constraint model of a line or a point on the image (Cui *et al.* 2016):

$$\boldsymbol{x}_e + \lambda(\boldsymbol{x}_b - \boldsymbol{x}_a) = \boldsymbol{R}^T(\boldsymbol{P} - \boldsymbol{t}) \tag{1}$$

where $\boldsymbol{P}$ is an arbitrary point on a line in space, $\boldsymbol{R}$ and $\boldsymbol{t}$ are the outer orientation elements of the image, $\boldsymbol{x}_a$ and $\boldsymbol{x}_b$ are the endpoints of the corresponding line segment on the image, and λ is a scale parameter. However, for highway scenes where long linear targets are dominant, 3D line features might be manifested as curved lines in the panoramic mode. Current line detecting or matching approaches will separate the line segments into broken pieces, leading to poor matching results. In this work, we propose a Spherical Hough Transform method based on the Spherical Straight Line model for long linear feature extraction and matching.

Methodology

Overview

In this work, the spherical straight line pairs between 2D panoramic images and 3D point clouds are extracted and matched via the spherical Hough transform. The workflow is proposed in Figure 2. First, line segments are detected from both sides. On the panoramic image side, because of the deformation of spherical projection, the spherical line features may no longer be straight lines; thus, we extract the boundary features first and then search for the lines using spherical Hough transform according to the edge pixels. The line features from the point cloud side are detected, including the landmarks, guardrails, and edges of the signboards. These line features are clustered according to their orientations. Next, the line features from both sides are matched within the Hough space based on their topological constraints. Finally, we determine the endpoint of the line feature according to the features from both sides to achieve the matched line segments.

Line Segments from Point Clouds

This section presents the approach to extracting the 3D line segments from lidar point clouds. Compared with urban scenes, road scenes are

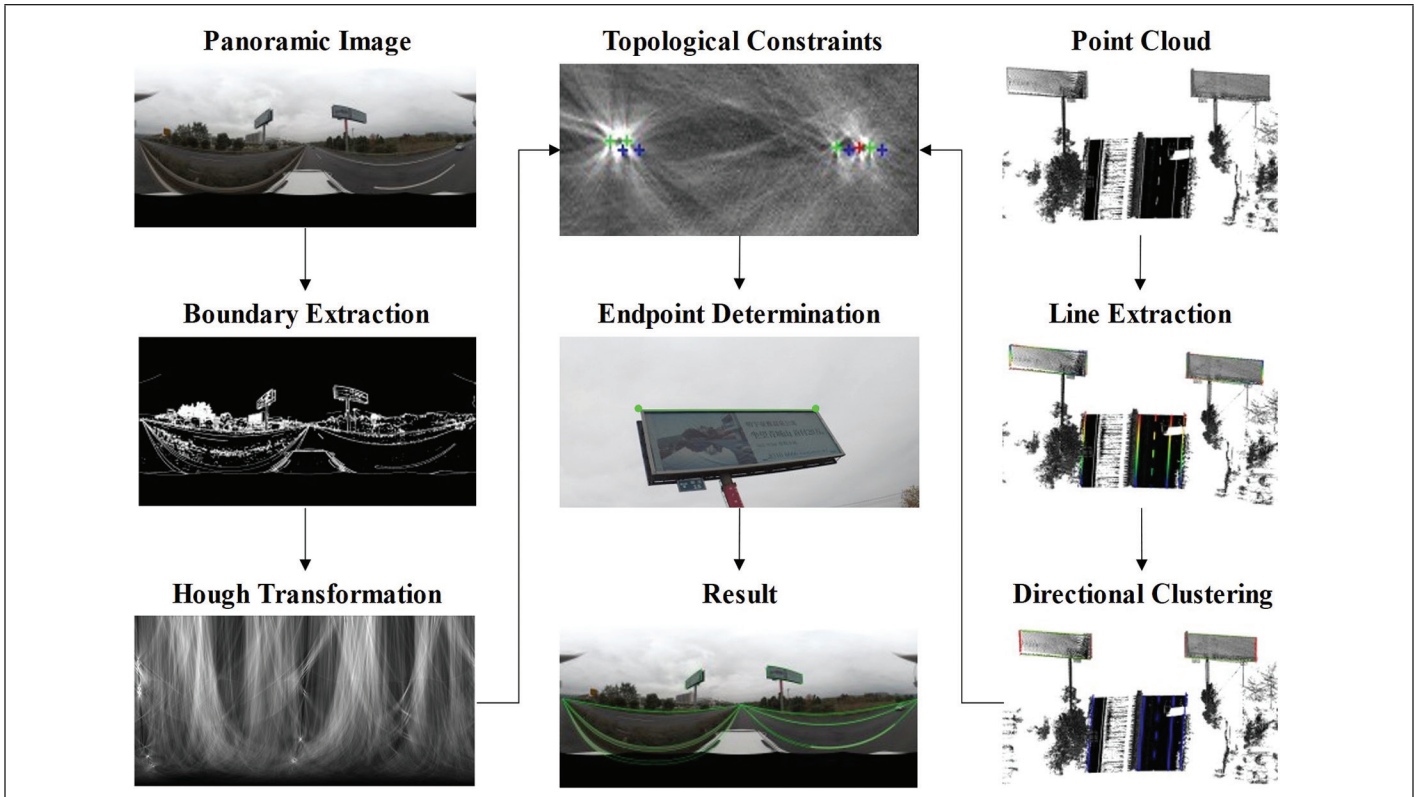

Figure 2. The overall workflow of the proposed approaches.

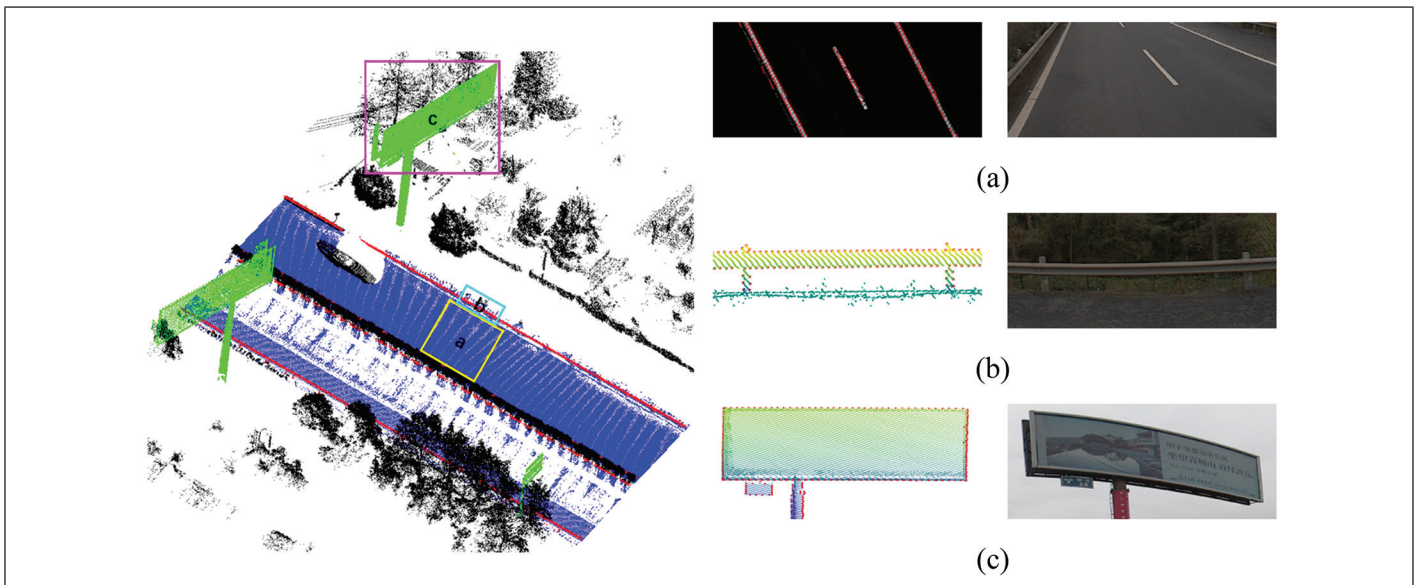

Figure 3. Line features from highway scene point clouds, including (a) landmarks, (b) guardrails, and (c) signboard edges.

relatively simple, and their linear features can be approximately classified into three categories: landmarks, guardrails, and signboard edges. As shown in Figure 3, the point clouds are first classified into different classes, such as ground, vegetation, and guardrails, based on the RandLA-Net (Hu *et al.* 2020). The line features are then extracted based on the classification results and clustered based on their orientations.

The landmarks belong to the ground points and are separated based on their significant intensity features, as shown in Figure 3a. Then, a density-based clustering algorithm is used to group the landmark points. Because the ground points are close to horizontal, the alpha-shape algorithm can easily extract their boundaries, and the line features are then extracted and fitted based on the 2D RANSAC. An approximate road direction can be determined from the landmarks, and the points from the guardrails are clustered and projected onto the vertical plane parallel to the estimated road direction. The interior line features are then extracted using the same methods used for the landmarks. Regarding the signboard, because it belongs to the same plane, we can directly track the boundary within the plane and then easily fit the edge lines. Once the initial line segments are extracted, further examination is conducted to optimize the detection results. Line segments with similar orientations are grouped and forced to be parallel, vertical, or collinear. Some prior constraints are also considered based on the highway design standard, such as the width of the landmarks and signboard.

Spherical Lines from Panoramic Images

For panoramic images, the spherical straight lines often appear as curved lines because of the projection mode, and traditional line detection methods such as LSD will fail, disassembling the curved lines into broken pieces. In this section, we first analyze the projection relationship between panoramic images and 3D lines. Then, the 3D line features on the panoramic image are extracted using the HT, which maps the curved boundary of the strip target on the image to the local extremes in the Hough space.

Spherical Straight Line Model

As shown in Figure 4, the panoramic image is a decomposition of a sphere surface. Its horizontal axis is the longitude, ranging from 0 to 2π, and the vertical axis is the latitude, ranging from $-\pi/2$ to $\pi/2$. As a result, the image width is always twice the image height. Because the panoramic image obeys the rule of center projection, the camera center O, point B and its formation b are always collinear. Suppose that S is the plane determined by the spherical straight line L_0 and camera center O; then, the projection line of L_0 on the panoramic image will be the intersection of the image sphere and plane S (the red line). As such, to generate the parameter space for all projection lines in the image sphere, we only need to find all possible planes passing through point O (the Great Circles such as S). Based on this consideration, two parameters are used to describe the projection lines: the first is the angle between S and the horizontal plane, which is denoted φ in Figure 4, and is in the range of $[0, \pi/2]$; the other is the orientation of S, which is denoted θ in Figure 4, representing the azimuth of the radius OA, and is in the range of $[0, \pi]$. These two parameters are also used in the HT-based line feature regression.

Once the plane S is determined by φ and θ, the corresponding function for the curve line is also determined. To better describe a random point on the spherical curve line, we introduce the angle α between OA and OB in Figure 4c. Based on the spatial geometric relations, we obtain:

$$\begin{cases} \tan(\theta - \theta_0 + \pi/2) = \cot\alpha \cos\varphi_0 \\ \sin\varphi = \cos\alpha \sin\varphi_0 \end{cases} \quad (\alpha \neq 0) \tag{2}$$

where φ_0 and θ_0 is the particular angles related to A (the projection of O on line L_0), and φ and θ indicate the particular angles related to B (arbitrary point on line L_0). Thus, the line segments can be easily represented by two α values under plane S.

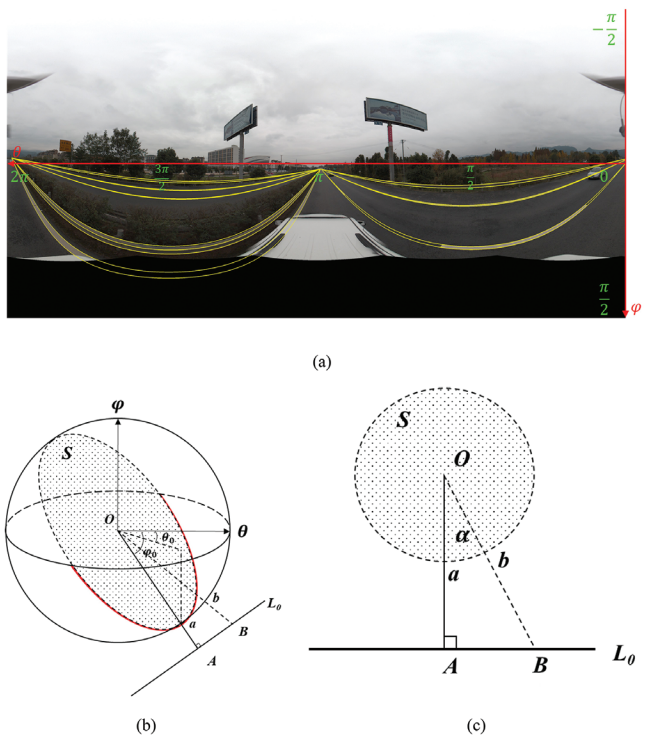

Figure 4. Schematic diagram of the Spherical Straight Line model of the panoramic camera. (a) The coordinate system of the panoramic image, where $\theta \in (0,\pi)$,$\varphi \in ((-\pi/2,\pi/2)$. (b) The projection of a spherical straight line to the panoramic imaging surface based on the central projection, where Point O is the camera center, line L_0 is a spherical straight line, and the curved red line is its projection on the imaging surface. (c) The cross-section decided by line L_0 and point O, where point A is the pedal and B is another random point in Line L_0, and a and b are the corresponding subpoint.

Spherical Hough Transform

We use the two angles φ and θ in the above section to create the 2D Hough space. Just like traditional HT, the regression of the projection lines for the panoramic images is based on the voting of single edge pixels. The workflow is as follows.

(a) The image edges are first extracted based on the Canny algorithm (Canny, 1986).
(b) For each edge pixel on the sphere surface, a certain number of circular cross-sections that pass through the pixel and camera center point are selected. For each cross-section, the φ and θ values are calculated and accumulate to the Hough parameter space.
(c) The target plane S is generated based on the extreme points in the Hough space.
(d) The line segments on the panoramic images are extracted based on plane S and the nearby edge pixels.

As shown in Figure 5, let point $A(\varphi_0, \theta_0)$ be the coordinate of the selected edge pixel on the unit sphere surface (radius equal to 1); then, the voting term of point A in the Hough space will be the parameters of all the big circles that pass through point O and point A, i.e., the blue circle with the parameter of (φ_i, θ_i). It can be seen that the φ_i values should range from φ_0 to $\pi/2$, and the θ_i value can be calculated based on the big sphere circle determined by φ_i, point A and point O.:

$$\theta_i = -\text{atan2}(\cos\beta\cos\varphi_i, \pm\sin\beta) + \theta_0 + \pi/2 \quad \varphi_i \in (\varphi_0, \pi/2) \tag{3}$$

where $\beta = \text{acos}(\sin\varphi_0/\sin\varphi_i)$. As such, when voting for the pixel in Hough space, we only need to gradually change the φ_i and then calculate the corresponding voting terms (φ_i,θ_i). For each edge pixel, we can obtain a curve line in the Hough space, i.e., the lines for point A, B, C, and D in Figure 5. Because those points belong to the same red projection line, the lines will intersect at the same point, which is the extreme point to be calculated, i.e., $(\pi/2, \pi/8)$ for the red line in Figure 5.

Line Segment Extraction

An example of the HT results is shown in Figure 6, in which each spherical straight line in the panoramic image corresponds to a local extremum point in the Hough space. In the section "Spherical Straight Line Model", we provided the function of curved lines in the sphere surface, but it is not convenient to extract the detailed curved line segments. According to the characteristics of the sphere projection, the curved projection line will become straight only when the φ value of the line is equal to $\pi/2$. Considering this, we can convert the curved line into a straight line by rotating the sphere surface, and we select a square buffer when extracting the line segments in the panoramic image. The edge pixels are considered here, and the far-most pixels near the line are projected to calculate the line endpoints.

Line Matching Within the Hough Space

Once the line features are successfully extracted from both sides, the task for line feature matching is to search for nearby extreme points within the Hough space. For the highway scenes, the difficulties concern the long parallel lines that are close to each other, i.e., the two sides of the landmarks, because their parameters are similar. In addition, long line segments may be divided into several pieces for the feature extraction procedure. Therefore, the parallel and collinear relationships are taken into consideration to improve the matching results and correct broken or missing pieces.

Pre-Matching with Local Topological Constraints

As shown in Figure 7, for a set of parallel 3D lines, i.e. L_1, L_2, and L_3, we can get the corresponding projection circles, whose lowest points

are marked as A_1, A_2, and A_3. Similar to Figure 4, we can get that OA_i is perpendicular to L_i (i = 1, 2, 3). As a result, L_i will be always perpendicular to the face determined by OA_1, OA_2, OA_3. This indicates that the three radius OA_1, OA_2, OA_3 are coplanar, and all the points A_1, A_2, and A_3 will form a circle perpendicular to the lines; this applies to the circles in the Hough space. Similar to the extraction of line segments in the panoramic image, we can rotate the sphere surface and put all of the vertical feet on a straight line. In this way, the extreme points in the Hough space will be collinear, and the searching of matching pairs will be converted from 2D to 1D. When considering the installation errors, we only need to search a small region, and the line features from the image and lidar will have robust relative positions. The relative distance and the orientation are then used to find the pre-matching results.

Mismatch Detection with Gradient Image Voting

The integration map of the spherical straight line may show multiple peaks near the true value because of an error in image boundary extraction, which is difficult to distinguish with only the distance and direction constraints. In this work, we invert the pre-matching points to the gradient image and distinguish the mismatching points from the true matching points by integrating the spherical straight line on the gradient image. The point with the largest integration result is selected as the final matching point. Because of the imaging characteristics of

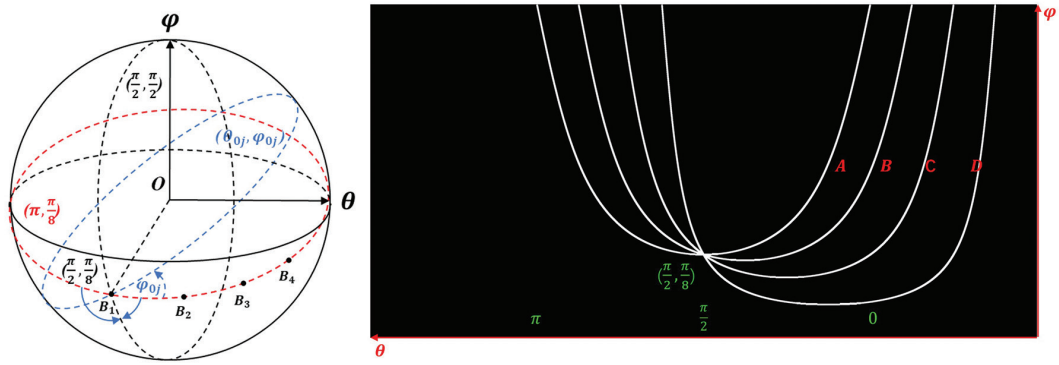

Figure 5. Example of points in the sphere panoramic surface and Hough space. (left) Point A is the lowest point for the red circle; B, C, and D are the other three random points on the circle. The blue circle passing through point O and A is randomly selected and its parameters in Hough space is (φ_i,θ_i). (right) the voting results of points A, B, C, and D in Hough space.

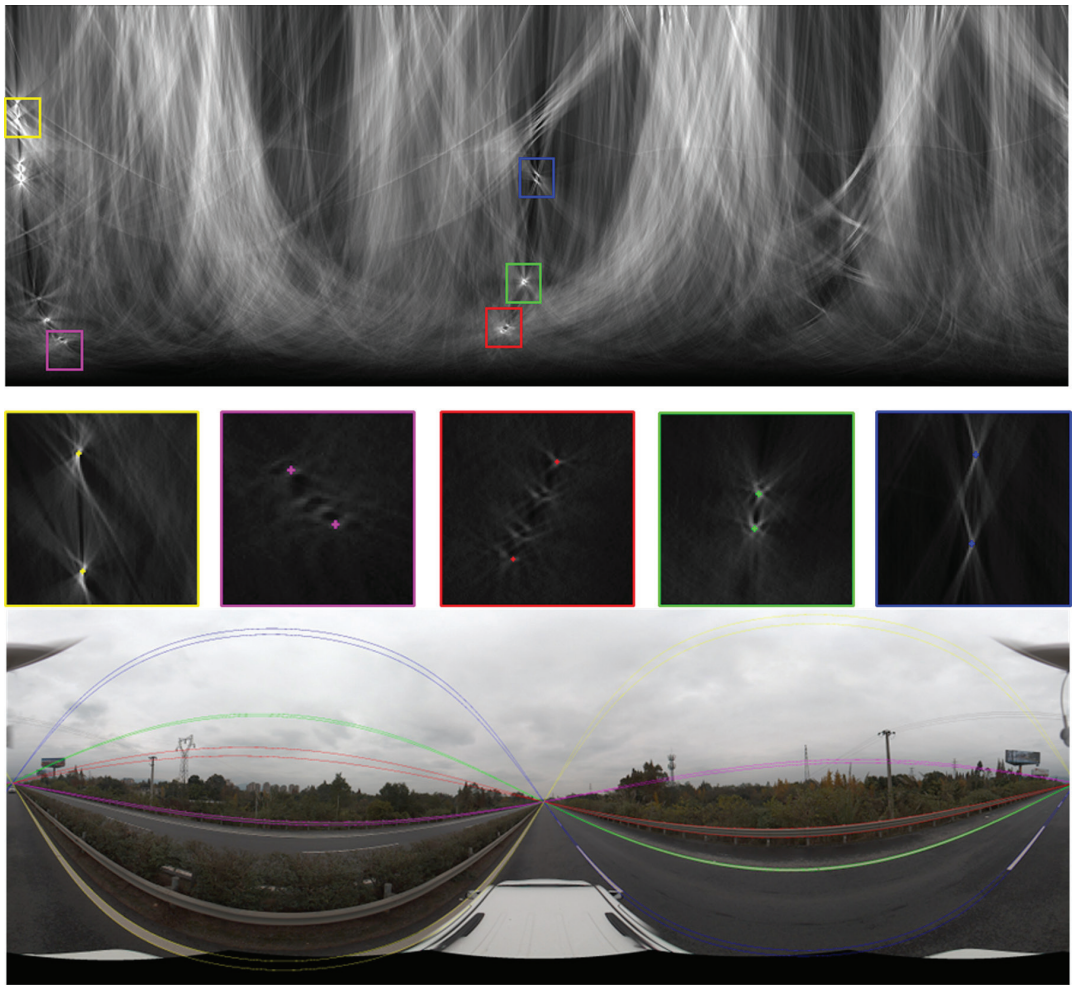

Figure 6. Correspondence between the extreme value point of the Hough space and the spherical straight line in a panoramic image.

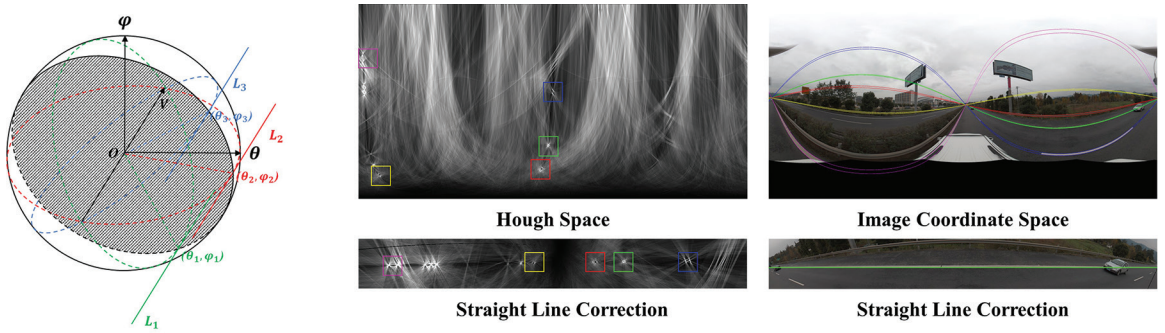

Figure 7. Parallel lines in the Hough space and the correction of straight lines.

Figure 8. View of the Du-Wen Expressway study area.

the panoramic camera, the curve has the highest resolution near the extreme value point. The gradient boundary is counted according to the point cloud as a priori knowledge to ensure that the statistical region has good differentiation. Vehicle occlusion on the highway also affects the nearby linear matching results; this occluded area must be eliminated by target recognition during matching.

Experiment and Results

This section experimentally evaluates the proposed methods, including the extraction of line features from both sides and their matching results in the highway scene.

Experiment Data

This study uses the point cloud and panoramic image data of the Du-Wen Expressway from Dujiangyan to Juyuan (Figure 8). The speed of the vehicle mobile scanning system is maintained at about 30 km/h. The panoramic images were acquired by a Ladybug5 camera with an acquisition interval of 5 s. In total, 1077 panoramic images were generated with a resolution of 4096 × 2048. The acquisition rate of the point cloud was 50 wHz, 100 scan lines per second. Ten randomly selected panoramic images from Duwen Expressway and the point cloud data within 30 m of the image areas were selected in the qualitative and quantitative evaluations.

Robustness Evaluation

In this section, we quantitatively evaluate the robustness of the proposed methods in extracting projection lines from panoramic images, including the influences of noise, occlusion, and road curvature.

Robustness to Noise and Occlusion

The HT-based projection line will be influenced by the noise within the edge pixels detected by the Canny algorithm. As shown in Figure 9, we select a projection line from a panoramic image (red line) and simulate noise to evaluate the line detection precision under various noise levels. Two types of noise are considered: (a) noise close to the line (white area) and (b) noise in other areas. We use the number of red pixels

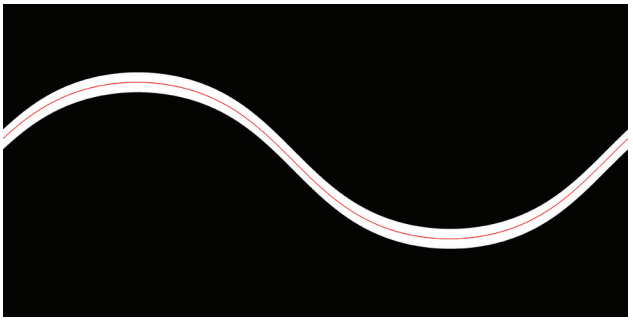

Figure 9. Introduction to the simulated data. Red line: the target projection line (ground truth). White/black areas: regions where random noise exists. The width of the white area is 5° either side of the red line.

(from ground truth) that are less than 2 pixels away from the fitted line as the precision metrics.

The quantitative results are presented in Figure 10. It can be seen that the noise in the black area has very little effect on the extraction results and that the accuracy of the extraction is mainly contributed by the nearby pixels. The robustness of the methods will greatly decrease when occlusion exists. Therefore, smoothing and occlusion detection should be performed during feature extraction to ensure the stability of feature extraction and matching.

Robustness to Road Curvature

According to the highway design standard from Chinese government, a minimum turning radius of 650 m is required. When curvature exists, the road features will no longer have straight lines, which will influence the precision of line extraction and matching. Because the level of influence is affected by the camera location, especially for the selection of the lanes and camera heights, we simulate the turning scene in Figure 11 and quantitatively evaluate the influence of the location precision.

The experimental results are shown in Table 1. The two-way four-lane roads are all tested, and elevations of the camera are changed from 0.5 m to 3.0 m, with a trail every 0.5 m. According to the experimental results, the fitting result can be guaranteed to be better than 0.0046 rad (about 3 pixels) when the height difference between the camera and the curve is controlled within 2.5 m. As shown in Figure 11, although the guardrail in the figure is not straight in space, it is perfectly described by a spherical straight model aligned on the boundary of the panoramic image because of the relatively gentle turn of the road. As such, our methods are robust for curved highway scenes under the turning radius constraints.

Curved Roads and Occlusion in a Real Scene

In Figure 12, two examples are provided for the curved road scene and the occlusion of a passing car. It can be seen that the proposed method can still successfully extract the target line segments, and the extreme point in the Hough space is rather clear. For the curved road scene in Figure 12a, because the turning radius of the highway is rather small, we can simply take the lines as straight, and the fitting results are acceptable. For the occluded part, we can still find a complete extraction result.

Evaluation and Comparison

In current methods, line features are detected mainly based on 2D line detection algorithms in the field of computer vision, such as LSD (Von Gioi *et al.* 2008) and Edge Drawing (ED)-line (Akinlar and Topal 2011; Topal and Akinlar 2012). For panoramic images, the curved lines are directly divided into pieces and are difficult to evaluate. Because the ultimate purpose of the line features is to register the image and the lidar point clouds, we use the line features from lidar, as before, when evaluating the image lines. Similar to the methods described in Figure 7, we rotate the image sphere to the given lidar line features, and thus the image line features can be straight within a small width. In this way, methods such as LSD can be used to extract the line features and can be compared with our methods.

We mainly consider the repetition rate of 2D–3D features and the completeness of the line features. The repetition rates refer to the

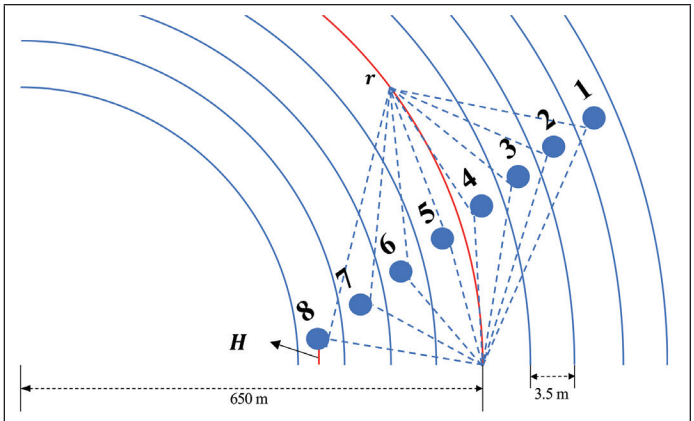

Figure 11. The simulated turning scene and the lanes. The lane width is assumed to be 3.5 m, the turning radius is set to 650 m, and the camera is located at the center of each lane.

Table. 1. Fitting accuracy of the Spherical Straight Line model to curves.

	Elevation Difference (m)					
	0.5	1	1.5	2	2.5	3
1	0.000693	0.001564	0.002827	0.002138	0.002037	0.004489
2	0.001170	0.001627	0.003118	0.002324	0.003024	0.004567
3	0.000801	0.001547	0.001491	0.003594	0.003685	0.002775
4	0.000652	0.001223	0.001648	0.002019	0.002423	0.005947
5	0.000940	0.001836	0.002705	0.003169	0.003964	0.004368
6	0.001598	0.002225	0.003236	0.002418	0.003204	0.005064
7	0.001019	0.001536	0.002267	0.002629	0.003722	0.005020
8	0.001310	0.003489	0.003280	0.003580	0.002941	0.002416

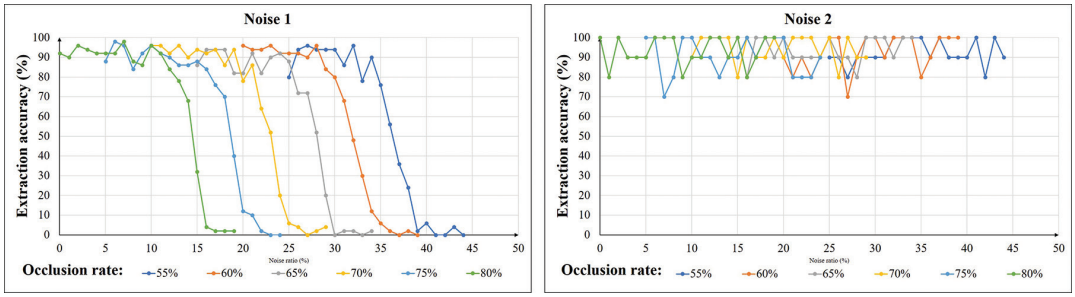

Figure 10. Influence of noise from the two regions. Noise ratio refers to the percentage of random noisy pixels in the corresponding areas and ranges from 10% to 40%. The occlusion ratio is the percentage of random pixels that are omitted while fitting the line. For a highway scene, the upper half of the image is often the sky without line features, and thus occlusion starts from 50%. (left) random noise in the white area; (right) random noise in the black area.

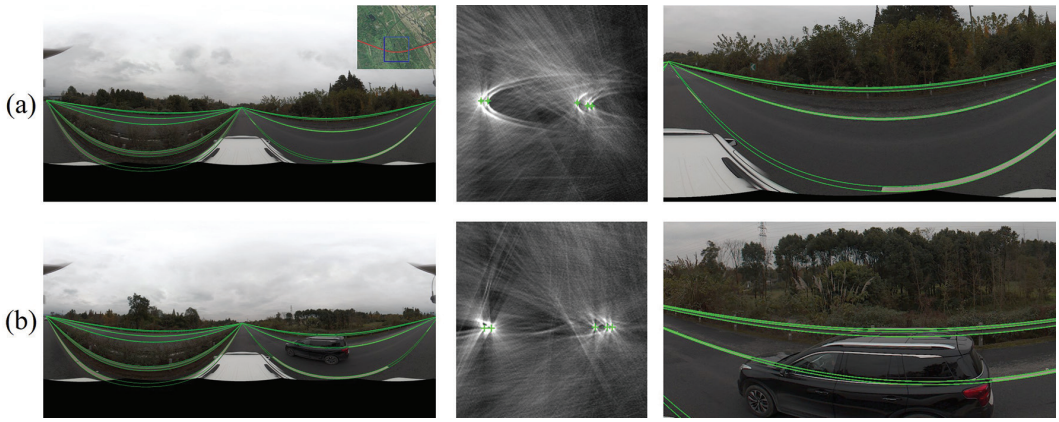

Figure 12. Spherical straight line extraction in (a) curved road and (b) occlusion scenes. (left) The input panoramic image, with the overall scene provided in the upper right corner of (a); (middle) the local Hough space and the identified local extreme points; (right) examples of extracted lines.

percentages of the line features that are matched with the lines from lidar. Higher repetition rates mean that the methods can more easily obtain matched line pairs and are less interrupted by noise and nearby features.

Five panoramic images are randomly selected from the test data, and the quantitative results are provided in Table 2. As seen, our methods can obtain more complete line features and thus have the lowest *PL* values. This is important for highway scenes because most line features are long and have small gaps, and broken pieces will easily lead to mismatching between line pairs. For other methods, although more line features are generated, there are many repeated or collinear line features inside even after the correction, which is also reflected by the *PL* values. The incomplete line features will also lead to low completeness metrics because of missing connections between those broken pieces.

The details of the line feature detection results are provided in Figure 13. It can be seen that the spherical line model can better describe the linear boundary affected by the panoramic image deformation and is significantly better than the traditional linear extraction algorithm in terms of feature repetition rate and target description integrity. Using current methods, because the surface of the spherical projection is non-Euclidian, it is difficult to effectively describe the projection lines in the spherical coordinate system with only the morphological characteristics.

Table 2. 2D–3D feature repetition rate for line extraction.

Image ID	GT	ED-Line			Hough			LSD			Our Method		
		EL	PL	com(%)	EL	PL	com(%)	EL	PL	com(%)	EL	PL	com(%)
337	18	14	4.1	27.3	16	9.5	48.8	17	7.2	54.4	12	1	96.7
383	30	22	3.9	27.1	25	9.7	52.6	28	7.8	63.0	20	1	97.8
554	12	10	3.7	31.5	11	8.2	41.8	12	6.7	50.2	12	1	96.9
837	12	11	3.9	32.1	10	10.3	42.1	12	8.1	50.1	12	1	96.6
940	16	13	4.3	27.6	12	8.7	48.3	14	6.9	56.7	12	1	97.7
sum	88	70	3.98	29.12	74	9.28	46.72	83	7.34	54.88	68	1	97.14

Note: GT = the line number for ground truth; ED-line = Edge Drawing-line; Line Segment Detector (LSD); EL = the extracted lines longer than 50 pixels; PL = the average number of lines for each GT line; Com is the pixel-level completeness of the detected lines.

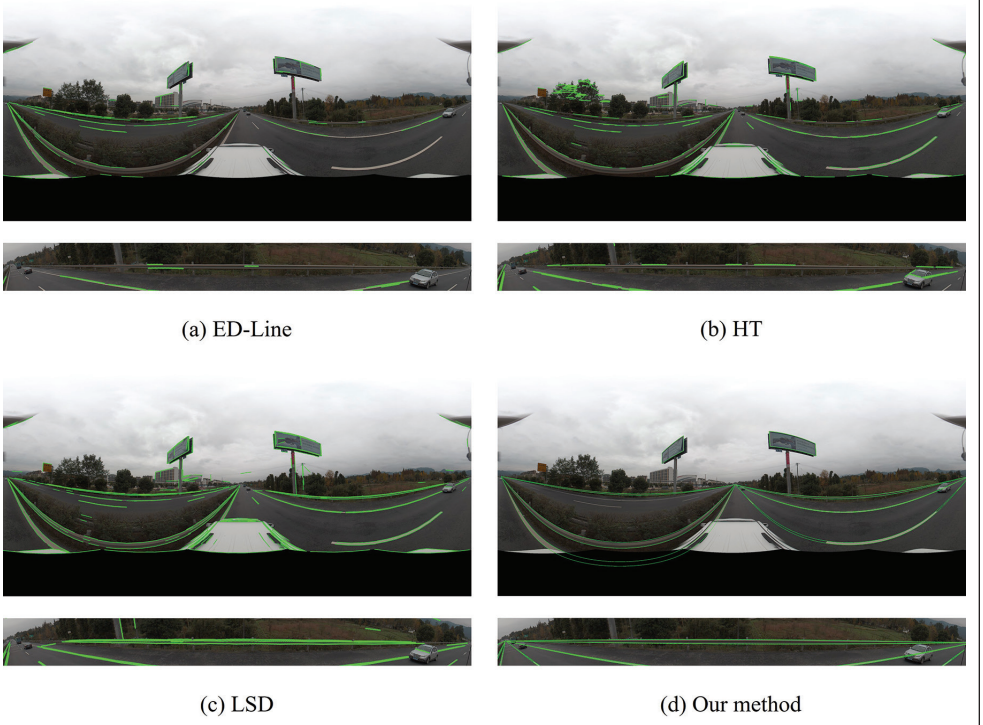

Figure 13. Comparison of line detection results and local details. ED-line = HT = Hough transform; LSD = Line Segment Detector.

Evaluation of Line Matching Results

This section analyzes the precision of matched line pairs between lidar point clouds and panoramic images. The ground truth is manually selected by considering the main line features in the highway scenes, as described in the section "Line Segments from Point Clouds". For the compared methods, because many long line features are divided into broken pieces, we take the 1:*N* pairs (one lidar line corresponding to *N* image lines) to be one *TP*; otherwise, they will have very low scores. Even in such a situation, our results still outperform the comparison methods in Table 3. Our methods show a particular advantage for the *FP* scores, which indicates that our methods are more robust to random noise. For the *FN* metrics, our results are mainly influenced by the fact that the line features from lidar are not very clear because of occlusion, noise, and low point density. The comparison methods only require a short piece to make *TP* pairs, whereas we are looking for overall matching results.

Discussion

Since current panoramic images are synthesized from multiple-lens cameras, another possible solution for the long-strip line features detection is to extract them from a single view and merge them into the panoramic image surface (Zhu 2019). In Figure 14, some trials are proposed and compared to our results. The Lines from a single view are extracted based on the LSD algorithm. Due to the stitching errors, obvious bias can be noticed for lines from different views, which makes it difficult to merge the collinear lines. Since there are some repeated parts between adjacent cameras, redundant line features are extracted. Meanwhile, the spurious or unstable line features will bring troubles to the follow-up line matching approaches. As a whole, our line features can be more complete compared to existing methods.

Conclusion

To address the difficulties of describing and matching long striped targets in highway scenes, this paper derives a rigorous spherical straight line model for panoramic images based on coplanar conditions and designs a straight line extraction and matching strategy based on the spherical Hough transform. Experimental results demonstrate that the proposed method can accurately describe the boundaries of long strip targets on the panoramic image and has high 2D–3D repeatability for long straight targets. The proposed model also shows advantages for registering between panoramic images and 3D lidar point clouds. Future work will apply the proposed methods to city or street scenes.

Acknowledgments

This study was partly supported by the National Natural Science Foundation of China (Projects No: 42230102, 41901408, 42071355),

as well as the Project Supported by the Open Fund of Key Laboratory of Urban Land Resources Monitoring and Simulation, Ministry of Natural Resources (Projects No: KF-2021-06-033).

Table 3. Point cloud and panoramic image line matching process.

		ED-Line				Hough				LSD				Our Method			
ID	GT	TP	FN	FP	Cor	TP	FN	FP	Cor	TP	FN	FP	Cor	TP	FN	FP	Cor
337	16	10	4	2	63	10	2	4	63	13	1	2	81	12	4	0	75
383	24	17	5	2	71	18	4	2	75	21	2	1	88	20	4	0	83
554	12	8	2	2	67	8	1	3	67	9	0	3	75	12	0	0	100
837	12	7	1	4	58	7	2	3	58	8	0	4	67	12	0	0	100
940	16	9	3	4	56	9	4	3	56	10	2	4	63	12	4	0	75

Note: *ID* = the index of the random selected image; *GT* = the number of matched line pairs in the reference; ED-line = HT = Hough transform; LSD = Line Segment Detector; *TP* = the true positive line pairs in both *GT* and the results; *FN* = the number of missing line pairs; *FP* = the number of spurious line pairs; *Cor* = the correctness in percentages, equal to *TP/GT*. Lines longer than 50 pixels are evaluated, and for the comparison methods, a *TP* is marked as longer if at least one line segment from the broken pieces is successfully matched.

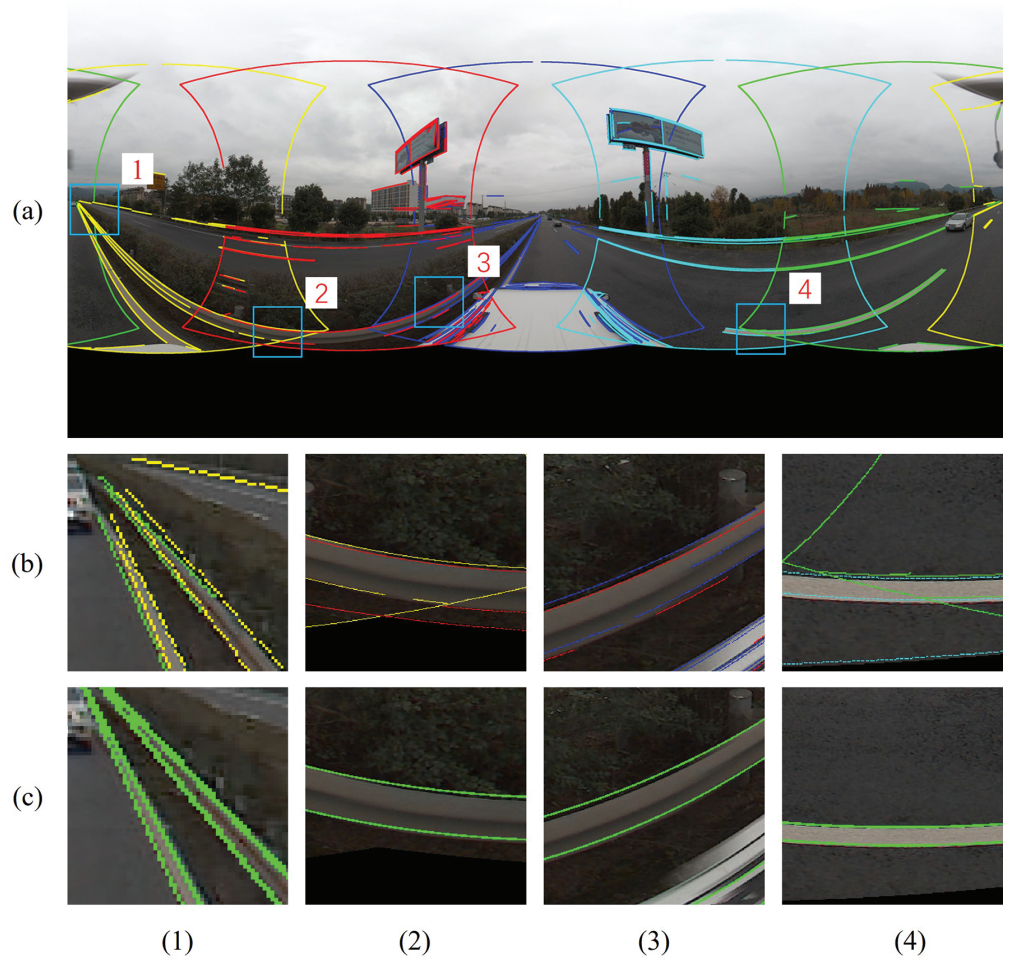

Figure 14. Compare of line detection results from single view. (a) Merge of LSD lines from different views, each a single color; (b) and (c) are the enlarged local details in the four selected regions, in which (b) is the lines from single view and (c) is our results.

References

Aggarwal, N. and W. C. Karl. 2006. Line detection in images through regularized Hough transform. *IEEE Transactions on Image Processing* 15(3):582–591.

Ahmad, T., P. Campr, M. Čadik and G. Bebis. 2017. Comparison of semantic segmentation approaches for horizon/sky line detection. Pages 4436–4443 in *Proceedings 2017 International Joint Conference on Neural Networks (IJCNN)*. https://doi.org/10.1109/IJCNN.2017.7966418.

Akca, D. 2010. Co-registration of surfaces by 3D least squares matching. *Photogrammetric Engineering and Remote Sensing* 76(3):307–318.

Akinlar, C. and C. Topal. 2011. Edlines: Real-time line segment detection by edge drawing (ed). Pages 2837–2840 in *Proceedings 2011 18th IEEE International Conference on Image Processing*. https://doi.org/10.1109/ICIP.2011.6116138.

Alba, M., L. Barazzetti, M. Scaioni and F. Remondino. 2011. Automatic registration of multiple laser scans using panoramic RGB and intensity images. *Proceedings of the ISPRS Workshop Laser Scanning*. https://doi.org/10.5194/isprsarchives-XXXVIII-5-W12-49-2011.

Awrangjeb, M. 2016. Using point cloud data to identify, trace, and regularize the outlines of buildings. *International Journal of Remote Sensing* 37(3):551–579.

Ballard, D. H. 1981. Generalizing the Hough transform to detect arbitrary shapes. *Pattern Recognition* 13(2):111–122.

Bao, S., W. Shi, P. Chen, H. Xiang and Y. Yu. 2022. A systematic mapping framework for backpack mobile mapping system in common monotonous environments. *Measurement* 197:111243.

Bazazian, D., J. R. Casas and J. Ruiz-Hidalgo. 2015. Fast and robust edge extraction in unorganized point clouds. Pages 1–8 in *Proceedings 2015 International Conference on Digital Image Computing: Techniques and Applications (DICTA)*. https://doi.org/10.1109/DICTA.2015.7371262.

Canny, J. 1986. A computational approach to edge detection. *IEEE Transactions on Pattern Analysis and Machine Intelligence* 6:679–698.

Choi, S., T. Kim and W. Yu. 2009. *Performance Evaluation of RANSAC Family*. London, UK: BMVC.

Cui, T., S. Ji, J. Shan, J. Gong and K. Liu. 2016. Line-based registration of panoramic images and LiDAR point clouds for mobile mapping. *Sensors* 17(1):70.

Duda, R. O. and P. E. Hart. 1972. Use of the Hough transformation to detect lines and curves in pictures. *Communications of the ACM* 15(1):11–15.

Elberink, S. O. and G. Vosselman. 2009. Building reconstruction by target based graph matching on incomplete laser data: analysis and limitations. *Sensors* 9(8):6101–6118. https://doi.org/10.3390/s90806101.

Fernandes, L. A. and M. M. Oliveira. 2008. Real-time line detection through an improved Hough transform voting scheme. *Pattern Recognition* 41(1):299–314.

Hackel, T., J. D. Wegner and K. Schindler. 2016. Contour detection in unstructured 3D point clouds. Pages 1610–1618 in *Proceedings of the IEEE Conference on Computer Vision and Pattern Recognition*. https://doi.org/10.1109/CVPR.2016.178.

Hu, Q., B. Yang, L. Xie, S. Rosa and A. Markham. 2020. RandLA-Net: Efficient semantic segmentation of large-scale point clouds. In *2020 IEEE/CVF Conference on Computer Vision and Pattern Recognition (CVPR)*.

https://doi.org/10.48550/arXiv.1911.11236.

Huang, K., Y. Wang, Z. Zhou, T. Ding, S. Gao and Y. Ma. 2018. Learning to parse wireframes in images of man-made environments. In *Proceedings of the IEEE Conference on Computer Vision and Pattern Recognition*.

https://doi.org/10.48550/arXiv.2007.07527.

Hussnain, Z., S. O. Elberink and G. Vosselman. 2021. Enhanced trajectory estimation of mobile laser scanners using aerial images. *ISPRS Journal of Photogrammetry and Remote Sensing* 173: 66–78.

Law, H. and J. Deng. 2018. Cornernet: Detecting objects as paired keypoints. *Proceedings of the European Conference on Computer Vision (ECCV)*.

https://doi.org/10.48550/arXiv.1808.01244.

Lee, J.-T., H.-U. Kim, C. Lee and C.-S. Kim. 2017. Semantic line detection and its applications. Pages 3249–3257 in *Proceedings of the IEEE International Conference on Computer Vision*. https://doi.org/10.1109/ICCV.2017.350.

Li, H., H. Yu, J. Wang, W. Yang, L. Yu and S. Scherer. 2021. ULSD: Unified line segment detection across pinhole, fisheye, and spherical cameras. *ISPRS Journal of Photogrammetry and Remote Sensing* 178:187–202.

Li, J., B. Yang, C. Chen, R. Huang, Z. Dong and W. Xiao. 2018. Automatic registration of panoramic image sequence and mobile laser scanning data using semantic features. *ISPRS Journal of Photogrammetry and Remote Sensing* 136:41–57.

Lin, Y., C. Wang, B. Chen, D. Zai and J. Li. 2017. Facet segmentation-based line segment extraction for large-scale point clouds. *IEEE Transactions on Geoscience and Remote Sensing* 55(9):4839–4854.

Lin, Y., C. Wang, J. Cheng, B. Chen, F. Jia, Z. Chen and J. Li. 2015. Line segment extraction for large scale unorganized point clouds. *ISPRS Journal of Photogrammetry and Remote Sensing* 102:172–183.

Lowe, D. G. 2004. Distinctive image features from scale-invariant keypoints. *International Journal of Computer Vision* 60(2):91–110.

Lu, X., Y. Liu and K. Li. 2019. Fast 3D line segment detection from unorganized point cloud. *arXiv preprint arXiv:1901.02532*.

Miled, M., B. Soheilian, E. Habets and B. Vallet. 2016. Hybrid online mobile laser scanner calibration through image alignment by mutual information. *ISPRS Annals of the Photogrammetry, Remote Sensing and Spatial Information Sciences* 3:25.

Morel, J.-M. and G. Yu. 2009. ASIFT: A new framework for fully affine invariant image comparison. *SIAM Journal on Imaging Sciences* 2(2):438–469.

Puente, I., H. González-Jorge, J. Martínez-Sánchez and P. Arias. 2013. Review of mobile mapping and surveying technologies. *Measurement* 46(7):2127–2145.

Rahmdel, P., R. A. Comley, D. Shi and S. McElduff. 2015. A review of Hough transform and line segment detection approaches. Pages in 411–418 *Proceedings of the 10th International Conference on Computer Vision Theory and Applications - Volume 2: VISAPP*. https://doi.org/10.5220/0005268904110418.

Ren, H., R. Liu, F. Wang and J. Yang. 2022. Automatic extraction method of urban road curb boundary from vehicle-borne laser point clouds. *KSCE Journal of Civil Engineering* 1–10.

Sampath, A. and J. Shan. 2007. Building boundary tracing and regularization from airborne LiDAR point clouds. *Photogrammetric Engineering & Remote Sensing* 73(7):805–812.

Topal, C. and C. Akinlar. 2012. Edge drawing: A combined real-time edge and segment detector. *Journal of Visual Communication and Image Representation* 23(6):862–872.

Von Gioi, R. G., J. Jakubowicz, J.-M. Morel and G. Randall. 2008. LSD: A fast line segment detector with a false detection control. *IEEE Transactions on Pattern Analysis and Machine Intelligence* 32(4):722–732.

Wang, R., F. P. Ferrie and J. Macfarlane. 2012. Automatic registration of mobile LiDAR and spherical panoramas. Pages 33–40in *Proceedings 2012 IEEE Computer Society Conference on Computer Vision and Pattern Recognition Workshops*. https://doi.org/10.1109/CVPRW.2012.6238912.

Weber, C., S. Hahmann and H. Hagen. 2010. Sharp feature detection in point clouds. Pages 175–186 in *Proceedings 2010 Shape Modeling International Conference*. https://doi.org/10.1109/SMI.2010.32.

Xu, B., W. Jiang and L. Li. 2017. HRTT: A hierarchical roof topology structure for robust building roof reconstruction from point clouds. *Remote Sensing* 9(4):354. <https://www.mdpi.com/2072-4292/9/4/354>

Xu, B., W. Jiang, J. Shan, J. Zhang and L. Lelin. 2016. Investigation on the weighted RANSAC approaches for building roof plane segmentation from LiDAR point clouds. *Remote Sensing* 8(1):5.

Yang, B. and C. Chen. 2015. Automatic registration of UAV-borne sequent images and LiDAR data. *ISPRS Journal of Photogrammetry and Remote Sensing* 101:262–274.

You, R. J. and B. C. Lin. 2011. Building feature extraction from airborne lidar data based on tensor voting algorithm. *Photogrammetry Engineering and Remote Sensing* 77(12):1221–1231.

Yuan, Q., L. Yao, Z. Xu and H. Liu. 2022. Survey of expressway infrastructure based on vehicle-borne mobile mapping system. *International Conference on Intelligent Traffic Systems and Smart City (ITSSC 2021)*. https://doi.org/10.1117/12.2627889.

Zhang, Y. and Z. Cui. 2022. Registration of terrestrial LiDAR and panoramic imagery using the spherical epipolar line and spherical absolute orientation model. *IEEE Sensors Journal* 22(13):13088–13098.

Zhang, Z., Z. Li, N. Bi, J. Zheng, J. Wang, K. Huang, W. Luo, Y. Xu and S. Gao. 2019. PPGNet: Learning point-pair graph for line segment detection. Pages 7098–7107 in *Proceedings of the IEEE/CVF Conference on Computer Vision and Pattern Recognition*. https://doi.org/10.1109/CVPR.2019.00727.

Zhang, Z., Y. Zhang, J. Zhang and H. Zhang. 2008. Photogrammetric modeling of linear features with generalized point photogrammetry. *Photogrammetric Engineering & Remote Sensing* 74(9):1119–1127.

Zhou, Y., H. Qi and Y. Ma. 2019. End-to-end wireframe parsing. Pages 962–971 in *Proceedings of the IEEE/CVF International Conference on Computer Vision*. https://doi.org/10.1109/ICCV.2019.00105.

Zhu, N. 2019. Simulation analysis of spherical panoramic mosaic. *Signal Processing* 158:190–200.

Blind and Robust Watermarking Algorithm for Remote Sensing Images Resistant to Geometric Attacks

Na Ren, Xinyan Pang, Changqing Zhu, Shuitao Guo, and Ying Xiong

Abstract

To address the problem of weak robustness against geometric attacks of remote sensing images' digital watermarking, a robust watermarking algorithm based on template watermarking is proposed in this paper, which improves the robustness of digital watermarking against geometric attacks by constructing stable geometric attack invariant features. In this paper, the Discrete Fourier Transform domain template watermark is used as the invariant feature against geometric attacks, and the embedding of the cyclic watermark is used to improve the watermark robustness for recovering the watermark synchronization relationship. To achieve blind extraction of the watermark, a parameter extraction method based on noise extraction is designed. The experimental results demonstrate that the proposed method can effectively improve the robustness of digital watermarking of remote sensing images against geometric attacks. Meanwhile, it can also resist common image processing attacks and compound attacks.

Introduction

Remote sensing images are basic strategic resources, which play an important role in land use, environmental protection, military operations, and other fields (Amhar *et al.* 2022). While the development of network technology makes the transmission of remote sensing image data more convenient, it makes the security protection problems such as piracy, leakage, and illegal dissemination of remote sensing image data become increasingly serious (Zhou *et al.* 2015; Singh *et al.* 2021; Yu *et al.* 2019). The emergence of digital watermarking technology provides a powerful solution for remote sensing image data security protection (Zhu 2017; Zhou *et al.* 2020).

Robustness is an important indicator of the capability of digital watermarking algorithms, which means the ability of watermarking algorithms to detect the correct watermark information after being attacked. Currently, scholars have conducted extensive research on how to improve the robustness of digital watermarking algorithms, which has significantly improved the robustness of remote sensing images in terms of filtering, noise, compression, and other attacks (Fu *et al.* 2016; Wang *et al.* 2017). However, for geometric attacks, such as rotating and scaling the remote sensing image to change the image size and position, etc., the watermark information cannot be extracted because it is very easy to destroy the watermark synchronization relationship, i.e., the consistent relationship between the embedding and extracting position in the image. And most of the current remote sensing image data watermarking algorithms are unable to resist geometric attacks. Therefore, how to improve the robustness against geometric attacks has become a key issue in digital watermarking algorithms to security for protect remote sensing image.

Existing watermarking algorithms aiming to resist geometric attacks for remote sensing image data are mainly divided into two categories. The first category is non-blind watermarking algorithms, which require the original data or other relevant information to correct the watermarked image after being attacked. It can recover the watermark synchronization relationship for watermark information detection. For example, Tarhouni *et al.* (2020) store the speeded up robust features (SURF) feature point information of the original image, and during the watermark extraction process, the SURF feature points in the attacked image are extracted, and then matched with the origin points to correct the watermark synchronization relationship. This type of method can accurately recover the relative position relationship between image watermark embedding and extraction by matching the set of image feature points. However, the original information such as image (Lee *et al.* 2020; Mohammed *et al.* 2020), feature points (Li and Zhang 2020), and transform domain coefficients (Dappuri *et al.* 2020) needs to be saved in advance and will be matched from the database with the information to be detected. Therefore, the non-blind watermarking algorithm increases the cost of storage and retrieval, which is not conducive to practical applications.

The second type of algorithm is blind watermarking algorithm, which does not require the original data or other relevant information for watermark detection. It usually maintains the watermark synchronization relationship by mining the invariant features, and uses the relative position relationship, which between the invariant features and the watermark embedding position, to achieve watermark embedding and detection. For example, Hsu and Chen (2016) constructed circular local invariant regions near the filtered feature points and embedded the watermark in the local invariant regions. Due to the invariant property of the feature points, the local invariant feature regions can be recovered by finding the requirement feature points in the attacked images, thus recovering the watermark synchronization relationship. This type of algorithm does not require the original data in the watermark detection process, and the watermark synchronization relationship is recovered based on the invariant information, such as feature points (Wang *et al.* 2011; Keskinarkaus *et al.* 2012), template watermark (Fang *et al.* 2021; Sun *et al.* 2021), and other invariant information, to resist geometric attacks. However, remote sensing images are feature-rich and watermark embedding is based on filtered features which are vulnerable to geometric attack and cannot resist arbitrary geometric attacks.

The above analysis shows that the non-blind watermarking algorithm increases the storage and retrieval costs, because it requires the participation of raw data or other relevant information for watermark detection. The blind watermarking algorithm achieves blind detection by finding the invariant feature to recover the synchronization after the geometric attacks. During the attacks, however, these filtered features

Key Laboratory of Virtual Geographic Environment, Nanjing Normal University, Ministry of Education, Nanjing 210023, China; State Key Laboratory Cultivation Base of Geographical En-vironment Evolution, Jiangsu Province, Nanjing 210023, China; Jiangsu Center for Collaborative Innovation in Geographical Information Resource Development and Application, Nanjing 210023, China (capoziom@163.com).

Contributed by Zhenfeng Shao, August 29, 2022 (sent for review October 25, 2022; reviewed by Yanyan Xu, Md Enamul Huq).

Photogrammetric Engineering & Remote Sensing
Vol. 89, No. 5, May 2023, pp. 321–332.
0099-1112/22/321–332
© 2023 American Society for Photogrammetry and Remote Sensing
doi: 10.14358/PERS.22-00114R2

are susceptible to large geometric attacks, and thus cannot resist arbitrary geometric attacks. So, in the current research of watermarking algorithms for remote sensing images to resist geometric attacks, finding stably invariant feature that can resist geometric attacks has become a difficult problem.

Therefore, we propose a blind watermarking algorithm based on template watermarking to resist geometric attacks. We design a specific template watermark based on the properties of the discrete Fourier transform (DFT) transform domain to construct stable feature invariants against geometric attacks. The watermark information can be extracted without the involvement of the original data. This method is a blind watermarking algorithm, which can improve the robustness against geometric attacks and is important for the security protection of remote sensing images.

The rest of the paper is organized as follows, the second section is the preliminaries, the next section is the proposed method, next is the experiments section, followed by the section that is the discussion, and finally the last section is the conclusion of the paper.

Preliminaries

DFT Transform

The discrete Fourier transform is the conversion from spatial domain signal to frequency domain signal. For a two-dimensional image $f(x, y)$ of size $M \times N$, the discrete Fourier transform $F(u, v)$ is defined by Equation 1, denoted as $F(f(x, y))$ following:

$$F(u,v)=\sum_{x=0}^{M-1}\sum_{y=0}^{N-1}f(x,y)\exp\left[-j2\pi\left(\frac{ux}{M}+\frac{vy}{N}\right)\right],(u=0,1,2,\cdots,M-1;v=0,1,2,\cdots,N-1) \quad (1)$$

Rotation Invariant Property of DFT

If $F(f(x, y))$ denoted as Fourier transform, then rewriting DFT to the polar form and rotating the image, as shown in the following equations, the two-dimensional Fourier transform is rotation invariant, so when the image is rotated by an angle, the Fourier transform of the rotated image will also be rotated by the corresponding angle. With this property, a cyclic watermark is constructed. By template matching of the watermark in the Fourier transform domain after rotation, we can extract the rotation attack angle.

$$f(x, y) = f(r, \theta), (x = r\cos\theta, y = r\sin\theta) \quad (2)$$

$$F(u, v) = F(\omega, \varphi), (u = \omega\cos\varphi, v = \omega\sin\varphi) \quad (3)$$

$$f(r, \theta + \theta_0) = F(\omega, \varphi + \varphi_0) \quad (4)$$

Scaling Inverse Property of DFT

If $F(f(x, y))$ denoted as Fourier transform, the two-dimensional Fourier transform is scaling inverse, as shown in the following equation, when the image is scaled up and down in the spatial domain, the frequency domain is transformed inverse of the corresponding scaling multiplier. With this property, the peak of the frequency amplitude at the radius of the cyclic watermark is taken as the invariant feature. By extracting the radius where the cyclic watermark is located at the Fourier transform domain of the scaled image, we can extract the scaling attack factor.

$$f(ax,by)=\frac{1}{|ab|}F(u,v) \quad (5)$$

Translation Invariant Property of DFT

If $F(f(x, y))$ denoted as Fourier transform, the two-dimensional Fourier transform has translation invariance, in the Equation 6 and Equation 7. The translation invariance reflects that when $f(x, y)$ in the spatial domain perform a shift, only a phase shift occurs in the frequency domain, which does not affect the magnitude. With this property, the watermark embedded in the frequency domain does not change, after translation and cropping.

$$f(x-x_0,y-y_0)=F(u,v)\exp\left[-j2\pi\left(\frac{ux_0}{M}+\frac{vy_0}{N}\right)\right] \quad (6)$$

$$\left|F(u,v)\exp\left[-j2\pi\left(\frac{ux_0}{M}+\frac{vy_0}{N}\right)\right]\right|=\left|F(u,v)\right| \quad (7)$$

Materials and Methods

To improve the problem of poor robustness of watermarking against geometric attacks, DFT domain template watermark is used as an invariant feature against geometric attacks. We design embedding position rules of separation in the frequency domain for adjacent chunked watermark information and propose a parameter extraction method based on noise extraction and template matching to accurately extract watermark information.

Cyclic Watermark Embedding

The content of the embedded watermark is a sequence of 0 and 1 generated by the copyright information and the key, and the length of the watermark in each chunk is l. So, the watermark is $s = \{S_j | S_j \in \{0,1\}, i = 0, \ldots, l-1\}$.

After chunking the image, the DFT transform is applied to the chunks separately. The watermark embedding is performed by directly replacing the DFT magnitude coefficients, and the watermark is embedded on the circle with r as the radius, Meanwhile, due to the symmetry of the DFT, a watermark bit should be embedded in two locations symmetrical to the center of the magnitude map. Therefore, the location of the watermark embedding is shown as the following equation. N is the image width after chunking, R is the embedding area determined by the index of the chunk, r is the radius where the watermark is embedded, i is the embedded watermark bit, L is the length of the watermark embedding on one side, around( ) function is used to round, floor( ) is used to round down, mod( ) is used to calculate the remainder.

$$\begin{cases} x_i = \dfrac{n}{2} + \text{around}\left(r\cos\left(R\cdot 90^\circ + \text{floor}\left(\dfrac{i}{L}\right)\cdot 180^\circ + 2\text{mod}(i,L)\dfrac{\pi}{180^\circ}\right)\right) \\ y_i = \dfrac{n}{2} + \text{around}\left(r\sin\left(R\cdot 90^\circ + \text{floor}\left(\dfrac{i}{L}\right)\cdot 180^\circ + 2\text{mod}(i,L)\dfrac{\pi}{180^\circ}\right)\right) \end{cases} \quad (8)$$

The replacement rule of the watermark in the embedding process is shown in the Equation 9, when the watermark S_i is 1, the replacement is the watermark intensity k_1, otherwise the original frequency-domain coefficients $M_{x,y}$, and after embedding the coefficients is shown in Figure 1. The embedding intensity is exaggerated for display purposes. The two 1/4 double circular shape watermarks embedded are referred to standard watermark ring in this paper (Figure 1).

$$M_{x,y}=\begin{cases} k_1, S_i = 1 \\ M_{x,y}, S_i = 0 \end{cases} \quad (9)$$

Embedding Position Rule

When the watermark information to be embedded is large scale, if all the watermark contents are embedded in the DFT magnitude of the whole image, then each segment of the image will be affected by all the watermark information and the imperceptibility of the watermark will be greatly reduced at this time. Therefore, in order to avoid reducing the imperceptibility of the watermark and increase the watermark capacity of the image, this paper chunks the image firstly and then embeds part of the watermark in the chunks, respectively.

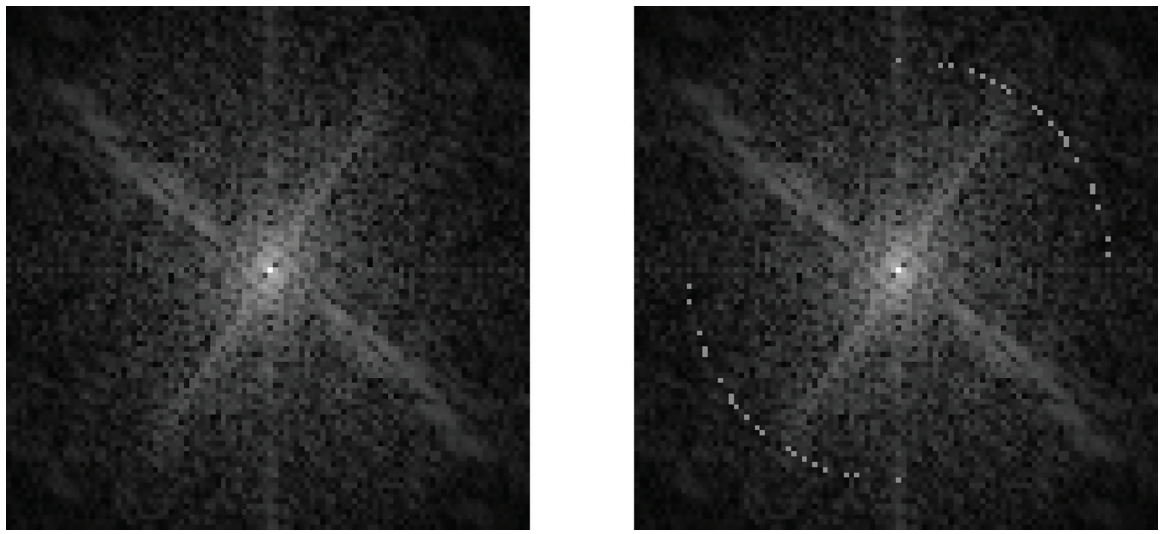

(a) (b)

Figure 1. Discrete Fourier transform (DFT) amplitude graph before and after embedding watermark. (a) The original frequency-domain coefficients. (b) The coefficients after watermark embedding.

In order to avoid the confusion of watermark contents from adjacent chunks during extraction, this paper separates the embedding regions of adjacent chunks and constructs the embedding position selection method in the frequency domain (Equation 10). (*I, J*) refers to the index of the chunk on the horizontal and vertical directions. If the position *R* refers to 0, the watermark information will be embedded in the first and the third quadrant, otherwise it will be embedded in the second and the fourth quadrant, as shown in the Figure 2. The actual image embedding watermarking process according to the chunking is shown in Figure 3. When the extracted watermark content is from two chunks, the extracted watermark is the whole circle in the four quadrants instead of the standard watermark ring.

$$R = \begin{cases} 0, mod(I+J,2) = 0 \\ 1, mod(I+J,2) = 1 \end{cases} \tag{10}$$

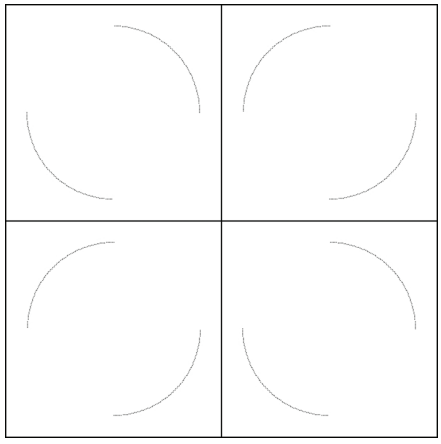

Figure 2. Diagram of watermark embedding position.

Unlike Su *et al.* (2020) and Pramila *et al.* (2008), whom embed the template watermark and copyright watermark information in different transform domains of the image, the copyright watermark is combined with the template watermark and the watermark information is embedded in a single transform domain only. The actual content of the watermark is the copyright watermark information, and the embedding position of it reflects the position of the template watermark.

After embedding the watermark, the chunked image is transformed to the spatial domain by the inverse Fourier transform. To ensure the values of the image are in the valid range and avoid the block effect, the coefficients in the frequency domain need to be normalized.

Watermark Detection Based on Template Matching and Noise Extraction

Due to the properties of the DFT transform, the DFT frequency coefficients rotate with the rotation of the image and scale inverse accordingly with its scaling. The embedded watermark exists in the form of noise, so the extraction needs to extract the noise coefficients from the chunked image. In order to avoid extracting information from multiple chunks with different watermark contents, the watermark ring pattern in the noise coefficient needs to be judged to ensure that it is standard.

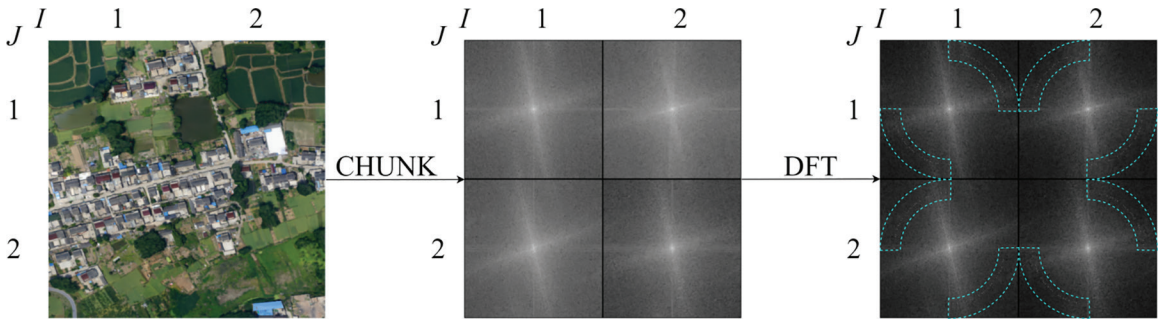

Figure 3. Flowchart of actual image embedded in watermark in chunks.

Furthermore, the statistical features of the noise coefficients are used to extract the coefficients of the original image rotation and scaling (Figure 4).

Peak Position Extraction from Global Image Noise

The magnitude diagram of the chunks and of the location where the chunks are located when embedded are shown in the Figure 5. Before extraction, the transformed image needs to be pre-processed. By removing the major coefficients from the DFT amplitude map, the watermark information presented in the spectrogram in the form of noise can be brought out. The preprocessing method is an improvement of the preprocessing process of Chen *et al.* (2020). Following the steps below, the preprocessing results are shown in Figure 6. For ease of observation, the preprocessed example image watermark is embedded on two radii with radii 120 and 130.

1. After image chunking, the image color space is converted from RGB to YUV, and the luminance component Y is converted to the Fourier domain (Figure 6a).
2. The main components were obtained by OSTU thresholding method classification (Figure 6c), and corrupted twice by convolution kernels c1 and c2 respectively (Figure 6d).
3. The noise components are extracted by Wiener filtering and transformed to the Fourier domain (Figure 6e).
4. The main coefficients obtained in the third step are used as a mask to act in the DFT domain of the obtained noise component (Figure 6f). After using the OSTU thresholding method, the watermark information is separated from the background (Figure 6g). Here the colors are inverted for display purposes.

The sub-blocks are transformed to coordinates separately (Figure 6h). In order to avoid the insignificance of watermark coefficients in individual sub-blocks, the noise on each radius of each sub-block is accumulated (Figure7a). The watermark coefficients in the form of noise will show significant peaks in the radius where they are located. And the extracted noise sums on different radius will be weakened as the radius increases. The first-order derivatives of the cumulative results are calculated (Figure 7b), and the radius is obtained by extracting the

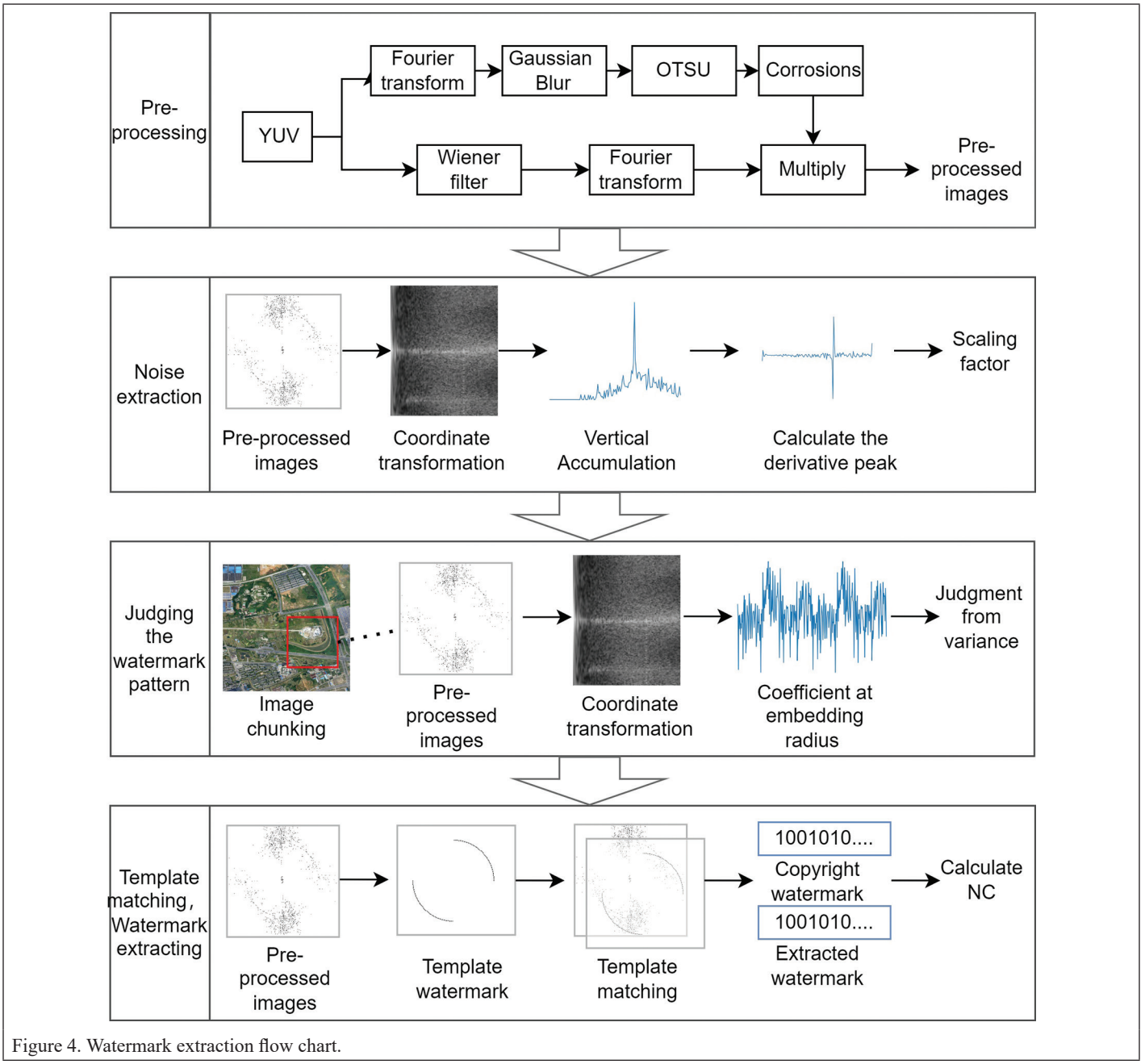

Figure 4. Watermark extraction flow chart.

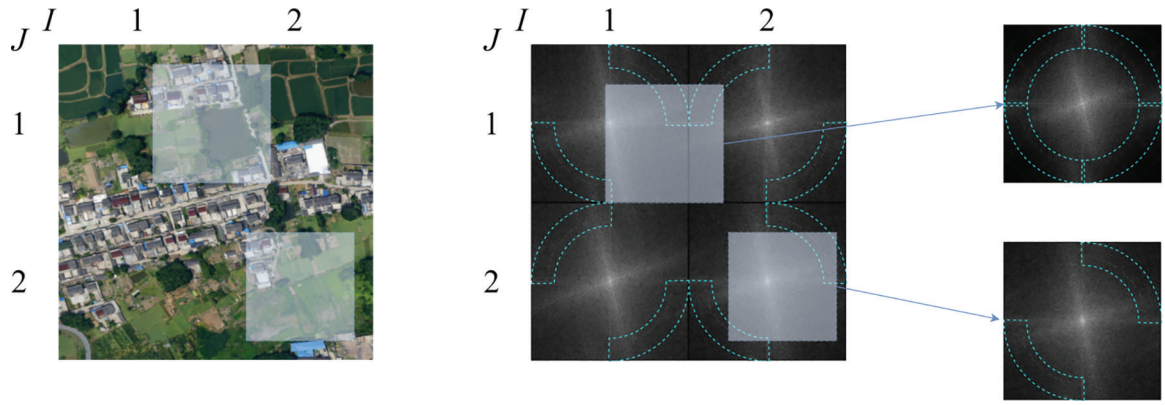

Figure 5. The magnitude diagram of the chunks and of the location where the chunks are located when embedded.

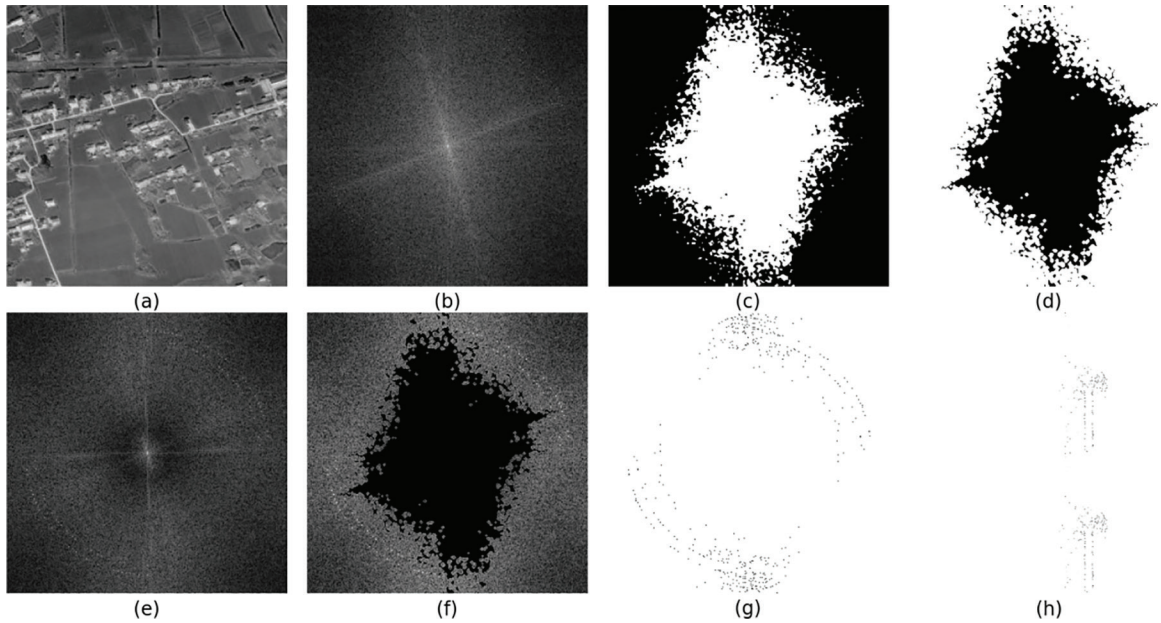

Figure 6. Preprocessing results: (a) Component Y after converted to YUV. (b) The Fourier domain of the luminance component. (c) The main components were obtained by OSTU thresholding method. (d) Corrupted twice by convolution kernels. (e). The noise components are extracted by Wiener filtering. (f) The main coefficients obtained by mask. (g) Separating watermark information by OSTU. (h) Transformed to coordinates.

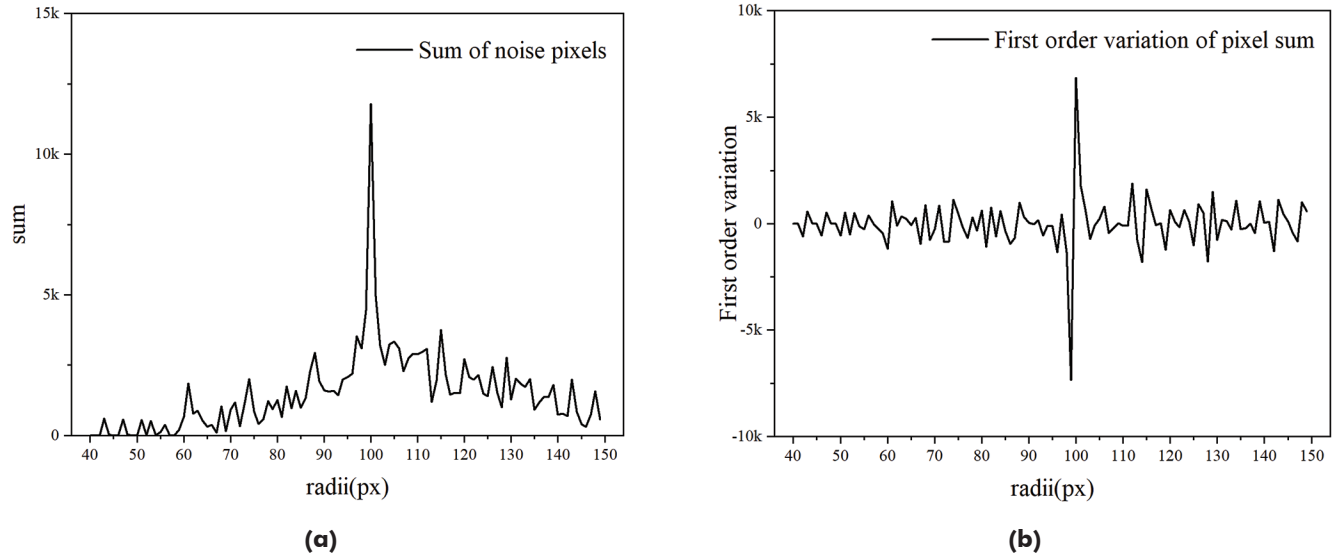

Figure 7. Noise pixel sums and first-order derivatives isolated on different radii. (a) Sum of the noise on each radius. (b) The first-order derivatives of the cumulative results.

peak that meets more than three times the size of the standard deviation of the first-order derivative mean.

Image Rotation Coefficient Extraction Based on Template Matching

Since the image may undergo an unknown directional transformation, thanks to the rotationally invariant property of the DFT, after the image has been rotated, the coefficients of the DFT are also rotated by the corresponding angle. And the starting point of the watermark sequence embedding in the image is estimated by template matching.

When the extracted chunks are a single subset of chunks on the image at the time of embedding, it will behave as a standard watermark ring in the frequency. Since the watermarks embedded in adjacent chunks are separated from each other by position and complementary to each other as circles, it will otherwise present a complete circle in the frequency domain. Therefore, by judging whether the circle of the watermark ring in the frequency domain is complete or not, we are able to indirectly synchronize the frequency domain chunking method and thus extract the actual watermark.

The determination of the watermark's shape requires the radius where the watermark circle is located, so this step needs to be placed after the noise peak extraction step. Based on the scaling factor information obtained in the previous step, scaling is performed to the specified size. Since the pixels embedded in the watermark are of high amplitude, the amplitude of the radius where they are located fluctuates significantly due to the watermark, and its variance is larger. The standard watermark ring is less than the complete ring with only half of the watermark exists, and its variance is smaller. By calculating the variance of both, the sub-block with a variance less than k2 is taken as the standard watermark ring for further extraction.

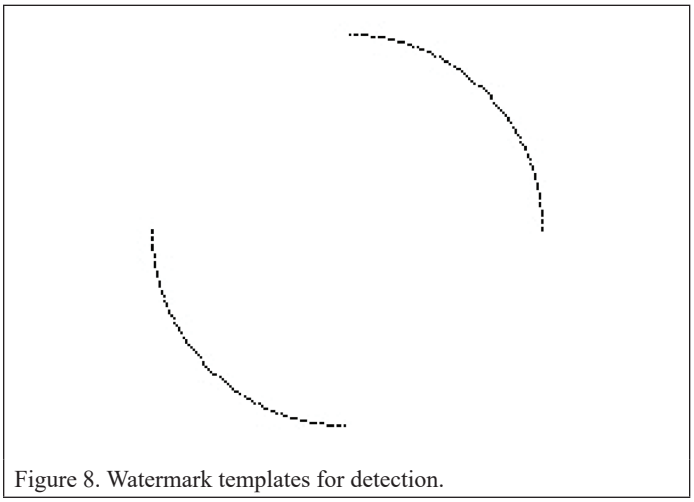

Figure 8. Watermark templates for detection.

To extract the image rotation angle, a watermark template with all 1s in the watermark sequence is designed (Figure 8). To calculate the normalized squared difference and get the best matching result within 180 degrees, the template is rotated by any angle with the separated watermarked image.

For the extraction of the actual watermark sequence, we need to combine the watermark embedding position formula and the obtained rotation angle. The actual watermark sequence can be obtained within 3 × 3 neighborhood area, by summing up the values. The watermark value will be 1 if the sum is greater than or equal to 255, otherwise will be 0.

Results

Experimental Data and Evaluation Indexes

Eight images of size 2000 × 2000 selected from 16-level tile maps are acquired from 91weitu (https://www.91wemap.com/) (Figure 9). The watermark sequence in one chunk is a binary sequence of length 45 generated by the key.

The imperceptibility of the watermark is calculated by the peak signal-to-noise ratio (PSNR), which is used to measure the similarity between the output image and the original image.

The peak signal-to-noise ratio evaluates the image quality after processing, by calculating the ratio between the maximum value of the image signal and the background noise. The calculation formula is shown in the following equation. is the maximum value of the image color depth, and the maximum value of the image with 8-bit color depth is 255. The larger the PSNR value, the smaller the distortion the original image, and the better the image quality. When the PSNR >= 40 dB, the image quality is considered excellent.

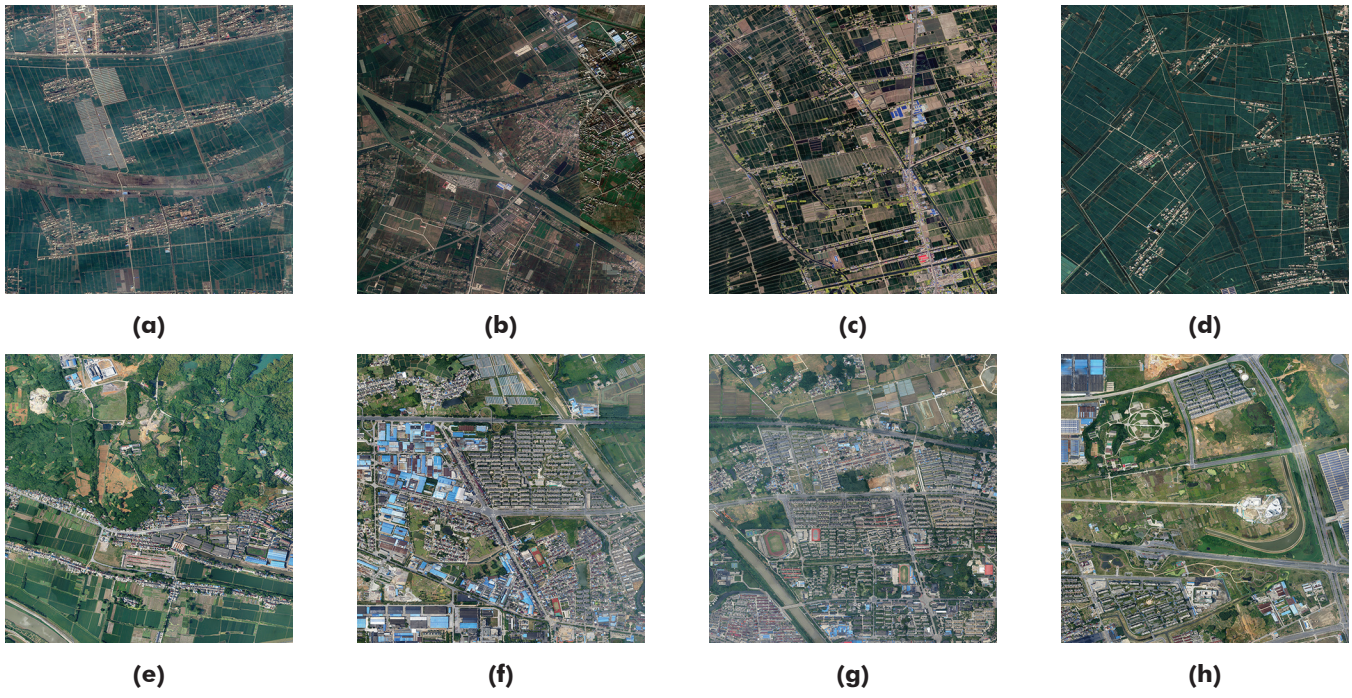

Figure 9. Example of experimental images.

$$PSNR = 10 \cdot \log_{10}\left(\frac{MAX^2}{MSE}\right) \tag{11}$$

$$MSE = \frac{1}{mn}\sum_{i=0}^{m-1}\sum_{j=0}^{n-1}\left[I(i,j) - K(i,j)\right]^2 \tag{12}$$

The extracted watermark is measured with the copyright watermark y by normalized correlation (NC). And the higher the NC, the higher the correct rate of watermark extraction. The NC and bit error rate definition is shown in the Equation 13.

$$NC = \frac{cov(x,y)}{\sigma_x \cdot \sigma_y} \tag{13}$$

$cov(x, y)$ is the covariance of the two sequences, and σ_x, σ_y is the product of the standard deviation of the two sequences.

Imperceptibility

The imperceptibility of the watermark is determined by many factors, such as the radius of the embedded watermark in the amplitude coefficient, the strength of the watermark embedding, and the percentage of '1' in the watermark sequence. In order to discuss the difference in the influence of each factor on the imperceptibility of the watermark, the following experiments are designed.

In order to study the effect of embedding strength and quantity of watermark on PNSR, watermark sequences containing different amounts of '1' were embedded with different strengths, and the PSNR after embedding watermark was calculated separately (Figure 10a). The embedding intensity ranges from (100, 160) at an interval of 10, and the watermark sequences containing '1' amount vary between (18, 30) at an interval of 4. The embedding radius is controlled as 110 px.

In order to study the influence of the location and quantity of watermark embedding on the PSNR, the sequences with different percentages of '1' were embedded at different radii of the amplitude coefficient, and the PSNR after embedding the watermark was calculated separately (Figure 10b). The radius range is (60, 130) at an interval of 10 pixels, and the watermarked sequences containing "'1' amount vary between (18, 30) at an interval of 4. The control embedding intensity q is 120.

Figure 10a shows the PSNR of watermarked sequences with different amounts of '1' at different embedding strengths. The PSNR decreases with the increase of the number of '1' in general. Meanwhile, the stronger the embedding strength, the lower the PSNR of the image. Since the watermark sequence satisfies the characteristics of a pseudo-random sequence, the number 0 and 1 in the sequence is equal. When n is 22, the embedding strength of the watermark is determined as 120 and the PSNR of the image = 40.6 dB, which satisfies the imperceptibility requirement of the watermark.

Figure 10b shows that the PSNR after embedding different watermark sequences containing '1' amount on the embedding radius, embedding the watermark on different radii has a large impact on the PSNR of the image. The maximum impact on the PSNR can reach 3.4 when the same watermark sequence is embedded between 60–130 px radius. The overall decrease in PSNR with an increasing number in sequence 1. When n is 22, the embedding strength is 120, and the PSNR varies between 39.56–40.87 dB. Since the choice of the radius will also affect the robustness of the watermark at the same time, it will be made in the discussion section.

The watermark is embedded in the experimental image according to the parameters selected above. The origin and embedded images in a zoomed in view with theirs PSNR are showing as follows (Table 1). The PSNR after embedding meets the requirement of watermark imperceptibility, and the change of the image cannot be detected by human eye.

Robustness of Geometric Attacks

During image processing, geometric attacks are easy to destroy the synchronization relationship, thus invalidating the watermark. In order to verify the robustness of the algorithm for geometric attacks, three kinds of geometric attacks are selected for robustness experiments. The experimental images are cropped to 40%, 60%, and 80% of the original image size (Table 2). The experimental images are rotated at different angles in the range of [20°, 340°] with an interval of 20° (Table 3). The experimental images are scaled in the range of [60%, 150%] with an interval of 10% (Table 4).

To avoid the possibility of inferring the attack method from the black edges of the image edges, the image size used in the robustness comparison test is twice the size of the original. When rotating, the center of the image is used as the rotation center, and the image is cropped to the original size from the rotation center outward after rotation. When scaling, the center of the image is used as the scaling center and the image is cropped to the original size from the center of the image outward after scaling.

Also, in order to verify the differences in robustness between the algorithm in this paper and other blind watermarking algorithms, a comparison experiment with the algorithms of Pereira and Pun (2000)

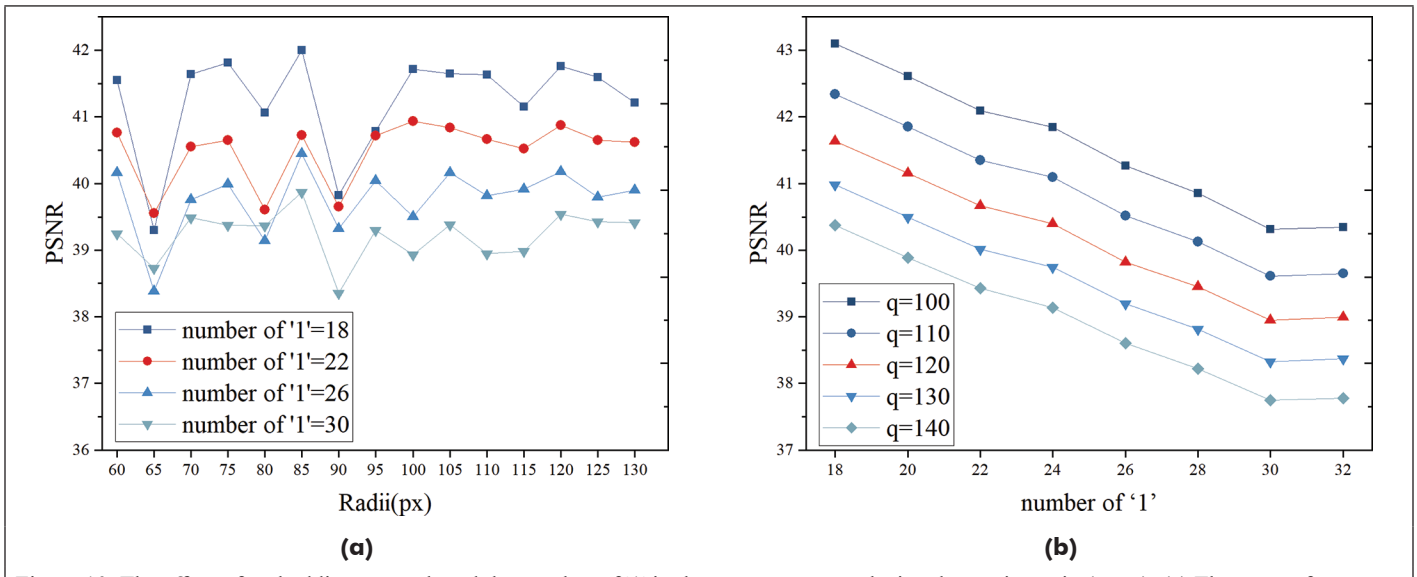

Figure 10. The effect of embedding strength and the number of '1' in the sequence on peak signal-to-noise ratio (PSNR). (a) The PSNR of watermarked sequences with different amounts of '1' at different embedding strengths. (b) The PSNR after embedding different watermark sequences containing '1' amount on the embedding radius.

and Niu *et al.* (2020) is designed in this paper. Pereira and Pun (2000) detect the scaling and rotation changes of the image by embedding a ray-type template watermark. Niu *et al.* (2020) take the feature points in the image as invariant information and embed the watermark information in the invariant feature region. The mean NC between the proposed method and the comparison algorithm under geometric attack are also shown in the table.

The watermark NC is still greater than 0.70 even at 40% crop level. In the cropping attack, only at least one complete chunk of the cropped image is required for watermark extraction. It can be considered that the algorithm in this paper is robust to the cropping attack. The robustness of this paper's algorithm against cropping attacks is comparable to that of Niu *et al.* (2020). Compared with Pereira and Pun's (2000) algorithm. Even if the robustness against cropping attacks is slightly lower, the algorithm still can resist large-scale cropping attacks.

Different overall magnitudes of images will have different effects on the watermark at the selected radius, making the accuracy of the extracted watermark in each image different. The accuracy of the watermark coefficients extracted from different rotation angles will produce small changes, but all experimental images still have watermark NC greater than 0.70 after rotation. It can be considered that the algorithm in this paper has strong robustness to rotational attacks at any angle. Compared with Pereira and Pun's (2000) algorithm, the algorithm in this paper is less stable in extracting the watermark information of the rotation attack, but it is still better than Pereira and Niu's algorithm in general.

The watermark NC changes within 0.05 for each image in the scaling range and the overall change is small. Even under the more serious

Table 1. The origin and embedded images in a zoomed-in view with the peak signal-to-noise ratio (PSNR).

A zoomed-in view of the original images				
A zoomed-in view of the watermarked images				
PSNR	39.9	40.38	40.66	40.65
	(a)	(b)	(c)	(d)
A zoomed in view of the original images				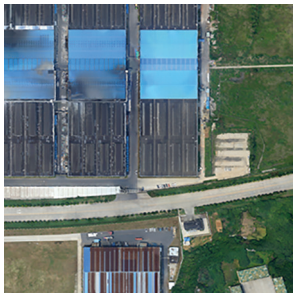
A zoomed in view of the watermarked images				
PSNR	39.47	40.59	40.33	40.49
	(e)	(f)	(g)	(h)

attacks of 150% scaling attack and 60% scaling attack, the NC is still greater than 0.95 and 0.70 at minimum. It can be considered that the algorithm in this paper is highly robust to scaling attacks in the range of 60%–150%. Since the embedding frequency range chosen by Pereira and Pun's (2000) cannot resist the scaling attack in a larger range, the robustness of this paper against the scaling attack is better.

However, since the proposed method is based on the DFT frequency domain embedding watermark, which is not invariant to affine transformation. The circular features of the watermark ring will change, and the watermark can no longer be extracted by extracting radius peaks and template matching, after affine transformation.

Robustness of Image Conventional Processing Attacks

In addition to geometric attacks, a qualified watermarking algorithm must be able to resist basic image conventional processing attacks, including noise, filtering, sharpening, etc. To verify the robustness of the algorithm, we choose different degrees of jpeg compression attack, Gaussian blur attack and Gaussian noise attack. JPEG Compression attack experiments include five different degrees of compression ratios of 50%, 60%, 70%, 80%, and 90%. Gaussian blur attack experiments are five different degrees of blur with a blur radius of 3 and a variance of 0.5–0.9 with an interval of 0.1. Gaussian noise is five different degrees of noise with a radius of 3 and a variance of 0.01–0.05 with an interval of 0.01 (Table 5). The mean NC between the proposed method and the comparison in the algorithm image under image conventional processing attacks are also shown in Table.

As shown in Table 5, the NC hardly changes under different degrees of Gaussian blurring attacks, and the extraction accuracy is high for all of them, which is very robust to Gaussian blurring attacks. Under the Gaussian noise attack, the NC of the watermarks do not change very significantly as the variance becomes larger, but the overall NC is all greater than 0.70. Under the compression attack, the watermark NC generally decrease as the compression increase, but even under 50% compression, the minimum NC is 0.75, which still has good accuracy. In summary, the algorithm can be very robust to any processing that does not affect the degree of image usage. For common image processing attacks, the algorithm in this paper is generally more robust compared to that of Pereira and Pun (2000). Although the proposed method is slightly weaker than the algorithm of Niu *et al.* (2020) in terms of Gaussian filtering attacks, it still behaves better than the algorithm of Niu *et al.* in general.

Robustness of Compound Attacks

To further verify the robustness of the algorithm under compound operation, experiments are conducted under the compound attack of noise attack and geometric attack and the compound attack of various geometric attacks. The experiments include image compression, blurring and noise attack experiments with different degrees after image rotation and scaling, as well as rotation and scaling compound attack experiments with large changes in the watermark synchronization relationship (Table 6, Table 7, Table 8). The mean NC between the algorithm in this paper and the comparison algorithm under the mixed attack are also shown in the following tables.

The extracted watermark NC varies under different rotation angles and decreases as the degree of image processing attack becomes stronger. However, the smallest watermark NC is still greater than 0.7 under the most severe compression, blurring, and noise attacks. It proves that the algorithm is robust to the compound attack of image rotation and image conventional attacks.

Table 2. Normalized correlation (NC) between the proposed method and the comparison algorithm of extracted watermarks at different cropping scales.

					MNC[1]		
Cropping Scale/%	Img(a)	Img(b)	Img(c)	Img(d)	Proposed	Niu *et al.* (2020)	Pereira and Pun (2000)
80	1	0.96	0.84	1	0.95	0.94	1
60	0.91	0.96	0.96	1	0.96	0.94	1
40	0.91	1	0.87	0.96	0.94	0.94	1

1. MNC refers to the mean normalized correlation, which is derived from the mean correlation coefficient of the experimental images.

Table 3. Normalized correlation (NC) between the proposed method and the comparison algorithm of extracted watermarks at different rotation angels.

					MNC[2]		
Rotation angle/°	Img(a)	Img(b)	Img(c)	Img(d)	Proposed	Niu *et al.* (2020)	Pereira and Pun (2000)
20	0.96	1	0.91	0.96	**0.96**[3]	0.91	0.84
40	0.8	0.87	0.8	0.87	0.84	0.92	0.89
60	0.87	0.96	0.91	0.96	**0.93**	0.91	0.84
80	0.92	0.96	0.87	0.96	**0.93**	0.90	0.87
100	0.83	1	0.96	1	**0.95**	0.94	0.84
120	0.83	0.96	0.91	0.96	**0.92**	0.91	0.89
140	0.91	1	0.96	1	**0.97**	0.92	0.87
160	1	0.87	0.76	0.87	0.88	0.93	0.84
180	0.96	1	0.96	0.96	0.94	0.94	1
200	0.96	1	0.91	0.96	**0.96**	0.91	0.84
220	0.84	0.84	0.8	0.87	0.84	0.92	0.87
240	0.87	0.96	0.91	0.96	**0.93**	0.91	0.82
260	0.92	0.96	0.87	0.96	**0.93**	0.90	0.89
280	0.83	1	0.96	0.96	**0.94**	0.94	0.84
300	0.92	0.96	0.91	0.96	**0.94**	0.91	0.89
320	1	1	1	1	**1.00**	0.92	0.89
340	0.83	0.87	0.8	0.87	0.84	0.93	0.84

2. MNC refers to the mean normalized correlation, which is derived from the mean correlation coefficient of the experimental images.
3. The bolded data indicate the specific values when the algorithm outperforms the comparison algorithm for the same attack.

Table 4. Normalized correlation (NC) between the proposed method and the comparison algorithm of extracted watermarks at different scaling ratios.

					MNC[4]		
Scaling ratio/%	Img(a)	Img(b)	Img(c)	Img(d)	Proposed	Niu *et al.* (2020)	Pereira and Pun (2000)
1.1	0.96	1	0.96	0.96	**0.97**[5]	0.93	0.73
1.2	0.96	1	0.96	0.96	**0.97**	0.93	0.71
1.3	0.96	1	0.91	0.96	**0.96**	0.90	0.71
1.4	0.96	1	0.96	0.96	**0.97**	0.93	0.76
1.5	0.96	1	0.96	0.96	**0.97**	0.85	0.71
0.9	0.96	1	1	0.96	**0.98**	0.89	0.71
0.8	0.91	1	0.96	0.96	**0.96**	0.89	0.76
0.7	0.96	1	0.96	0.96	**0.97**	0.81	0.71
0.6	0.96	1	0.79	0.96	**0.93**	0.80	0.52

4. MNC refers to the mean normalized correlation, which is derived from the mean correlation coefficient of the experimental images.
5. The bolded data indicate the specific values when the algorithm outperforms the comparison algorithm for the same attack.

The difficulty of watermark extraction is enhanced under the dual influence of rotation and image processing attacks. As the scaling range increases, the loss of image processing on the image increases, the watermark NC decreases, and the stability of the algorithm extraction decreases. However, the minimum watermark NC is still greater than 0.7 even under the scaling attack in the range of 0.8–1.2. Therefore, the algorithm also has strong robustness to the compound attack of image scaling and image conventional attack.

The NC varies with the rotation attack, and the smallest watermark NC is still greater than 0.87. Therefore, the algorithm is highly robust to the compound attack of geometric attacks.

Discussion

Selection and Generalization of Embedding Radius

The amplitude coefficients, at different radii in the DFT domain, have different change patterns after image attacks (Chen *et al.* 2008; Solanki *et al.* 2004; Dajun and Sun 2005). So, embedding watermarks at different radii will affect the robustness of the algorithm. Robustness is divided into robustness for geometric attacks and robustness for conventional image process attacks. The influence of radius on the robustness of geometric attacks is mainly reflected in the scaling attack. After scaling attacks, the watermarked circle will also scale in the magnitude map. However, their coefficients change differently at different locations when under conventional attack. In order to make the method resist, the scaling attack in a certain range and choose the radius range that has less influence on the geometric attack and image conventional process attack, the following experiments are designed in this paper.

The watermark NC embedded in different radii are detected under Gaussian blurring attacks with variances of 0.5, 0.7, and 0.9, Gaussian noise attacks with variances of 0.01, 0.03, and 0.05 and JPEG compression attacks with parameters of 60%, 80%, and 90%, respectively. The radii are chosen in the range of 60–130 px with 5 px interval (Figure 11).

Figure 11a shows the robustness of the watermark embedded at different radii to Gaussian blur attacks with variances of 0.5, 0.7, and 0.9. The NC at any radius is mostly above 0.9 overall when the variances are 0.5 and 0.7 and are greater than the threshold value of 0.75 when the variances are 0.9. The NC decreases significantly at radii greater than 125 px when the variances are 0.9. Therefore, the robustness to Gaussian blur attacks is better at radii of 60–120 px.

Figure 11b shows the robustness of the watermark embedded at different radii to Gaussian noise attacks with a variance of 0.01, 0.03, and 0.05. The NC are all above 0.8 when the radius is 65–130 px, and the NC

Table 5. The normalized correlation (NC) between the proposed method and the comparison algorithm under conventional image process attacks.

						MNC[6]		
	Strength	Img (a)	Img (b)	Img (c)	Img (d)	Proposed	Niu *et al.* (2020)	Pereira and Pun (2000)
JPEG compression	90%	0.96	1	0.96	0.96	**0.97**[7]	0.93	0.80
	80%	0.83	0.96	0.91	0.96	**0.92**	0.90	0.51
	70%	0.87	0.96	0.87	0.96	**0.92**	0.89	0.31
	60%	0.87	0.84	0.8	0.91	**0.86**	0.83	0.24
	50%	0.87	0.96	0.75	1	**0.90**	0.80	0.22
Gaussian blur 3×3	0.5	0.96	1	0.96	0.96	**0.97**	0.83	0.89
	0.6	0.96	1	0.96	0.96	**0.97**	0.83	0.87
	0.7	0.96	1	0.96	0.96	**0.97**	0.80	0.85
	0.8	0.96	1	0.91	0.96	**0.96**	0.79	0.83
	0.9	0.96	1	0.87	0.96	**0.95**	0.80	0.82
Gaussian noise 3×3	0.01	0.83	0.79	0.76	0.83	**0.80**	0.85	0.46
	0.02	0.87	0.83	0.8	0.97	**0.87**	0.85	0.31
	0.03	0.87	0.84	0.83	0.83	**0.84**	0.87	0.35
	0.04	0.7	0.91	0.83	0.87	**0.83**	0.86	0.30
	0.05	0.79	0.84	0.83	0.85	**0.83**	0.85	0.32

6. MNC refers to the mean normalized correlation, which is derived from the mean correlation coefficient of the experimental images

7. The bolded data indicate the specific values when the algorithm outperforms the comparison algorithm for the same attack

Table 6. Normalized correlation (NC) under rotation and image conventional processing compound attacks.

		20.00	40.00	60.00	80.00	100.00	120.00	140.00	160.00	180.00
JPEG compression/%	50	0.83	0.78	0.87	0.87	0.87	0.96	0.87	0.78	0.83
	60	0.96	0.78	0.87	0.78	0.87	1.00	0.96	0.78	0.87
	70	0.96	0.78	0.91	0.83	0.87	0.91	0.96	0.83	0.91
	80	0.96	0.87	0.96	0.91	0.91	0.91	0.96	0.87	0.91
	90	0.91	0.87	0.96	0.87	0.96	0.91	0.96	0.91	0.96
Gaussian blur 3×3	0.5	1.00	0.87	0.96	0.87	0.91	0.91	0.96	0.87	0.91
	0.6	1.00	0.83	0.96	0.87	0.91	0.91	0.96	0.87	0.91
	0.7	1.00	0.83	0.96	0.87	0.91	0.91	0.96	0.91	0.91
	0.8	1.00	0.83	0.96	0.87	0.91	0.78	0.96	0.91	0.91
	0.9	1.00	0.83	0.96	0.87	0.87	0.91	0.96	0.91	0.91
Gaussian noise 3×3	0.01	0.78	0.75	0.96	0.75	0.83	0.78	0.83	0.78	0.87
	0.02	0.75	0.71	0.83	0.75	1.00	0.87	0.78	0.78	0.83
	0.03	0.71	0.83	0.96	0.75	0.78	0.78	0.78	0.78	0.87
	0.04	0.87	0.13	0.78	0.71	0.78	0.87	0.83	0.71	0.96
	0.05	0.83	0.71	0.75	0.71	0.78	0.78	0.78	0.78	0.75

Table 7. Normalized correlation (NC) under scaling and image conventional processing compound attacks.

		0.9	0.8	0.7	0.6	1.1	1.2	1.3	1.4	1.5
JPEG compression/%	90	0.96	0.87	0.96	0.91	0.91	0.83	0.91	0.91	0.83
	80	0.87	0.87	0.91	/	0.87	0.91	0.96	0.91	0.91
	70	0.87	0.83	/	/	0.91	0.96	0.96	0.91	0.83
	60	0.87	0.78	/	/	0.91	0.96	0.96	0.91	0.91
	50	0.78	0.13	/	/	0.96	0.91	0.91	0.91	0.91
Gaussian blur 3×3	0.5	0.91	0.96	0.91	0.91	0.91	0.91	0.91	0.91	0.91
	0.6	0.91	0.91	0.91	/	0.91	0.91	0.91	0.91	0.91
	0.7	0.87	0.91	0.91	/	0.91	0.91	0.91	0.91	0.91
	0.8	0.87	0.91	0.91	/	0.91	0.91	0.91	0.91	0.91
	0.9	0.87	0.91	0.87	/	0.91	0.91	0.91	0.91	0.91
Gaussian noise 3×3	0.01	0.83	0.87	0.78	0.78	0.91	0.87	0.83	0.83	/
	0.02	0.13	0.83	/	/	0.78	0.83	0.87	0.87	/
	0.03	0.13	0.83	0.78	/	0.71	0.78	0.91	0.83	/
	0.04	0.78	0.87	/	/	0.13	0.87	/	/	0.87
	0.05	0.83	0.78	0.13	/	0.91	0.91	0.78	/	/

of 0.68 is relatively weak when the radius is 60 px for Gaussian noise attacks with a variance of 0.05. Therefore, the robustness to Gaussian noise attacks is better at radii of 60–130 px.

Figure 11c shows the robustness of the watermark embedded at different radii against JPEG compression attacks with parameters 60, 80, and 90. The NC decreases overall as the compression strength increases and is greater than the threshold 0.75 overall when the radius is between 60 and 100 px and decreases significantly when the radius is greater than 100 px. Thus, the robustness to compression attacks is better between radius 60–100px.

In summary for the analysis of noise, blur, compression, and other attacks, the robustness of conventional image process attacks on images is generally better when the radius is 65–100 px. In order to make the image resistant to a certain range of scaling attacks, the radius changes in the scaling range needs to be controlled within 65–100 px. We set the radius to 80 px, when the scaling degree is 60%–150%, the radius changes in the range of 53–133 px, which can resist the above attacks.

The radius of the watermark embedding in this paper is a very crucial parameter. The choice of the radius will not only affect the robustness to conventional image processing attacks, but also affect the robustness to different degrees of geometric attacks. In this paper, the radius of embedding is set to 80 through the above experiments and analysis of radius selection, which can resist a wide range of geometric attacks with the verification of robustness experiments. As verified by the above experiments, with the radius selection in this paper, it also has strong robustness against image processing attacks. The embedding radius in this paper is relative to the chunk size of 300. Meanwhile, according to the invisibility experiments, it can be shown that the radius selection in this paper can have good invisibility. In summary, the radius selection in this paper can get the balance of security and invisibility. The distance from the embedding radius to the center of the chunk is 8/30 of the chunk size, and the radius needs to be embedded at the same ratio when the chunk size is adjusted.

Image Compression Attacks

It is found that the accuracy of the watermark is higher in some experiments when the compression degree is 50, compared to when the compression degree is 60–70. This subsection focuses on the relationship between the degree of image compression attack and the degree of watermark loss in algorithmic attacks. The compression operation used in the experiments is the Python Imaging Library image processing library, and we found that the degree of compression of the image is not exactly proportional to the degree of loss of the watermark.

The reason is that when the compression ratio is before 6–9, the change of compression on the image is concentrated in the middle frequency of the image. As the compression ratio becomes larger, the loss of the middle frequency region is more serious. However, when the compression ratio is 5, the change of compression on the image is concentrated in the center of the image. At this time, the loss of the image is not on the watermark embedding region; thus, it can get better extraction results. Therefore, the enhancement of the compression ratio can only represent the enhancement of the image loss, not exactly the enhancement of the watermark information attack.

Generality of the Research Subject

This subsection discusses the generality of the research object of this paper. The research object of this paper focuses on remote sensing images, which usually exist in the form of large size during the use of remote sensing impact. At the same time, unlike ordinary images, remote sensing images are richer in feature information. With the rich features, using the feature point-based extraction watermarking method for ordinary images will bring more challenges to the stability of the algorithm. Although the research object of this paper focuses on remote sensing images, the algorithm is also applicable on ordinary images.

Limitations of Affine Transformation Attack

This subsection discusses the limitations of the algorithm in this paper for affine transformation attacks. Since DFT does not have the property of invariant to affine transformation, the algorithm extracts the watermark ring based on its circular features. Unfortunately, the watermark does not have circular features after affine transformation and cannot be extracted according to the extraction algorithm in this paper.

Conclusion

Aiming at the problem of weak robustness for remote sensing image digital blind watermarking against geometric attacks, a blind and robust watermarking algorithm based on location template watermarking for remote sensing image is proposed. The algorithm takes the DFT domain template watermark as the invariant feature, adopts a cyclic template watermark, increases the watermark capacity by the embedding position selection rule, and determines whether the watermark is included. It can accurately extract the geometric attack parameters by noise extraction and template matching for geometric attacks. In the crucial embedding radius selection aspect, we focus on the radius change generated during the scaling of geometric attacks. In order

Table 8. Normalized correlation (NC) under scaling and rotation compound attacks.

	20%	40%	60%	80%	100%	120%	140%	160%	180%
1.1	0.96	0.87	0.96	0.87	0.91	0.91	0.96	0.91	0.91
1.2	1	0.87	0.96	0.87	0.91	0.91	0.96	0.84	0.87
1.3	0.96	0.87	0.96	0.87	0.91	0.91	0.96	0.08	0.91
1.4	1	0.87	0.96	0.87	0.91	0.91	0.96	0.87	0.91
1.5	1	0.87	0.96	0.87	0.91	0.91	0.96	0.08	0.91
0.9	1	0.84	0.96	0.87	0.91	0.91	0.96	0.91	0.91
0.8	0.96	0.87	0.96	0.87	0.91	0.91	0.96	0.91	0.91
0.7	1	0.87	0.96	0.87	0.91	0.91	0.96	0.87	0.91
0.6	1	0.87	0.96	0.91	0.91	0.96	1	0.91	0.91

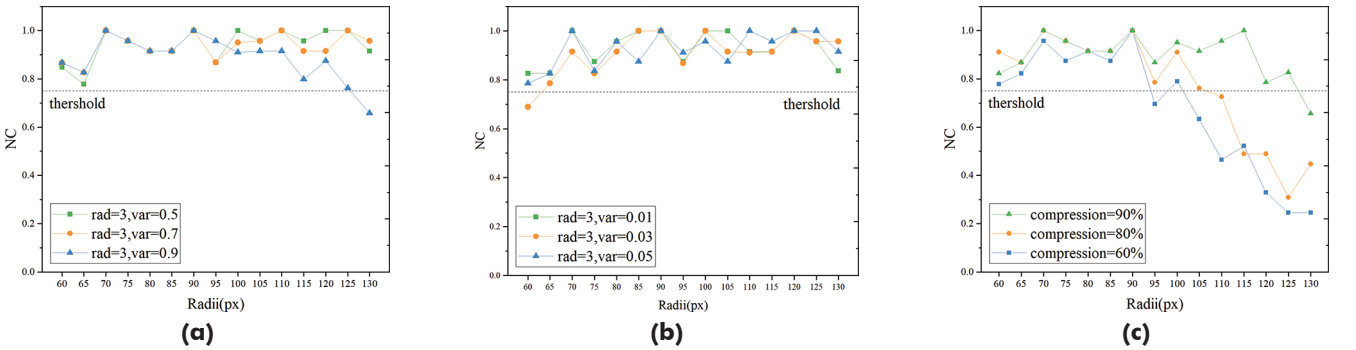

Figure 11. Robustness of embedded watermarks under compression, filtering, and noise attacks at different radii. (a) The robustness of the watermark embedded at different radii to Gaussian blur attacks. (b) The robustness of the watermark embedded at different radii to Gaussian noise attacks. (c) The robustness of the watermark embedded at different radii against jpeg compression attacks.

to extract accurately within the change range and to make the image resistant to image conventional attacks, experiments were designed to select the appropriate radius after image attacks under different radii.

Geometric attack robustness experiments, image conventional attack experiments, compound attack experiments, and comparison experiments are conducted in this paper. The experimental results show that the algorithm can effectively improve the robustness against geometric attacks. The algorithm has better robustness against common image processing attacks and has stronger robustness against geometric attacks than the comparison paper. However, DFT does not have the property of invariance to affine transformation. Therefore, the watermark does not have circular features after affine transformation and cannot be extracted according to the extraction algorithm in this paper. Thus, the algorithm has poor robustness to resist affine attack. It is worth further research to improve the robustness of remote sensing image digital watermark to affine attack.

Acknowledgments

The data sets for this study can be found in the 91weitu (https://www.91wemap.com/). Author contributions are as follows: conceptualization, Xinyan Pang and Na Ren; methodology, Changqing Zhu; validation, Shuitao Guo and Ying Xiong; formal analysis, Shuitao Guo; writing, Xinyan Pang; review and editing, Na Ren; supervision, Changqing Zhu. All authors have read and agreed to the published version of the manuscript. This work was funded in part by the National Natural Science Foundation of China under Grant 41971338, 42071362; in part by the Natural Science Foundation of Jiangsu Province under Grant BK20191373; in part by the Postgraduate Research & Practice Innovation Program of Jiangsu Province KYCX21_1357. The authors declare that the research was conducted in the absence of any commercial or financial relationships that could be construed as a potential conflict of interest. All claims expressed in this article are solely those of the authors and do not necessarily represent those of their affiliated organizations, or those of the publisher, the editors, and the reviewers. Any product that may be evaluated in this article, or claim that may be made by its manufacturer, is not guaranteed, or endorsed by the publisher.

References

Amhar, F., E. P. Giri, F.E.S. Silalahi, S. N. Neyman, Anggrahito, D. Ramdani, D. Jaya, D. Sutrisno, S. A. Kolopaking, T.R.N. Rachma and Murdaningsih. 2022. Ownership protection on digital elevation model (DEM) using transform-based watermarking. *ISPRS International Journal of Geo-Information* 11. https://doi.org/10.3390/ijgi11030200.

Chen, W., N. Ren, C. Zhu, Q. Zhou, T. Seppänen and A. Keskinarkaus. 2020. Screen-cam robust image watermarking with feature-based synchronization. *Applied Sciences* 10:7494. https://doi.org/10.3390/app10217494.

Dajun, H. and S. Qibin. 2005. A practical print-scan resilient watermarking scheme. Pages I–257 in *Proceedings of the IEEE International Conference on Image Processing 2005*, held in Genova, Italy.

Dappuri, B., M. P. Rao and M. B. Sikha. 2020. Non-blind RGB watermarking approach using SVD in translation invariant wavelet space with enhanced grey-wolf optimizer. *Multimedia Tools and Applications* 79:31103–31124. https://doi.org/10.1007/s11042-020-09433-0.

Fang, H., D. Chen, Q. Huang, J. Zhang, Z. Ma, W. Zhang and N. Yu. 2021. Deep template-based watermarking. *IEEE Transactions on Circuits and Systems for Video Technology* 31:1436–1451. https://doi.org/10.1109/tcsvt.2020.3009349.

Fu, H., J. Wen, P. Ge and S. Bian. 2016. Research on blind-watermarking algorithm in transform domain for raster geo-data based on synchronous function. *Geography and Geo-Information Science* 32:65–70. https://doi.org/10.3969/j.issn.1672-0504.2016.05.010.

Hsu, P.-H. and C.-C. Chen. 2016. A robust digital watermarking algorithm for copyright protection of aerial photogrammetric images. *The Photogrammetric Record* 31:51–70. https://doi.org/10.1111/phor.12134.

Keskinarkaus, A., A. Pramila and T. Seppänen. 2012. Image watermarking with feature point based synchronization robust to print–scan attack. *Journal of Visual Communication and Image Representation* 23:507–515. https://doi.org/10.1016/j.jvcir.2012.01.010.

Lee, J.-E., Y.-H. Seo and D.-W. Kim. 2020. Convolutional neural network-based digital image watermarking adaptive to the resolution of image and watermark. *Applied Sciences-Basel* 10. https://doi.org/10.3390/app10196854.

Li, J.-Y. and C.-Z. Zhang. 2020. Blind watermarking scheme based on schur decomposition and non-subsampled contourlet transform. *Multimedia Tools and Applications* 79:30007–30021. https://doi.org/10.1007/s11042-020-09389-1.

Mohammed, A. A., D. A. Salih, A. M. Saeed and M. Q. Kheder. 2020. An imperceptible semi-blind image watermarking scheme in DWT-SVD domain using a zigzag embedding technique. *Multimedia Tools and Applications* 79:32095–32118. https://doi.org/10.1007/s11042-020-09694-9.

Niu, P., L. Wang, X. Shen, S. Zhang and X. Wang. 2020. A novel robust image watermarking in quaternion wavelet domain based on superpixel segmentation. *Multidimensional Systems and Signal Processing* 31:1509–1530. https://doi.org/10.1007/s11045-020-00718-z.

Pereira, S. and T. Pun. 2000. Robust template matching for affine resistant image watermarks. *IEEE Transactions on Image Processing* 9:1123–1129. https://doi.org/10.1109/83.846253.

Pramila, A., A. Keskinarkaus and T. Seppänen. 2008. Multiple domain watermarking for print-scan and JPEG resilient data hiding. In *Digital Watermarking*. Berlin Heidelberg: Springer, pp. 279–293.

Singh, P., K. J. Devi, H. K. Thakkar and J. Santamaría. 2021. Blind and secured adaptive digital image watermarking approach for high imperceptibility and robustness. *Entropy* 23. https://doi.org/10.3390/e23121650.

Solanki, K., U. Madhow, B. S. Manjunath and S. Chandrasekaran. 2004. Estimating and undoing rotation for print-scan resilient data hiding. Pages 39–42 in *Proceedings of the 2004 International Conference on Image Processing*, held in Singapore.

Su, Q., H. Wang, D. Liu, Z. Yuan and X. Zhang. 2020. A combined domain watermarking algorithm of color image. *Multimedia Tools and Applications* 79:30023–30043. https://doi.org/10.1007/s11042-020-09436-x.

Sun, X.-C., Z.-M. Lu, Z. Wang and Y.-L. Liu. 2021. A geometrically robust multi-bit video watermarking algorithm based on 2-D DFT. *Multimedia Tools and Applications*. https://doi.org/10.1007/s11042-020-10392-9.

Tarhouni, N., M. Charfeddine and C. Ben Amar. 2020. Novel and robust image watermarking for copyright protection and integrity control. *Circuits Systems and Signal Processing* 39:5059–5103. https://doi.org/10.1007/s00034-020-01401-1.

Wang, X., N. Ren, C. Zhu and Y. Yu. 2017. A digital watermarking algorithm based on QR code and quantization DCT for remote sensing image. *Geography and Geo-Information Science* 33:19–24. https://doi.org/10.3969/j.issn.1672-0504.2017-06.004.

Wang, X.-Y., P.-P. Niu, L. Meng and H.-Y. Yang. 2011. A robust content based image watermarking using local invariant histogram. *Multimedia Tools and Applications* 54:341–363. https://doi.org/10.1007/s11042-010-0534-y.

Yu, C., X. Li, X. Chen and J. Li. 2019. An adaptive and secure holographic image watermarking scheme. *Entropy* 21. https://doi.org/10.3390/e21050460.

Zhou, Q., N. Ren, C. Zhu and A.-X. Zhu. 2020. Blind digital watermarking algorithm against projection transformation for vector geographic data. *ISPRS International Journal of Geo-Information* 9. https://doi.org/10.3390/ijgi9110692.

Zhou, W., C. Zhu and W. Wu. 2015. Review of the security features of geographic information. *Bulletin of Surveying and Mapping* 122–125. https://doi.org/10.13474/j.cnki.11-2246.2015.0329.

Zhu, C. 2017. Research progresses in digital watermarking and encryption control for geographical data. *Acta Geodaetica et Cartographica Sinica* 46:1609–1619. https://doi.org/10.11947/j.AGCS.2017.20170301.

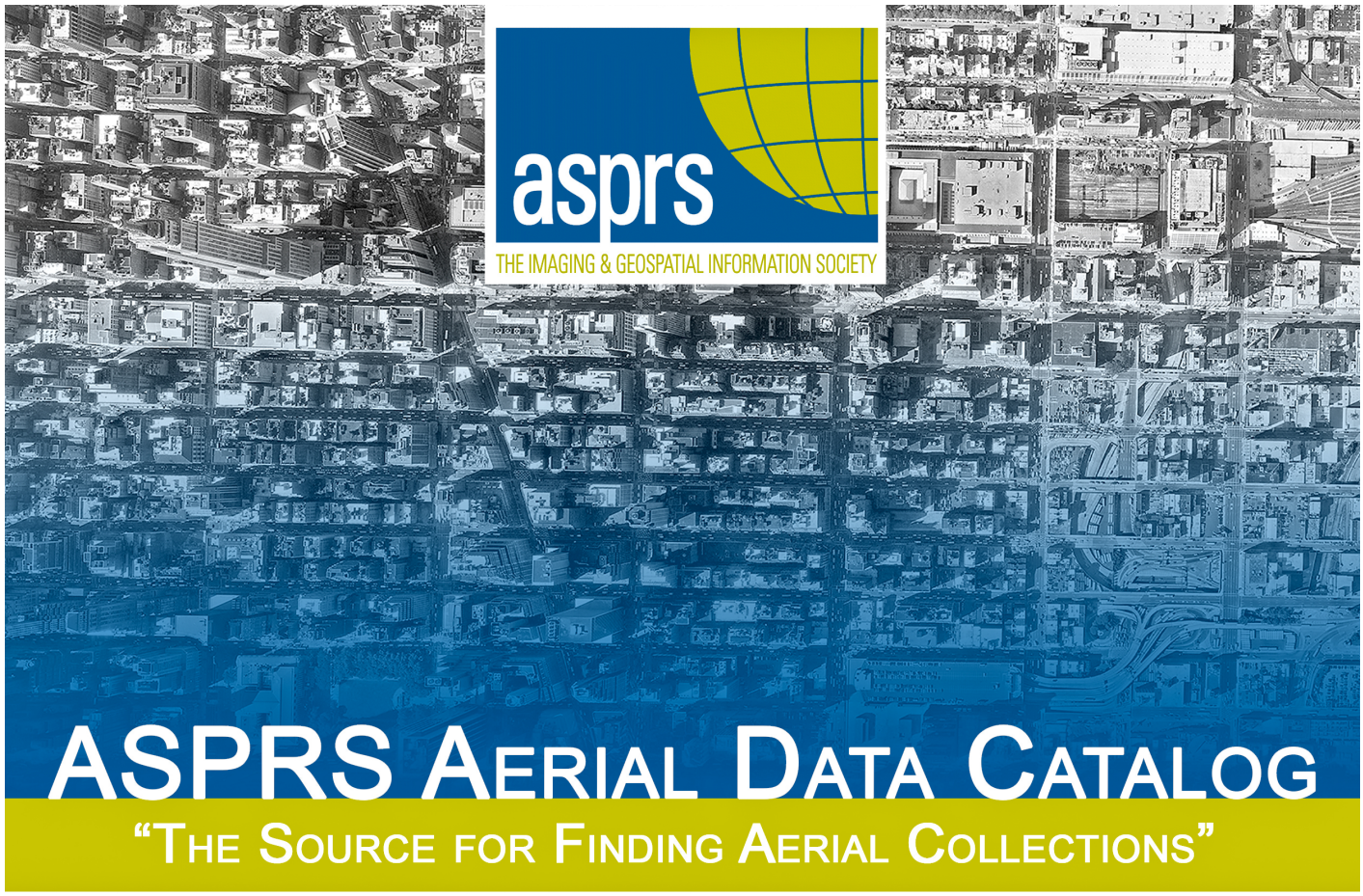

asprs
THE IMAGING & GEOSPATIAL INFORMATION SOCIETY

ASPRS Aerial Data Catalog

"The Source for Finding Aerial Collections"

http://dpac.asprs.org

The ASPRS Aerial Data Catalog is a tool allowing owners of aerial photography to list details and contact information about individual collections.

By providing this free and open metadata catalog with no commercial intrests, the Data Preservation and Archiving Committee (DPAC) aims to provide a definitive metadata resource for all users in the geospatial community to locate previously unkown imagery.

DPAC hopes this Catalog will contribute to the protection and preservation of aerial photography around the world!

ASPRS Members: We Need Your Help!
There are three ways to get involved

1 USE — Use the catalog to browse over 5,000 entries from all 50 states and many countries. Millions of frames from as early as 1924!

2 SUPPLY — Caretakers of collections, with or without metadata, should contact DPAC to add their datasets to the catolog free of charge!

3 TELL — Spread the word about the catalog! New users and data collections are key to making this a useful tool for the community!

For More Details or To Get Involved Contact:

David Ruiz • druiz@quantumspatial.com • 510-834-2001 OR David Day • dday@kasurveys.com • 215-677-3119

LEARN
DO
GIVE
BELONG

ASPRS

AMERICAN SOCIETY FOR PHOTOGRAMMETRY & REMOTE SENSING

ASPRS Offers

- » Cutting-edge conference programs
- » Professional development workshops
- » Accredited professional certifications
- » Scholarships and awards
- » Career advancing mentoring programs
- » *PE&RS*, the scientific journal of ASPRS

asprs.org